University of Milan - Bicocca

Ph.D. School in Nanostructures and Nanotechnology

Ph.D. Thesis

GaAs/AlGaAs Quantum Dot Intermediate Band Solar Cells

Andrea Scaccabarozzi

Supervisor:
Dr. Maurizio Acciarri

Supervisor:
Prof. Stefano Sanguinetti

Si parva licet componere magnis,
accipe opus meum et lege,
et semper tibi sit memoria
saepe magna celari parvis rebus.

ABSTRACT

This thesis presents my Ph.D. work about quantum dot GaAs / $Al_{0.3}Ga_{0.7}As$ solar cells grown by droplet epitaxy, exploring the potential of this materials system for the realization of intermediate band photovoltaic devices.
In the first chapter a general introduction to the field of solar energy is given, outlining the reasons why this research has been performed. The physics of the photovoltaic cell is briefly explained in its most important points, to give the reader clear understanding of what is presented in the following chapters.
Intermediate band devices are presented in the second chapter. The theoretical foundations presented do not aim at constituting an exhaustive explanation of the theory underlying intermediate band solar cells, but the scope is again to give clear understanding of the characterization of the quantum dot devices reported in the following chapters. A survey of the state of the art in the field is given, pointing out the differences with our technology.
The initial part of my Ph.D. work was spent in developing the technology to design and grow (Al)GaAs photovoltaic devices, as well as the characterization techniques required to understand the behavior of such devices. In chapter 3 the method developed to design the solar cell structure is illustrated, and in chapter 5 the experimental setup used for characterization is presented, along with the

measurements on the single junction devices realized during this work. Chapter 4 is dedicated to the description of the growth and fabrication methods used to grow the samples reported here. The development of the fabrication technology proceeded in close contact with the characterizations of the devices, in order to optimize the process.
Finally in chapter 6 the results on quantum dot photovoltaic cells are reported: the key working principles of intermediate band devices have been demonstrated with our materials system, and this, to the knowledge of the author, is the first time that strain free quantum dot solar cells are reported of intermediate band behavior. The role of defects in the $Al_{0.3}Ga_{0.7}As$ matrix is explained in connection with both the optical and electrical characterizations presented.

An important part of my Ph.D. work has been devoted to the characterization of GaAs structures grown on novel Si substrates, the final goal being the integration of photovoltaic (but not limited to it) III-V technology on Si. This part of my work is not reported here for the sake of unity of the quantum dot solar cell work, though it provided important scientific output that has been and is being published elsewhere.

CONTENTS

CHAPTER 1

INTRODUCTION

In this first chapter we will outline the motivations that lie at the basis of this research. We will firstly generally describe the so-called energy problem about the continuously growing demand for energy and the finite nature of our currently used energy sources, and after that we'll describe the working principles of photovoltaic devices, which are likely to be one of the most relevant perspective solution to the energy problem. The general description of PV devices will be concluded presenting the key mechanisms that lead to efficiency loss in solar cells.

1.1 Hungry of energy

In the last two decades the world has experienced unprecedented economical and social development, and if from one side we still see western countries in the dominant positions, on the other side developing countries already represent the biggest driving force for economical expansion. Such a big and rapid development poses a serious question whether this trend is sustainable or not in a world with finite resources. A very important yet not exhaustive parameter to quantify worldwide development is the total demand

for electrical energy, for there's a strict connection with industrial production and household power consumption. This parameter is not exhaustive because a more comprehensive view should include also the energy consumed for transportation and refinement of materials. Nevertheless it points out a trend of impressive growth. As we can see from figure 1.1 the primary electrical energy demand has doubled in the last 35 years. More than 80% of our power needs are satisfied by burning fossil fuels like coal, oil or gas, while 10% is obtained by burning waste or organic fuels. This sums up to more than 90% of our current electric power coming from carbon/hydrogen containing materials burnt in thermoelectric plants. The energy needed for transportation is also provided by derivatives of oil that are burnt in thermal engines. This should be enough to

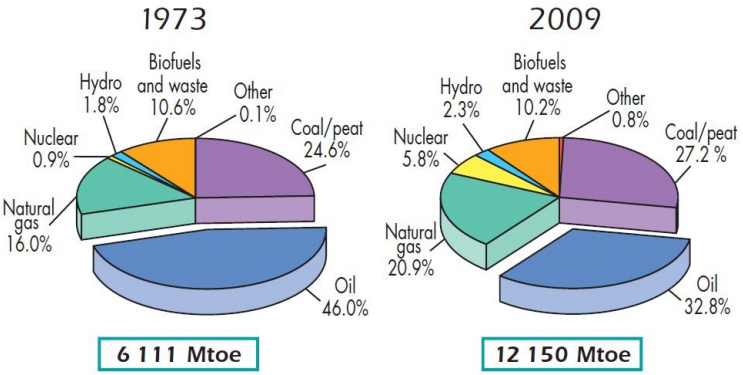

Figure 1.1: Evolution of the world electrical energy demand, with different generation sources outlined as a percentage of the total amount, in Millions of Tons of Oil Equivalent. Data from IEA, [1].

realize that modern society is completely dependent on supplies of fossil fuels, and that there is absolutely no way to avoid consuming them at least in the short or medium term. But if one tries to look further into the future, it's also evident how the fossil fuels cannot be used indefinitely in time, because of their extremely long generation times, of the order of geological eras. So, as it is usually done, we can assume that the global reserves of fossil fuels constitute a finite amount undergoing continuous depletion due to

our exploitation. At some point in the future all of these reserves will be exhausted and in the present scenario, there will be left only about 10% of the electric energy available today, if not even less. This topic is rather controversial among economists, because some suggest that the current reserve estimates only include the economically convenient deposits: due to the decrease of reserves we'll see a big rise in prices and this will make many more deposits, like tar-sands, convenient for exploitation. Anyway it's clear that this will only shift later in time the total depletion moment. This is actually what has been observed in the last years in western countries, namely the Hubbert's oil peak. Some economists on the other hand [2] believe that assumptions like Hubbert's are too simplistic for a reliable model, since the real market is strongly influenced by political decisions and financial speculation. Moreover, the global economy is rapidly changing with a lot of new actors who can influence the oil market, which in close feedback influences the economy worldwide.

Another problem introduced by the use of fossil fuels is the release into the atmosphere of a large amount of carbon dioxide and other pollutants. CO_2 is well known to be a greenhouse gas, that together with water vapor and methane contributes to keep the average temperature of the Earth around 20°C. Industrial activities and fossil fuel combustion for transportation or electricity generation have released a large amount of CO_2 contributing to the increase of the natural greenhouse effect. No absolutely conclusive demonstration has been provided so far that any climate changes can be directly related to human activity. A lot of debate is still alive in the scientific community about the true responsibility of human activities for global warming. There might be other factors influencing global climate, like solar activity changes or increased volcanic activity, for which in history a correlation with chiller periods has been found. Nevertheless greenhouse gas emissions can indeed increase the Earth temperature and lead to climate instability with dramatic consequences for the future of mankind, especially in less developed rural areas, where people are much more sensitive to droughts or floods. In 2009 the total carbon dioxide emissions scored at 29 thousand of metric tons [1]. May they be responsible for global warming or not, in figure 1.2 we can indeed observe how large the increase trend in these yearly emissions is.

In case they have some effect on global warming, it's extremely important to find a way to avoid them. In case they don't, still it's much better to avoid them, because pollutants of proven toxicity and carcinogenicity are released alongside. A reduced, if not ab-

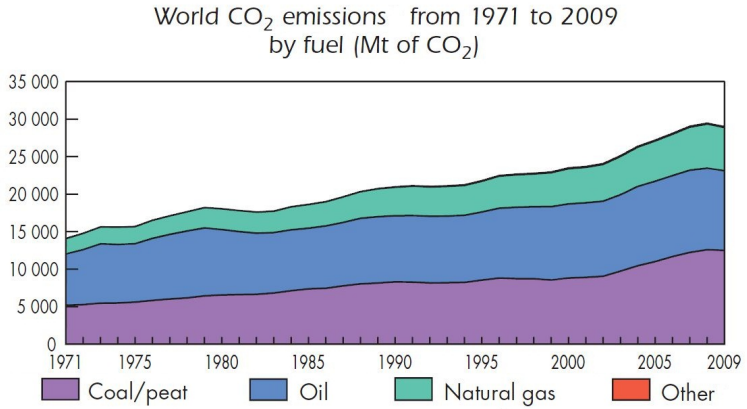

Figure 1.2: Historical data of CO_2 emissions per year, divided by source, in metric tons. Data from IEA [1].

sent, dependence on fossil fuels would certainly prevent greenhouse-related warming and would contribute significantly to a reduction of atmospheric pollution. Renewable energy sources can be clear answers to these problems, since they have very low environmental impact and they can provide safety from energy supply risks coming from reserve depletion or political instability. That's why there is a lot of effort to increase the renewable component in the energy mix in developed countries.

The term *renewable energy* is applied to all the energy sources which will not exhaust or change significantly in million of years to come. A clear example is solar energy: sunlight warms up our planet but at the end of each day its warming power is not consumed, but will *renew* for another day[1]. Besides solar energy, there are wind energy, tidal energy, geothermal energy and hydroelectric

[1]The limit to this is set by astrophysics to about 5 billion of years, enough to be considered infinite for human needs.

energy.

Hydroelectric power generation is already a largely used buffering mechanism to deal with peaks of demand during the day in countries where water basins or high flow rivers are available. This is because there is no need to start a thermal engine, but it's sufficient to let water fall and drive turbines. From this point of view, hydro energy looks more like a kind of gravitational storage mechanism than an alternative fuel. In developed countries however, most of the possible sites to localize such plants are already exploited nearly at full potential, so there is no more room for expansion, unless we want to face the risk of hydrogeological instability or move hundreds of thousands of people away from their houses. Indeed no pollution or carbon emissions are related to hydro power, apart from those needed to build the plants.

Tidal energy could be a different approach to hydro power generation, dealing with the installation of low speed high mass turbines in locations where the difference in daily tides is significant. As for traditional hydro power the same considerations apply to locations of plants and cleanliness of the energy produced.

Geothermal energy could be a very interesting resource in countries with significant volcanic or sub-volcanic activity, since this is usually related to the presence of high temperature regions underground. Through the installation of wells and suitable heat pipes, it's possible to power thermal engines overground that produce electricity. The exploitation of the internal heat of the Earth seems to have no time constraints, since the heat capacity of the planet is large enough. Otherwise the need for a suitable low-depth geological conformation is likely to prevent geothermal energy to be the answer to the world energy needs.

Today wind energy is one of the most important candidates to become a significant contributor to the world power production. Turbines located in windy areas can exploit the atmospheric kinetic energy just like tidal energy, with the advantage of being of much easier implementation. In spite of issues like noise, landscape damage and wind fickleness, among green sources wind energy reports the top amount of installed power capacity, 238GW accounting for 345TWh of produced energy as of 2011 [3]. This is less than 2% of

the globally consumed energy in 2010, more than 18000TWh! [1]. As the energy demand is forecast to grow to 40000TWh in 2050 [4], wind power is not likely to be able to reach that enormous amount of energy, even if a large increase of wind farms and offshore plants occurs. Nevertheless it will be a fundamental part of the future energy mix, providing clean and reliable electricity.

Biomass and waste burning are sometimes included among the renewable energy sources, as they are inherent to the life cycle of our planet and human activity itself. As of 2010 [1] they contribute to about 10% of global power generation, and will probably keep this share in future because it's the most cost effective way of getting rid of the waste produced by mankind. Anyway this source of energy cannot be considered clean, as it still produces carbon dioxide in burning processes.

Nuclear energy is also sometimes considered a clean energy source, but it's opinion of the author that this is absolutely not the case. First of all it is not renewable, as long as it is entirely fission-based and fusion plants are not developed, since uranium is present in limited quantity on the Earth. Then, even though it's true that the carbon footprint is limited to the small amount emitted in the uranium mining and refining processes, the complete environmental footprint must include the radioactive waste problem, which so far has not been solved at all. Also nuclear plants bring with them the risk of accidents with radionuclide release, not only in old plants, as the Fukushima Dai-ichi disaster has recently shown.

Solar energy is probably the most promising source of clean and abundant energy that we have at the moment, with an estimated generation capacity of *ten thousand* times the current global demand [4]. This estimate is quite easy if one considers the average amount of solar irradiation at sea level over an area equal to the planet surface minus the oceans' surface. As shown in figure 1.3 solar energy greatly surmounts all the other energy sources. That's why there is large effort in the scientific community in finding new and more efficient ways of exploiting such a huge potential. There are 3 main different ways to exploit solar energy:

- Passive heat

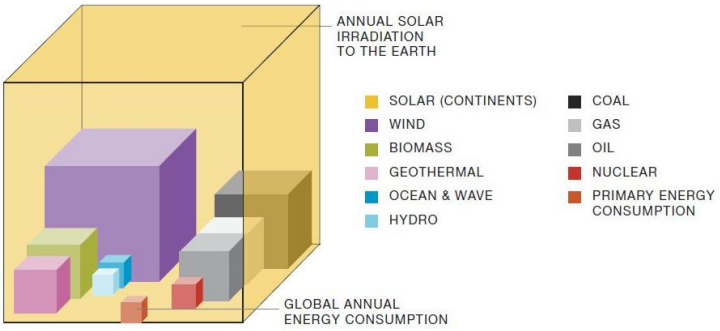

Figure 1.3: Comparison of the potential of the currently known energy sources. Estimates are made on the basis of climate models and statistical data. From [4].

This is nothing but the way the sun naturally warms up our planet. One can easily find the energy balance between the Sun and Earth considering them as blackbody emitters at two different temperatures, coupled by the Stefan-Boltzmann law of radiative heat transfer. With the inclusion of geometrical factors accounting for the relative sizes and positions in the solar system and albedo and greenhouse coefficients, a reasonable equilibrium temperature of 18°C is found for Earth [5]. This results as an average of darker and lighter places, basically poles and equator. Since environmental temperature changes are usually not higher than 20 or 30 degrees from the average it is inconvenient to use work producing machines, because the (Carnot) efficiency will be extremely low. Despite that, it's still possible to use passive heat to save electrical power, for example using it to warm up water in tubes for household consuming, or to use solar-fueled evaporation air conditioning systems.

- Solar thermal
  This is generally referred to power plants using large area mirrors to focus sunlight onto a water containing tank. With high concentration in sunny areas it is easily possible to heat

water (or other substances) up to several hundreds of degrees, producing high pressure steam that can be used to power up turbines and generate electricity. Thanks to the high thermal capacity of the water, such systems can be engineered in order to have a large generation capacity even at night. The total conversion of sunlight into heat is what usually happens, so the efficiency of this kind of systems is limited only by the optical concentration, that is related to the maximum temperature that can be reached by the tank, and by the conversion into electricity, that can be higher than 60% in optimized plants.

- Photovoltaic energy
  Photovoltaics deals the direct conversion of sunlight into electric current. Solar cells exploit this effect, thanks to their capability of generating and collecting charge carriers when illuminated with sunlight. This charge flow, as long as the illumination is steady, constitutes a direct current flow through the photovoltaic (PV) cell. The difference of electric potential is determined by the material and device characteristics, and, like the current, it is strongly related to its absorption spectrum. Therefore PV cells act as DC generators without any need for additional thermal cycles to get electricity. Since the energy density of sunlight (measured per unit area) is rather low than fossil fuel's (measured per unit mass), it is necessary to cover large areas with PV devices to get current levels suitable for large scale applications. Moreover, since the common electrical grid is based on AC transmission, an inverter is needed to connect DC PV plants to the grid.

Photovoltaics has seen a big development in the last decades, thanks to its convenience, reliability and versatility to adapt to different needs of electric power generation. This Ph.D. thesis is dedicated to the study of novel photovoltaic devices, as will be more clearly specified later. For this reason in the following paragraph the advantages of photovoltaic solar generation will be briefly reviewed.

1.2 Photovoltaic solar energy production

Photovoltaic solar energy generation has several advantages over the other renewable energy sources. As said before, the technology is reliable and secure from sanitary and military points of view, and it has a very low carbon footprint compared to fossil fuels. The data reported in figure 1.2 represent the estimate of the total amount of carbon dioxide emissions from electricity generation and from transportation. It is indeed true that renewable sources are negligible also because today they represent a negligible part of the energy mix. But looking at intensive data in [4] the emissions can be compared. Coal scores a maximum of 900g/KWh of CO_2, Oil 850g/KWh, while natural gas 400g/KWh; PV emissions instead come only from the cell and modules manufacturing chain, and EPIA estimates the carbon footprint of PV to be only 40g of CO_2 per KWh. Moreover, during the average 25 years of life a PV plant can produce several times the energy consumed for its manufacturing. The energy pay-back time is now estimated to lie between 1 and 3 years in Europe [4], depending on the latitude.
As of 2011, the global generation capacity of PV systems is 70GW [6], with Europe leading the market with a share of nearly 75% as shown in figure 1.4. The global market is predicted to largely

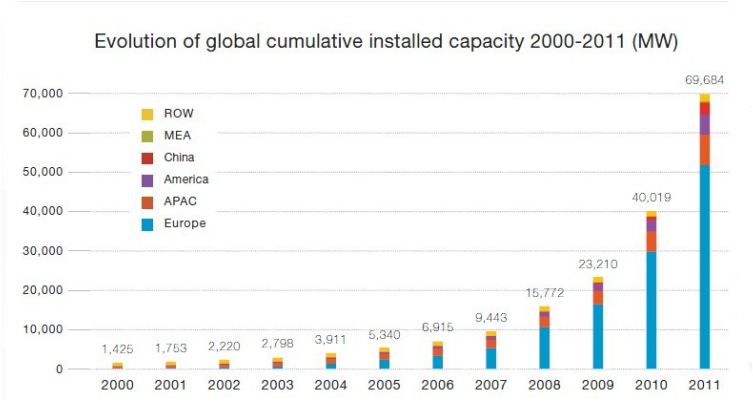

Figure 1.4: Evolution of the global installed PV generation capacity in the last 11 years. From [6].

grow in the next years: the global demand will grow from today's 20 thousand TWh to twice as double in 2050 and PV is forecast to reach 2TWh in 2030 and a range among 500 and 6700 TWh in 2050 [1] [4]. These predictions are estimates made on the basis of current economical and demographic growth rates, according to different political and economical scenarios, and moderate technology progress in PV cells. In the best view, PV energy will represent as much as 20% of the energy mix by 2050. Even in the best case, it's unlikely that photovoltaics can be the ultimate answer to the energy problem in future, unless significant breakthroughs in cell technology are achieved. A dramatic increase in the efficiency of conversion of solar energy would represent a major shift to higher shares in the energy mix, with clear environmental benefits. This is the reason why a lot of research groups throughout the world are investigating how to overcome current physical and technological limits of PV devices.

1.2.1 Some economics

The world of photovoltaics represents not only a good hope for the future, but it's already a cost-effective reality, at least in developed markets like the European Union. In fact in 2011 PV power reached 21GW of new installations [4], to be compared to wind's 9.6GW and 9.7GW of natural gas, while the dependence on non-renewables has somehow reduced, since decommissioned oil-fueled plants amount to -1.1GW and nuclear to -6.2GW[2]. These results come mainly from political decisions: in fact other developed countries like the USA or Japan have a completely different energy mix, while the EU relies much more on Russian gas supplies. The political scenario in each country determines the cost of energy, which is averaged to 0.15€/KWh in EU27 for example. This number is critical to understand whether PV generation is really competitive in the free market. In the last decade we could experience [4] a price decrease of about 22% every time the worldwide production capacity of PV modules doubled. This is quite an optimistic perspective, since the price of electricity is increasing at a 5% yearly rate, and will soon lead PV to be fully competitive. As an example

[2]This comes after Germany's decision to shut down its nuclear power plants.

in Italy, where the cost of energy is higher than the average and where solar irradiation is high too, it is estimated that PV will be fully competitive with traditional energy sources already from 2013. This is only to give an idea about how close can be the objective of having a real fossil fuel free world.
Actually it is still true that PV technology benefits of advantageous feed-in tariffs (FiTs), to incentivate its diffusion. But this is true also for other energy sources, and has much more to do with politics than the market. As an example, Euratom is funded 0.5 billion € per year only for research on nuclear energy and technology, while all the renewable energy (and PV is only a part of them) FiTs amount to 0.33 billion € per year. IEA estimates that financial aid to the fossil fuel industry amounts worldwide to 312 billion dollars [6].
In spite of any kind of financial support, all the scenarios analyzed by economists agree in predicting a large growth for photovoltaics, also considering that up to now the countries with the top irradiation level (the so called *sunbelt*) or countries with very large potential market like China host by far the minority of installed plants. As has been shown in the European market, the increase in PV modules production capacity will lead to further reduction in costs for new plants, making solar energy more and more convenient. The potential of PV in desert areas or in rural underdeveloped areas is also extremely big and could lead to the energy independence of small communities that today can't benefit of electrical power.

1.3 Basic solar cell physics

Since this work is about nanostructured semiconductor solar cells, we won't take into account any devices other than semiconductor homo- or hetero-junction solar cells in the following.
A solar cell is a semiconductor-based opto-electronic device that converts sunlight into direct current. As it is well known [7], semiconductor materials can absorb photons whose energy is above a certain threshold, the energy gap. The absorption process leads to the generation of a pair of charge carriers[3], namely an electron and

[3]Let us only think of optical (but not Raman) processes, so photon energies are of the order of 1 eV.

a hole, which are free to move in the semiconductor crystal. If some electric field is applied, a current of these charge carriers will flow through the crystal and can be collected by electric contacts at the crystal edges. This photoinduced current is exploited for example in PbS detectors, which need to be electrically biased in order to detect light. In fact if no electric field is present, after some time the free holes and electrons annihilate in a recombination process. The solar cell is somewhat more complex, because in the simplest case it consists of a p-n junction of semiconductor material, that is of course a semiconductor p-n diode. Thanks to the doping gradient in the crystal, a depletion region[4] is formed at the junction and a built-in potential difference is present between the p and the n side. This built-in electric field is what gives the photovoltaic effect:

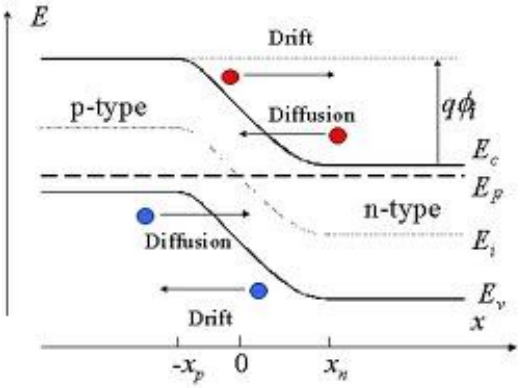

Figure 1.5: The picture shows the band diagram of a p-n junction in direct space. Band bending and the built-in potential are shown.

photogenerated carriers can diffuse to the junction where they are separated and eventually collected by the external contacts, with no need for externally applied fields. So the solar cell acts as a dc current generator, with a voltage dependent on the built-in potential and illumination level, while current depends only on the

[4]It is also called space charge region.

illumination level[5].

1.3.1 The solar spectrum

The emission spectrum of the Sun can be well approximated by that of a blackbody whose temperature is 5750K, as can be seen in figure 1.6. The extra-atmospheric spectrum, called AM0, has

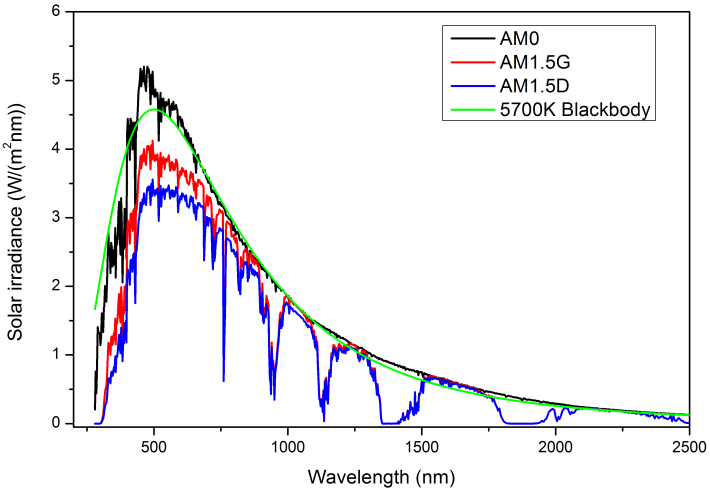

Figure 1.6: The different standard solar spectra compared with a blackbody spectrum. AM is the air mass coefficient. Data are taken from [8]

been measured by satellites and it is consistent with a picture of our Sun being a blackbody at a temperature of 5700K, with the superposition of sharp atomic emission and absorption lines, that make its shape jagged, originating from the atomic plasma in the photosphere. Apart from variations in the solar activity, this spectrum can be exactly measured and it's constant over time. This

[5]At least in a simplified model with no parasitic resistance and low injection levels.

is not the case for the solar spectrum on the ground, after sunlight has passed through the atmosphere. In fact the atmosphere is not homogeneous, with varying concentrations of water vapor, clouds, dust and particulate that can change within few minutes and depend strongly on geographical location and local climate. Nevertheless, in order to understand how terrestrial spectra are modeled, let us consider for a moment a homogeneous atmospheric layer covering the Earth: The atmospheric light absorption can be modeled by a simple Lambert-Beer exponential law that takes into account the passage of light across a certain thickness of a gas layer. One has also to add the Rayleigh scattering effect [9], that gives the reddish appearance to the sky at twilight and blue during the day. To give a complete picture the model should include other effect like scattering by bigger particles, like water droplets or dust. All of these absorption and scattering processes vary during the day as the angle of incidence of sunlight changes[6], and as the concentration of dust or particulate changes. Moreover the weather conditions can change the local spectrum significantly in any moment. Anyway, the most important contribution to spectral variations, apart from locally varying climatic conditions, comes from the angle of incidence of sunlight, and it can be specified by one simple parameter: the air mass. It is defined by

$$A.M. = \frac{1}{\cos\theta} \tag{1.1}$$

where θ is the angle of incidence of sunlight. Since it weighs the optical path length in the atmosphere, the name AM0 to extraterrestrial spectrum is self explained.
In order to establish a reference standard for testing and calibration, it has been decided to use the AM1.5 inclination. The reason for that is to be found from the average latitude where scientific work on photovoltaics started, in the temperate region. It is generally agreed that this is a good way to assess the performance of PV cells and modules that will be installed at those latitudes. The standard spectra used in PV community are called AM1.5G and AM1.5D [8]. They are not truly measured spectra, like AM0, but they are averages of measurements and atmospheric modeling

[6] And also during the year, as seasons pass by.

calculations for our latitudes. The global (G) spectrum includes the indirect sunlight coming from scattering and ground reflection, while the direct (D) spectrum only includes direct radiation and it is used as a reference for optical concentrator devices.

By knowing the semiconductor absorption spectrum and the solar inpinging spectrum it is straightforward to calculate the generation term in the continuity equation of a solar cell as a function of the penetration depth x [11].

$$G(x) = \int AM(\lambda) \cdot (1 - R(\lambda)) \cdot \alpha(\lambda) e^{-\alpha(\lambda)x} \tag{1.2}$$

The term $R(\lambda)$ and $\alpha(\lambda)$ are the reflection and the absorption spectra of the solar cell respectively. Since the real part of the refractive index for semiconductors is typically high (for example in Si is averagely 4 in the visible range), the reflectivity at normal incidence is around 35%, as easily calculated by Fresnel equations [9].
Reflection can be minimized in a certain wavelength band using anti-reflective coatings (ARCs). In fact if a slab of dielectric material of a certain thickness is put over the semiconductor surface, destructive interference conditions can be achieved. The optimum thickness corresponds to the optical path length that gives 180° phase shift in a double pass [10]. Complex antireflective multilayers can be designed and fabricated using different dielectric materials, like TiO_2, SiO_2, Si_xN_y, MgF_2 or ZnS, and in this way very low reflectivities can be obtained. Since solar cells should be cheap devices, they usually have only a single layer silicon oxide or nitride ARC, but more complex and efficient devices often rely on multi layered ARCs that offer broader bands and higher transmittance.

1.3.2 Solar cell device model

In this paragraph the most important equations that govern the physics of semiconductor junction solar cells are shortly reviewed. For simplicity we'll refer to homojunction p-n diodes (figure 1.5).
The intrinsic carrier concentration n_i is related to the energy gap E_g by

$$n_i = \sqrt{N_c N_v} \cdot e^{\frac{-E_g}{2kT}} \tag{1.3}$$

where N_c and N_v are the effective density of states of the conduction and valence band respectively and kT is the Boltzmann factor. This concentration represents the equilibrium between the thermal generation and recombination rates. In doped semiconductors, the majority carrier concentration can be considered nearly equal to the doping level[7], while the electron minority carrier concentration n_p is given by

$$n_p = n_i \cdot e^{-\frac{E_i - E_f}{kT}} \tag{1.4}$$

where E_i is the intrinsic Fermi level and E_f is the electron quasi-Fermi level. The same equation is valid for holes in the n side, provided that the sign in the exponential is changed. At equilibrium by the law of mass action the product np is equal to n_i^2. So from equation 1.4 this leads to $E_{fn} = E_{fp}$.
The charge transport can occur by drift or diffusion, so, for electrons,

$$\vec{J_n}^{drift} = qn\mu_n\vec{\nabla}\phi \tag{1.5}$$

$$\vec{J_n}^{diffusion} = qD_n\vec{\nabla}\Delta n \tag{1.6}$$

where q is the unit charge, μ_n is the drift mobility and D_n is the diffusion coefficient. Analogous equations hold for holes. By Einstein relation, the diffusion coefficient can be related to mobility:

$$D = \mu \cdot \frac{kT}{q} \tag{1.7}$$

It is also convenient to define the lifetime τ for minority carriers as the exponential decay time in recombination processes, and the diffusion length as $L_{diff} = \sqrt{D\tau}$. Its meaning is similar to the mean free path for molecules in a gas phase, but here collisions are recombination events.
When excess carriers are injected or generated in a semiconductor they recombine, with a rate proportional[8] to the displacement from the equilibrium concentration n_0; for electrons

$$R = \frac{n - n_0}{\tau} \tag{1.8}$$

[7]We are assuming that all the donors are ionized at room temperature, that is reasonable for shallow donors at 300K.

[8]This is true for low-injection conditions.

This is of course the easiest way to take into account recombination effects. More complicated expressions are also well known and used, like the Shockley-Read-Hall (SRH) recombination [7], to accurately deal with deep defects in semiconductors.
We can write now the continuity equation for a semiconductor, putting together the drift and diffusion components of the current and generation (G_n) and recombination (R_n) rates.

$$\vec{\nabla} \cdot \vec{J_n} = q \left(G_n - R_n + \frac{\partial n}{\partial t} \right) \tag{1.9}$$

Let us reduce the problem to one dimension, with x directed from one side of the junction to the other, and simplify equation 1.9. We also consider steady state conditions, so time derivatives are zero by definition.

$$G_n - \frac{\Delta n_p}{\tau_n} + n_p \mu_n \frac{\partial E}{\partial x} + \mu_n E \frac{\partial n_p}{\partial x} + D_n \frac{\partial^2 n_p}{\partial x^2} = 0 \tag{1.10}$$

Here $E = d\phi/dx$ is the modulus of the electric field. This equation is known as the *drift-diffusion* equation, and together with its hole counterpart describes the electric behavior of the p-n junction, provided that suitable boundary conditions are set. For example one can assume perfectly ohmic contacts, so that the minority carrier concentration infinitely far away from the junction equals its equilibrium value:

$$n_p(\infty) = n_{p0} \longleftrightarrow \Delta n_p = 0 \tag{1.11}$$

For solar cells more complicated boundary conditions are used, that take into account surface recombination effects or back surface field layers that reduce the collection of minority carriers[9]:

$$\frac{\partial \Delta n_p}{\partial x} = \frac{S_n}{D_n} \Delta n_p \tag{1.12}$$

In real cases the surface recombination velocity S can depend on the voltage bias, making the calculation a bit more complicated.

[9] Actually the ohmic contact is nothing but a surface with infinite recombination velocity for minority carriers, while the perfect back (or front) surface field should have zero recombination velocity.

It is very important to understand that p-n junction solar cells are minority carrier devices and their behavior is governed by thermal diffusion. In fact by making the gradient of equation 1.4

$$\vec{\nabla} n = \frac{n_i}{kT} e^{\frac{E_f - E_i}{kT}} \left(\vec{\nabla} E_f - \vec{\nabla} E_i \right) = -\frac{qn}{kT} \vec{E} + \frac{n}{kT} \vec{\nabla} E_f \qquad (1.13)$$

since $\vec{\nabla} E_i = q\vec{E}$. Now, substituting the previous equation and equation 1.7 in the expression of the current density, we have

$$\vec{J_n} = q\mu_n n\vec{E} - qD_n \vec{\nabla} n = qn\vec{E} \left(\mu_n - \frac{qD_n}{kt} \right) + \frac{qD_n n}{kT} \vec{\nabla} E_f = \mu_n n \vec{\nabla} E_f \qquad (1.14)$$

The hole counterpart has of course the same shape. This means that currents can only flow in case a gradient of quasi-Fermi levels exist. That's why quasi-Fermi levels are called also the electrochemical potentials, since they govern fluxes of matter (charge carriers) driven by concentration inhomogeneities and/or electric fields. From this point of view it's clear what happens when a p-n junction is formed: firstly there is a concentration gradient between the two sides, so diffusion occurs, but as diffusion takes place, recombination of minority carriers leaves a depletion region at the junction. In this region a static electric field is present, due to the unbalanced nuclear charges of donors and acceptors, that drives carriers in opposite direction than diffusion. This lasts until the diffusion component is balanced by the drift component and the electro-chemical potentials difference becomes zero. The static field at the junction gives the built-in potential, that acts as a barrier for holes towards the n side and for electrons towards the p side (figure 1.5). If an external field is applied, in reverse bias conditions (p side grounded, n side at positive potential) the barrier height is enlarged and diffusion becomes even more unlikely, while in direct bias conditions (p side at positive potential, n side grounded) the barrier height is reduced and current can flow.
Going back to the drift-diffusion equation 1.10, in the neutral region of the diode, that is outside the depletion region, the solution with ohmic boundary conditions is:

$$\Delta n = n_{n0} e^{-\frac{x - W_n}{L_n}} \cdot \left(e^{\frac{qV}{kT}} - 1 \right) \qquad (1.15)$$

where W_n is the depletion region width on the n side of the junction[10]. Summing with the hole component, the total current across the junction in the dark can be written as:

$$J = J_0 \left(e^{\frac{qV}{kT}} - 1 \right) \tag{1.16}$$

When light is shone over the solar cell, a photocurrent generation term must be added from equation 1.2 into 1.9 and 1.16 becomes:

$$J = J_0 \left(e^{\frac{qV}{kT}} - 1 \right) - J_L \tag{1.17}$$

If SRH recombination were taken into account a $exp(qV/2kT)$ would be included in the diode equation 1.16.

$$J = J_{01} \left(e^{qV/kT} - 1 \right) + J_{02} \left(e^{qv/2kT} - 1 \right) - J_L \tag{1.18}$$

All the effects of doping, recombination and boundary conditions (that is the effective structure of the device) are included in the J_{01} and J_{02} terms, while the generation (light absorption effects) are included in J_L. Numerical software is often used to model devices: these codes solve the drift diffusion equations with customizable structures, recombination effects (like Auger), energy barriers and so on. Equation 1.18 describes the so-called two-diode model for solar cells, that can be found in figure 1.7. Often a single diode model is used to fit experimental data, but in the exponential a factor $qV/\eta kT$ is used, where η lies between 1 and 2. The closer to 1, the more the solar cell resembles an ideal diode, while the closer to 2, the more important are the space charge region recombination effects.

Let us now consider equation 1.4, in the case the n-type region is grounded and the p-type region is at a voltage V corresponding to the voltage generated by the solar cell. Let μ be the electrochemical potentials, we have:

$$n = n_i e^{(E_i - \mu_n)/kT} \tag{1.19a}$$

$$p = n_i e^{(\mu_p - E_i - qV)/kT} \tag{1.19b}$$

[10]Explicit expressions for W_n or V_{bi} can be found in [7].

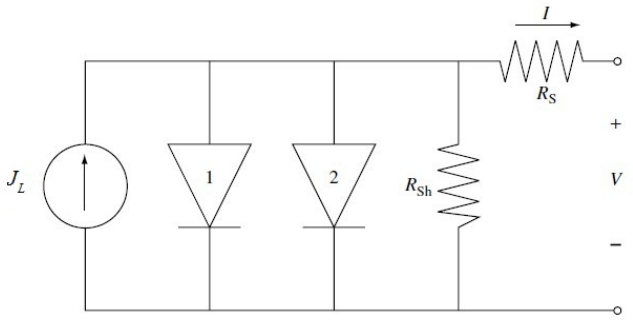

Figure 1.7: Two-diode model for solar cells. The solar cell is a dc current generator, with two diodes with different characteristics in parallel and parasitic resistances.

and this, for the law of mass action means[11]

$$qV = \mu_n - \mu_p \tag{1.20}$$

This result is very important in understanding the physics of the photovoltaic devices.

The most important parameters that describe the JV characteristic of a solar cell are: the short-circuit current density J_{sc}, which depends on the absorption spectrum and on the injection level and represents the maximum current output by the solar cell; the open-circuit voltage V_{oc}, which depends primarily on the energy gap, material quality, defects and injection level; the fill-factor FF, which is a figure of merit describing how much the JV curve resembles a rectangle: it is the ratio between the maximum power output by the cell and the product between the maximum current and voltage in the IV curve.

$$FF = \frac{V_{mpp} I_{mpp}}{V_{oc} I_{sc}} \tag{1.21}$$

[11] A more rigorous treatment can be found in [7] and in [11]. All of them rely on the fact that at the contacts the quasi-Fermi levels keep their equilibrium values and they are uniform throughout the depletion region.

Another very important parameter is the efficiency of the device, defined by

$$\eta = \frac{P_{out}^{max}}{P_{in}} = \frac{FF \cdot V_{oc} I_{sc}}{A \cdot I(AM_x)} \tag{1.22}$$

where P is the power, A the cell area and $I(AM_x)$ the spectral irradiance. Real devices also have non-ideal parasitic resistances and capacitances. Since solar cells are steady state devices, capacitance effects can usually be neglected. Some solar cells, especially at high current, show a deviation from the exponential diode law that bends the IV curve towards linear behavior: this effect can be modeled with a resistance in series to the diodes. Figure 1.8 shows the effect of an increasing series resistance in a silicon solar cell. On the other side, some cells, especially in reverse bias, show a deviation from the exponential diode law, like if the current had an alternative path and could leak from the diode: this effect can be modeled with a resistance in parallel to the diodes, and the effect of this so-called shunt resistance is shown in figure 1.9. Real devices, especially in the case of prototypes, may suffer from both series and shunt resistance problems. It can be quite challenging to understand which is the origin of these leakages, since if they are of significant entity, the IV curve deviates a lot from ideality and is not easy to interpret. Finally, this is the real solar cell equation with parasitic resistances included, describing the circuit in figure 1.7.

$$I = -I_{sc}^{*} + I_{01}(e^{q(V-IR_S)/kT} - 1) + I_{02}(e^{q(V-IR_S)/2kT} - 1) - \frac{V - IR_S}{R_{Sh}} \tag{1.23}$$

Since this equation is implicit, it is also not easy to fit to experimental data and estimate the values of the parasitic resistances.

1.4 Limits of photovoltaic energy

As correctly pointed out in figure 1.3, solar energy has by far all the potential to satisfy the world energy needs. In spite of that, since it is spread out over the entire Earth surface, its energy density is rather low compared to fuels: only to have a reference, one needs a

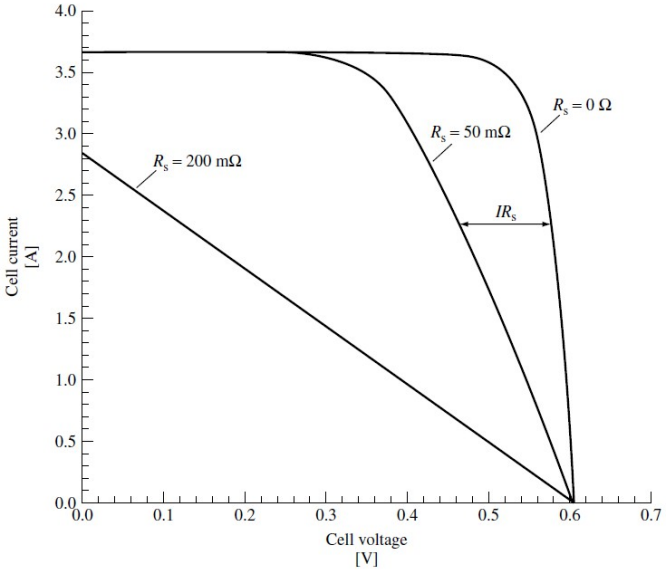

Figure 1.8: The figure shows a silicon solar cell IV curve, and how it changes with the addition of an increasing series resistance, from [11]. Please note that in [11] the sign convention for currents is the opposite to what has been used in this chapter. With our convention the figure looks symmetric respect the voltage axis.

more than 33 hectares wide solar farm[12] to generate enough power to replace a 50MW traditional plant. This translates into higher costs per unit area for the same power density. If the efficiency of PV devices were increased, less area would be needed. To achieve also the cost reduction goal, it's important to keep the same materials and manufacturing costs, or switch to less expensive ones. In this section the most important mechanisms that limit conversion efficiency in PV cells are reviewed. Their understanding is fundamental in order to conceive devices that exploit different physical phenomena to convert sunlight into electricity.
In the previous sections we described the solar cell from the semiconductor device point of view. This is of course correct and gives

[12]Assuming $150W/m^2$ generation capacity, average for Si PV modules.

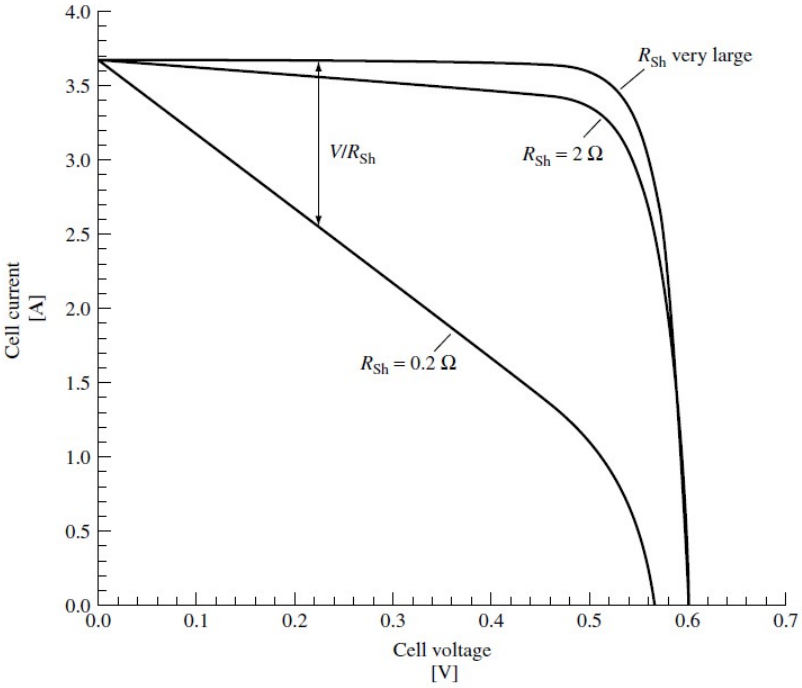

Figure 1.9: The figure shows a silicon solar cell IV curve, and how it changes with the addition of an increasing shunt resistance, from [11]. Please note that in [11] the sign convention for currents is the opposite to what has been used in this chapter. With our convention the figure looks symmetric respect the voltage axis.

good insight on what are the most important physical processes that allow the operation of a solar cell. Anyway it is important never to forget that since solar cells are energy conversion devices, thermodynamics apply in deeper sense than only charge carrier statistics. A thermodynamic approach can give a different and interesting point of view about the energy conversion mechanism of photovoltaic cells.

In order to understand the ultimate efficiency limit, let us consider a solar cell as an ideal reversible Carnot engine, generating electri-

cal work with the heat transfer from a high temperature reservoir (the Sun, T_H =5750K) and a low temperature reservoir (the Earth, T_L =300K). The efficiency of this machine can be easily calculated from

$$\eta_{Carnot} = 1 - \frac{T_L}{T_H} \simeq 94.5\% \tag{1.24}$$

Actually a more correct picture was given by Landsberg [14], introducing the concept of irreversible radiative heat transfer: in fact solar power is delivered to the Earth by the Stefan-Boltzmann law, and not by infinitesimal quasi-equilibrium thermal transfer[13]. Moreover, even though very small and usually negligible, also the solar cell radiates some blackbody[14] heat back to the Sun. As a finite-temperature-difference heat transfer, blackbody radiation involves some generation of entropy, which lowers the Carnot efficiency to 93.3%. If also entropy generation can occur in the process of absorption and emission of light by the solar cell, the efficiency limit is set to 86.8% [15]. These values become even lower if one considers that sunlight arrives to the Earth within a finite angle of view, determined by the distance and reciprocal sizes of Sun and Earth. An upper bound of 68.2% is calculated for photovoltaic conversion [5] [15] with AM1.5G spectrum.

All of the above mentioned calculations don't take into account the energy gap of semiconductors. In this, they are indeed more general and can be applied to many different systems[15]. Nevertheless for our purposes it is necessary to focus the attention on semiconductor physics. There are two fundamental effects in a semiconductor solar cell that limit the efficiency, that are inherent to the light absorption threshold process in semiconductors. First of all, the energy in excess of the bandgap (the absorption threshold) is rapidly lost as heat; then, the energy carried by sub-gap photons is lost. In fact when a photon is absorbed, the generated exciton will readily lose its energy (the same as the generating photon[16], that can be even

[13]This is sometimes referred to as the Stefan-Boltzmann thermodynamical engine.

[14]It is important to notice how the blackbody radiation is negligible, while luminescent radiation is not. In fact luminescence is the key physical mechanism that governs the detailed balance, as shown in the following.

[15]Even photosynthesis can be described with this approach, as done in [14]

[16]In indirect bandgap materials there is also the phonon contribution to be considered.

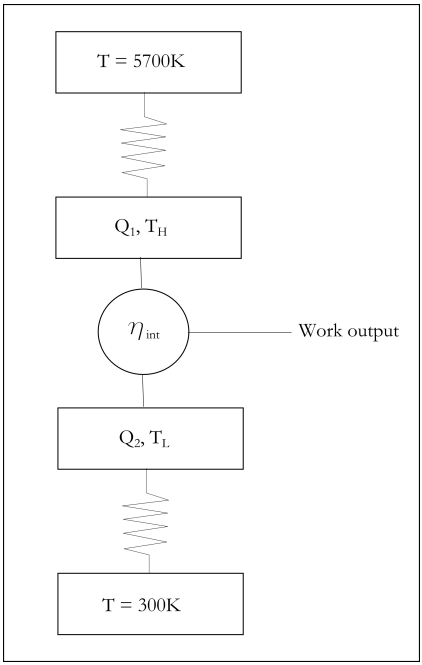

Figure 1.10: Scheme of an endoreversible thermal engine. The primary source is the Sun at 5700K, while the low temperature reservoir is the Earth at 300K. Irreversible radiative heat transfer couples the sources with the engine.

twice or three times the bandgap) with multiple electron-electron or electron-phonon scattering events. These scattering processes are very fast (on the femtosecond scale) and leave the conduction and valence bands populated only near the band edges, in thermal equilibrium with the lattice. This process is known as thermalization of hot carriers. In the case of photons with energy lower than the bandgap, absorption is not possible, so the long wavelength parte of the solar spectrum cannot be exploited. A reduction in the bandgap will mitigate the effect of the long wavelength missed absorption, but it will enhance thermalization effects. An increase in the bandgap on the other side will mitigate thermalization losses but will enlarge the missed absorption band.

Equation 1.20 states an extremely important concept: the output

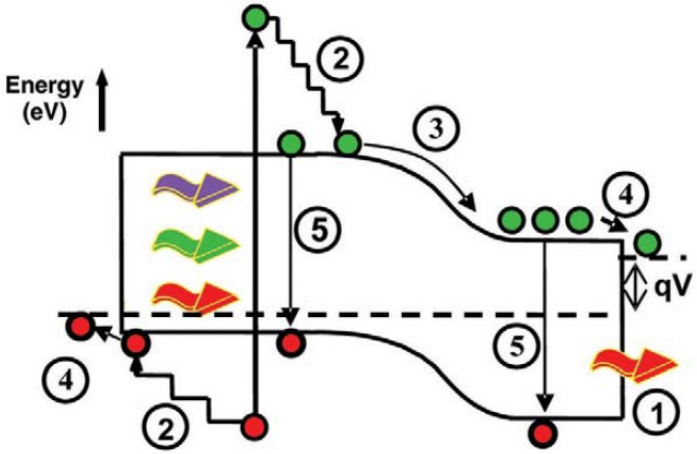

Figure 1.11: This figure shows the loss mechanisms in single junction solar cells: (1) missed absorption of low energy photons (2) thermalization of hot carriers (3) junction loss (4) non-ideal contacts (5) recombination. From [19].

voltage in a solar cell equals the difference between the chemical potentials at the output poles of the device[17]. In the case of ordinary bulk semiconductors, the chemical potentials of electrons and holes lie inside the bandgap. This means that their difference can at most be equal to the bandgap. We can extremely simplify the solar cell as a current generator with constant voltage equal to the bandgap. The current output can be calculated assuming complete absorption and collection for light with energy above the bandgap, from a blackbody spectrum of 5750K. The power output will simply be the product, as if the diode characteristic were a rectangle instead of an exponential. The efficiency vs bandgap curve is shown in figure 1.12. Even though it is a very rough estimate, this curve

[17]Even though this has been shown here only for the specific case on p-n junctions, this result is valid in general for any energy conversion device operating with two electric poles, as it comes from the fundamental laws of thermodynamics, as well explained in [5] and [12].

provides the correct shape and position for the maximum, between the bandgaps of Si and GaAs.

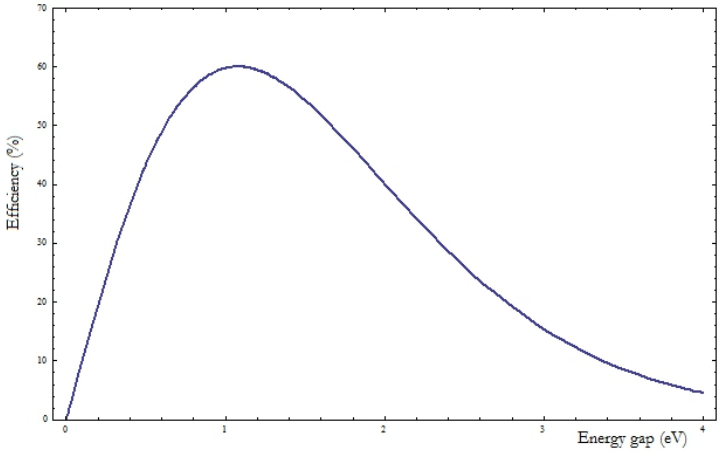

Figure 1.12: Efficiency curve as a function of the bandgap of a single-junction photovoltaic cell for a 5750K blackbody spectrum. The current is calculated assuming total absorption and collection of above-gap light, the voltage is set equal to the bandgap and the diode characteristic is approximated by a rectangle.

Going back to the thermodynamical picture, we can clearly understand how missed absorption can be thought of as heat transferred directly to the low temperature reservoir, while thermalization is an entropy generation mechanism. Shockley and Queisser have applied these thermodynamical arguments to the physics of single junction solar cells [16], introducing the concept of the radiative limit: the detailed balance counterpart of the generation process that occurs when a photon is absorbed is radiative recombination, releasing a photon with energy equal to the bandgap. By detailed balance arguments Shockley and Queisser could account for entropy generation mechanisms in solar cells (that were neglected in the calculation shown in figure 1.12) and calculate the ultimate efficiency limit

of nearly 41% for maximally concentrated sunlight[18] and 31% for an irradiance level comparable to AM1.5. An important assumption to get this result is that charge carriers undergo perfect collection, or have infinite mobility. GaAs solar cells of 29% efficiency have been demonstrated [17], meaning that the Shockley-Queisser limit is not so out of reach. In less efficient devices, incomplete light absorption, reflection, parasitic resistances, non ideal electrical contacts, non-radiative recombination processes or other types of defects can significantly lower the efficiency and degrade device performance.

Single junction PV devices poorly exploit sunlight for all the reasons explained above. The so-called third generation photovoltaics is a collection of the novel physical concepts proposed to overcome the efficiency limit for single-junction devices [15]. The tailoring of the absorption spectrum of semiconductors to the solar spectrum is exploited in multijunction (or tandem) solar cells: the devices are made either of a monolithic or mechanical stack of different bandgap single junction sub-cells. Each subcell absorbs a part of the solar spectrum with the best efficiency in that range; the series connections allows a high voltage output, while concentration optics can provide extremely high current output. So far [17] the best PV device is a triple junction solar cell with InGaP/GaAs/InGaNAs subcells, scoring 43.5% at 418X concentration. From the theory it is possible to calculate that a multijunction cell with infinite number of absorbing layers, thus perfectly matched to the solar spectrum, could achieve 86.8% efficiency at maximal concentration. This should not be a surprise, as this is the same number obtained for a cell without any loss mechanisms[19].
If tandem cells represent a way to adjust the absorption of semiconductors to sunlight, it is also possible to adjust the solar spectrum to single junction cells: this is done with up or down conversion layers, that enrich the solar spectrum of blue or red photons respectively. Coupled with traditional cells optimized to work in the blue or in the red end of the solar spectrum, they can increase the efficiency from the Shockley-Queisser limit.

[18] This is set to about 46000 times to Earth by the geometry of the solar system.

[19] As light coming from radiative recombination from top cells can be absorbed by bottom cells, overcoming somehow the radiative limit.

The radiative limit is based on the fact that in bulk semiconductors carrier relaxation times are much faster than diffusion (so collection from a device) times. That's why it is correct to assume that thermalization sets all the excited carriers very close to the band edges, and why the quasi-Fermi levels must lie inside the energy gap. But if carrier cooling were slowed and hot carrier collection with selective energy contacts were enabled, it would be possible to reduce significantly themalization losses and achieve higher voltage outputs. A detailed analysis of hot carrier devices is provided in [15].
The other key assumption leading to the radiative limit is that each absorbed photon can generate only one electron-hole pair, even if its energy is twice the bandgap or more. Multiple exciton generation has been demonstrated in novel devices with nanostructures [20], leading to quantum efficiencies higher than one. In fact nanostructures, thanks to their spatially confined energy levels, avoid the constraint of conservation of crystal momentum that makes so unlikely multiple exciton generation in bulk semiconductors.
A completely different approach is exploited in multiple band (or intermediate band - IB) devices: their goal is the introduction of energy bands inside the main bandgap of the semiconductor. If this can be achieved, subgap photons can promote the excitation of carriers in the intermediate band(s) and eventually in the main conduction and valence bands, thus extending the absorption coefficient of the semiconductor to lower energies without reducing the main bandgap. If the chemical potentials of electrons and holes at the contacts are kept at the same levels as without any intermediate bands, the output voltage is preserved and the efficiency is increased. Calculations show that the ultimate efficiency limit for this kind of devices is as high as 63.8% [21]. Intermediate band solar cells are the subject of this work, and in the following chapter the physics of these devices will be described. A small review of other PV technologies, fron old to new concepts, can be found in [18].

CHAPTER 2

INTERMEDIATE BAND SOLAR CELLS

In this chapter we will introduce the physics of the intermediate band (IB) solar cell. After a brief introduction about the physics of the IB devices, we will survey the state of the art in this field, showing different implementations of the IB concept realized so far. Particular focus is put in particular on nanostructured materials, for they represent the approach presented in this work to prove experimentally the effectiveness of IB devices. Special attention will be given to the requirements of nanostructured layers to get a working and efficient solar cell.

2.1 Theory

Since its introduction in 1997 [21], intermediate band solar cell have received the attention of a large number of research groups, due to the potential of the intermediate band to increase the ultimate efficiency of photovoltaic devices from 41 to 63% under maximal concentration of sunlight. The key working principle of the intermediate band solar cell have been demonstrated in a InAs/GaAs

quantum dot solar cell [22], though so far to the knowledge of the author no net increase of the efficiency has been shown by an IB device respect to a device with the same characteristics but lacking the IB. Reviews of the topic can be found in references [23] and [24].

Many authors report strong enhancement of the photocurrent [25] due to sub-gap absorption, and even large increase in efficiency compared to reference devices [26]. Sablon et al. [26] fabricated InAs/GaAs quantum dot solar cells and reported a large increase in current (more than 60%) without significant voltage degradation. They also report the production of a large photocurrent due to sub-gap light only, but no spectral selectivity on the different IB-related transitions has been measured. So, even though it is very likely to be an IB solar cell, it is has not been demonstrated that the IB working principles, as explained in the following, are fulfilled.

The intermediate band design for the increase of solar cell efficiency has been explored from a thermodynamical point of view in many papers (see references [27] to [46]). The field has expanded a lot, as much to include novel designs of tandem cells including IB subcells (from [48] to [50]), or to propose materials that show an intermediate band without the insertion of nanostructures (from [35] to [39]).

The band diagram in real space of an intermediate-band solar cell is shown in figure 2.1: an intermediate band (IB) is present in the main energy bandgap of a semiconductor (the host). If the IB is half-filled with electrons, photons with energy lower than the main bandgap can excite transitions from the valence band (VB) to the IB and from the IB to the conduction band (CB). For a photovoltaic device this means an extension of the absorption coefficient to lower energies, thus largely increasing the amount of current generated by sunlight. The current loss due to missed absorption of sub-gap photons is reduced in an IB solar cell, and efficiency increases, provided that the voltage output remains the same as without the IB. When sunlight is shone over a photovoltaic cell, the population of electrons and holes in the CB and VB respectively shifts from its thermal equilibrium value. This flux of matter (the electrons pumped from CB to VB) brings a change in the free energy of the

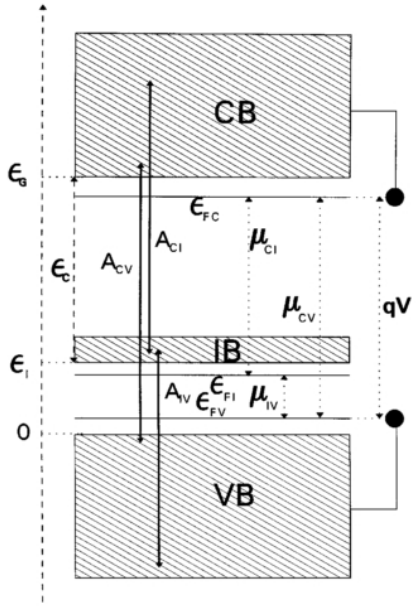

Figure 2.1: Band diagram of the intermediate band solar cell. From reference [21].

system, equal to the bandgap energy per electron[1]. As shown in the previous chapter, a chemical potential or quasi-Fermi energy μ can be introduced to describe the system: it contains information about the population and the net pumping ratio, including recombination mechanisms. At equilibrium we have shown in the previous chapter that:

$$n = n_i \cdot \exp\left(\mu_n - E_i\right)/kT$$

$$p = n_i \cdot \exp\left(E_i - \mu_p\right)/kT$$

By taking their product, that is equal to n_i^2, we know that $\mu_n = \mu_p$. When the photovoltaic cell is illuminated a term qV_{OC} has to be

[1]Light with energy above the bandgap excites electrons at higher energy, but this excess is lost nearly immediately by thermalization at the band edges.

added in the equations above[2], and by taking the product we have the following result:

$$qV_{OC} = \mu_n - \mu_p$$

that means that the output voltage of a solar cell is determined by the quasi-Fermi level splitting[3]. This splitting can be enhanced by increasing generation, that is by light concentration, and this is the thermodynamical reason why solar cells become more efficient as sunlight is concentrated. In a IB photovoltaic device, the presence of the IB introduces extra generation and recombination terms in the balance. A true intermediate band, as described in [21], should exhibit a quasi-Fermi level that is separated from the ones that describe VB and CB. If this occurs, electrical contacts aligned with quasi-Fermi levels of holes and electrons in a region where the IB is not present, can still extract carriers at a potential difference equal to the difference of quasi-Fermi levels of CB and VB. It is clear that strong recombination coupling with the IB would lower the quasi-Fermi energy splitting, maybe to the extent that the IB pins one of the quasi-Fermi levels of CB or VB and the effect is a dramatic voltage output reduction[4]. A separated quasi-Fermi level for the IB is thus necessary for the photovoltaic device to preserve the output voltage and increase the efficiency, thanks to the increased current generation. It is interesting to point out that since the splitting depends on the balance between generation and recombination mechanisms, it can be enhanced with high levels of light concentration.

Calculations show (figures 2.2 and 2.3) that at maximal concentration the efficiency can rise up to 63%, to be compared with 41% of single-junction devices, for a main bandgap of 1.9 eV and a CB-IB bandgap of 0.7 eV [21].

Specific device models have been proposed to describe the operation of IB solar cells. The most important points of those models regard the description of optical transitions involving the intermediate band and the generation recombination currents involving the

[2]Because the solar cell is in working conditions.

[3]In particular by the splitting at the contact poles of the device.

[4]That is exactly what happens when a single-junction solar cell contains a large number of defects active as recombination centers.

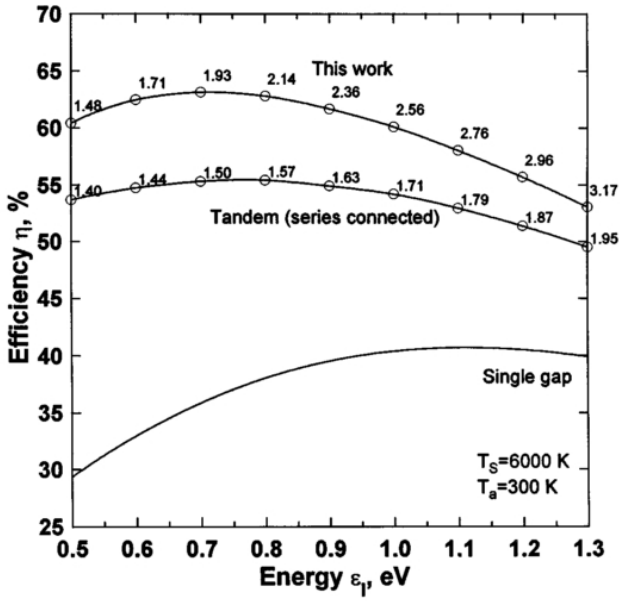

Figure 2.2: Efficiency calculation for an ideal IB device, compared to triple junction tandem and single junction solar cells. From reference [21].

intermediate band (references [41] and [28]). The drift-diffusion equations of the solar cell can be modified in order to include the subgap photocurrent (see figure 2.4): the electrical model consists of the host semiconductor diode, describing the VB-CB transitions, paralleled by two other diodes in series, describing VB-IB and IB-CB transitions. The models proposed also include space-charge and other recombination effects to best fit the experimental data. A complete description can be found in references [42] to [44].

2.2 QD-IBSC

The most explored strategy to realize an intermediate band material is the insertion of nanostructures into a semiconductor. This is

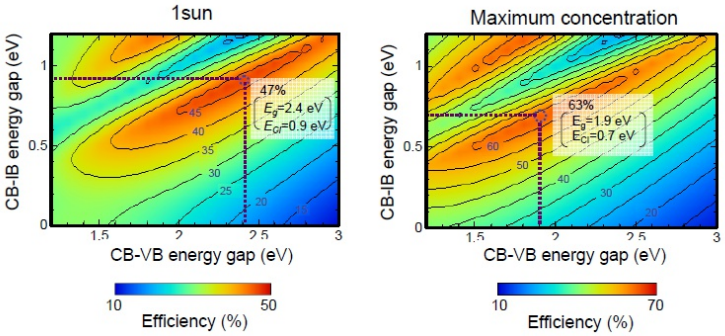

Figure 2.3: Efficiency calculation for an ideal IB device as a function of the bandgaps, for 1 sun and maximal concentration. From reference [40].

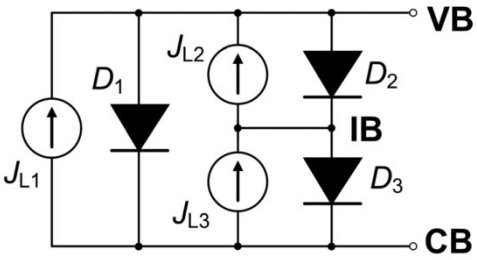

Figure 2.4: Equivalent circuit for the intermediate band photovoltaic cell, showing how the main VB to CB generation path is paralleled by the series effect of the two-photon absorption involving VB to IB transitions and IB to CB transitions. From reference [42].

because size tuning allows for the engineering of the energy levels of the nanostructures, that by quantum confinement are inserted into the main bandgap of the semiconductor host. Quantum dots in particular have the correct delta-like density of states required to form an intermediate band that has a separate quasi-Fermi level from the conduction and valence band of the host semiconductor [51]. Quantum wells and wires instead share the unconfined properties of the bulk in the dimension(s) other than the confined one(s). The presence of unwanted states may increase the (thermal) cou-

pling between the IB and the CB (or VB), with deleterious effects on the separation of the quasi-Fermi levels.
The IB behavior has been demonstrated in GaAs solar cells containing InAs quantum dots ([22] and [52]) grown by MBE. Recent progress has also been made with the growth of InAs/GaAs quantum dot solar cells with MOCVD [53] and even transfer to flexible substrates by epitaxial lift-off [54]. Even though a lot of research is active in the field (see for example references from [55] to [59]), only the first works by Luque and Martì show deep investigation of the IB behavior, by checking for two-photon absorption and splitting of the quasi-Fermi levels. As an example I report in figure 2.5 the quantum efficiency measurement for a quantum dot solar cell made of GaAs with a multistack of InAs quantum dots: such a measurement does not prove IB behavior, but only the extension of the absorption coefficient to longer wavelengths. This occurs naturally in bulk semiconductors when the bandgap is lowered (that is what happens in the quasi-Fermi level of CB and IB merge), and could easily explain the reported decrease in V_{OC} respect to the GaAs reference sample. However, this measurement cannot exclude IB behavior as well, because two-photon transitions (from VB to IB and then from IB to CB) can be excited by monochromatic photons with energy lower than the VB-CB gap, provided that the related absorption coefficients are non-zero at that energy. Potentially, multistacks of quantum dots like those reported in the literature can be good candidates for efficient IB solar cells, but true IB behavior must be checked.
A possible limitation to this technology comes from strain-induced defects that can generate in the quantum dot layers [57], and eventually limit the number of layers that can be grown. Higher densities of quantum dots in strain compensated materials have been proposed and realized (see references [60] to [66]). The effect of strain compensation is beneficial in reducing dislocation density, and so in avoiding the degradation of the above-gap photoresponse. In this systems a net efficiency increase is expected, because there is a significant extension of the photoresponse to below-gap energies. The issue of voltage preservation however is still present in these devices, so that no efficiency increase has been observed so far.
An interesting feature of strain-compensated quantum dot multilayers is the self-ordering effect observed in multilayered samples

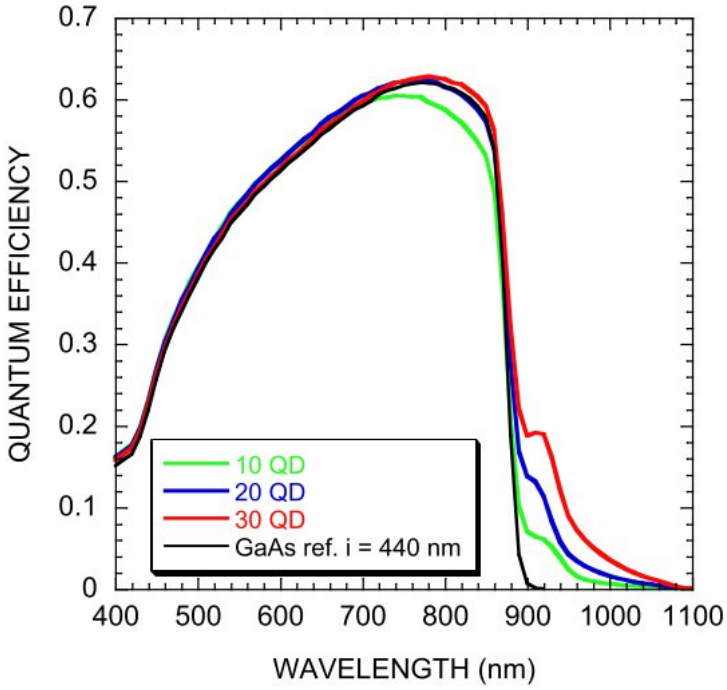

Figure 2.5: Reported quantum efficiency measurement of a InAs/GaAs quantum dot solar cell. From reference [55].

[67]. This ordering may lead to the formation of a miniband that would serve as the perfect IB as theorized in [21].
An important drawback of the Stranski-Krastanov technique used to grow InAs quantum dots is the presence of the wetting layer, that introduces unwanted quantum-well-like states along with the dot states, that can assist the escape of carriers from the IB (and thus couple the quasi-Fermi levels of IB and CB) through tunneling or phonon interactions.
In this work $Al_{0.3}Ga_{0.7}As$ solar cells containing GaAs quantum dots grown by droplet epitaxy are investigated as potential IB photovoltaic cells. $Al_{0.3}Ga_{0.7}As$ has a room temperature bandgap of

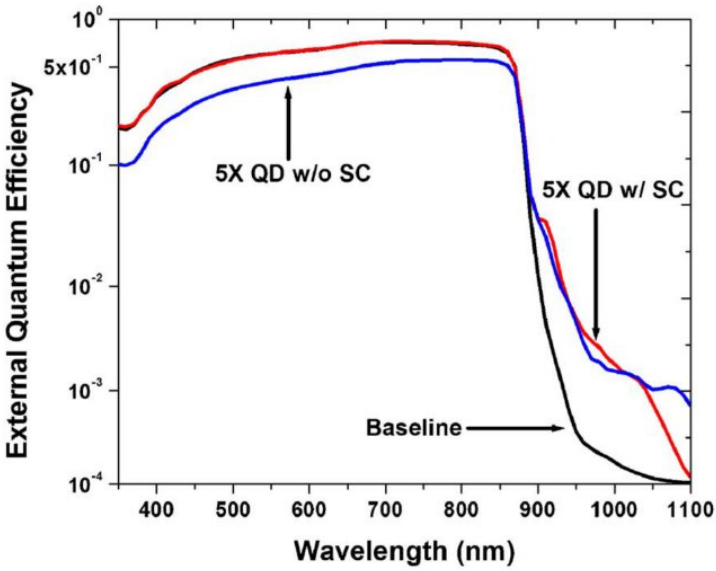

Figure 2.6: Reported quantum efficiency measurement of a InAs/GaAs quantum dot solar cell with GaP strain compensating layers. The effect of strain compensation removes dislocations and restores the baseline GaAs solar cell photoresponse at high energies. From reference [66].

1.8eV, that nearly matches the most efficient IB cell obtained from theoretical calculations ([21], see figures 2.2 and 2.3). By the band offset of $Al_{0.3}Ga_{0.7}As$ and GaAs, if it were only a CB offset, we could estimate the IB - CB bandgap to be at most around 0.4 eV; however the band alignment is type I and quantum confinement lifts the energy levels from the bulk band edges. As it will be shown in chapter 6, a reasonable value for the IB - CB bandgap is around 0.2 eV, that gives the $Al_{0.3}Ga_{0.7}As$/GaAs IB solar cell a maximum theoretical efficiency very close to the single junction values. Nevertheless, since it is a strain free system, research can provide results that are unaffected by defect behavior (like Fermi level pinning at dislocations). In fact the reason why quantum dot solar cells perform worse than the quantum dot - less counterparts reported has not been certainly attributed either to the

presence of crystal defects or to the presence of the IB. Moreover, lattice matched structures do not suffer from issues coming from the release of strain when multistacks are grown. Finally, droplet epitaxy can achieve high densities of quantum dots, thus increasing the effect of IB-related transitions, and the high aspect ratio of the nanostructures has been theorized to increase the absorption coefficient of IB-CB optical transitions [69], thus enhancing the possibility of a good quasi-Fermi level split and efficient IB device operation.

CHAPTER 3

SAMPLE STRUCTURE DESIGN

In this chapter the approach followed to design the photovoltaic device structures will be described. Numerical simulations will be shown, with which we could calculate the best-efficiency structure for the matrices AlGaAs cells that host the nanostructured IB layers. Special attention will be given to GaAs and $Al_{0.3}Ga_{0.7}As$ single junction heteroface solar cells, as they were the main steps of the approach to IB cells and served to define all of the device processing and characterization tools used. In this chapter the attention is pointed on how simulations can match experimental data for non-ideal devices and help to understand the various growth and post-growth processing issues present. In chapter 5 a detailed experimental analysis of the assessment of our manufacturing processes for single junction GaAs and $Al_{0.3}Ga_{0.7}As$ photovoltaic cells is presented. In chapter 4.3 instead a discussion of the processing steps is proposed. These three sections should be considered together as the first step of the project leading to intermediate band devices, as understanding of the host medium for the quantum dots has been achieved.

3.1 General guidelines

The design of a photovoltaic cell structure must take care of the many parameters present in the drift-diffusion equations illustrated in the previous chapter. However, since photovoltaic devices are meant to efficiently convert the absorbed sunlight, the starting point for strucure design is a simple calculation of the minimum thickness necessary to absorb all the above-gap sunlight. This can be done easily by calculating the transmittance of a homogeneous slab of semiconductor material as a function of thickness, from the Lambert-Beer extinction law.

$$I_T(\lambda) = I_0(\lambda) \cdot \exp\left[-\alpha(\lambda)x\right] \tag{3.1}$$

where α is the absorption coefficent of the semiconductor and x is the thickness of the slab. Since the absorption coefficient usually increases as the energy increases, complete absorption of above-gap light occurs whenever complete absorption of light with energy equal to the bandgap occurs. This means that a straightforward calculation of the penetration depth of light at the bandgap energy gives a very good estimate for the required thickness of the active layer of a solar cell. As an example, for GaAs, the absorption coefficient at 1.42 eV (room temperature bandgap) is $8 \cdot 10^3 cm^{-1}$ [70], that translates into a penetration depth of $1.25\mu m$. We may fix the thickness threshold for complete absorption at about 3 penetration depths. In the previous example, this means that the minimum solar cell thickness for complete light absorption is about $3.75\mu m$. For Si, being it an indirect gap material, the minimum thickness is about 2 orders of magnitude higher[1]. The concept of minimum thickness should not lead to think that thicker devices would perform better: in fact, as shown in the previous chapter, the solar cell's behavior is governed by diffusion of carriers, that can be described in terms of a diffusion length of minority carriers. This is in fact the second main constraint in the design, and depends on doping level and polarity, as well as (of course) the mobility of carriers in the semiconductor: a performing photovoltaic device needs a thickness comparable to the diffusion length of minority carriers

[1] Commercial Si solar cell as this as $180\mu m$ are currently manufactured, as the optical thickness is increased by light trapping techniques.

for efficient collection. An example of this will be shown in chapter 5 for $Al_{0.3}Ga_{0.7}As$ solar cells, for holes in n-$Al_{0.3}Ga_{0.7}As$ have very poor mobility and this leads to missed collection of the photogenerated carriers. It is opinion of the author that the best design from this point of view will be provided by plasmonic structures (see [71]), that can either concentrate light in the semiconductor film or let it flow in-plane, thus leading to complete absorption with cells thinner than the penetration depth. These techniques have not been explored in this work.

After defining a reasonable value for the thickness of the photo-

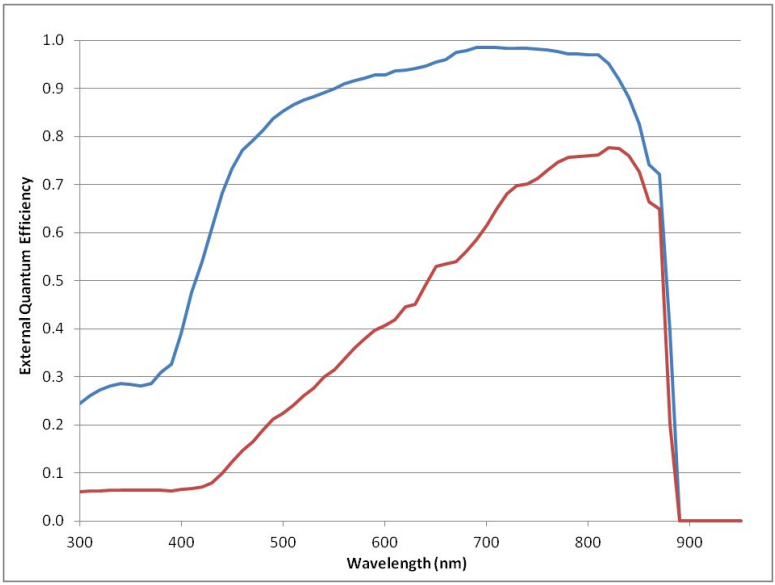

Figure 3.1: The graph shows the effect of a passivating window layer on the simulated spectral response of a GaAs solar cell.

voltaic cell, numerical simulation software was exploited to define the structure and doping levels of the device layers. One has to keep in mind some other important guidelines in designing the solar cell structure. The key element of the photovoltaic device, the p-n junction, is asymmetric. This is because light injection comes

from one side only[2] and the injection profile is exponentially decaying as light penetrates from the surface. Asymmetry is also in the choice of the doping polarity, that is made according to which is the minority carrier type with the longest diffusion length. For reasons of availability during the project, only n-type wafers have been used to manufacture the devices presented in this work, that are p-emitter on n-base.
The emitter air-exposed surface must be passivated in order to have good collection of high energy photons, with lower penetration depth. To this end, a window layer is used with higher bandgap, so that minority carriers diffusing towards the free surface are reflected back to the junction and can be collected. Passivation

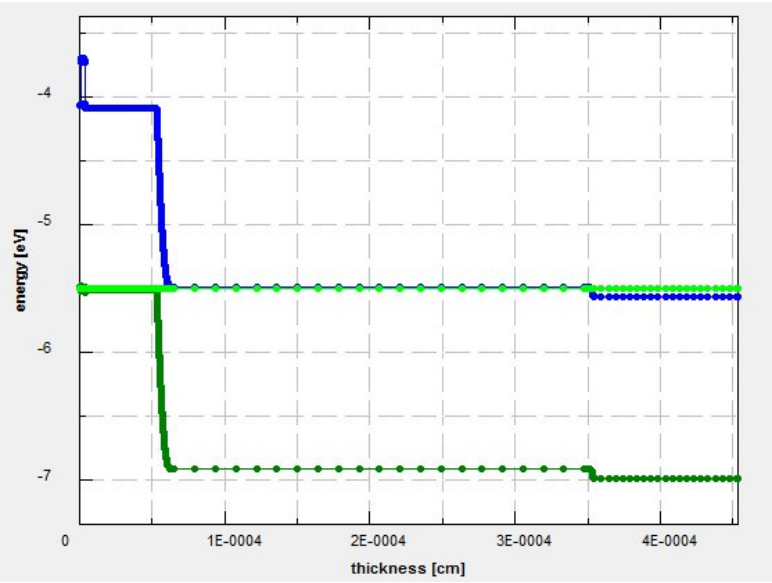

Figure 3.2: Band diagram in real space at 0V bias of a p-n GaAs solar cell.

of the front surface by a window layer improves the blue photoresponse of the photovoltaic device, as it is shown in figure 3.1, and

[2]Though bifacial solar cells are also produced, but they are not considered in this work.

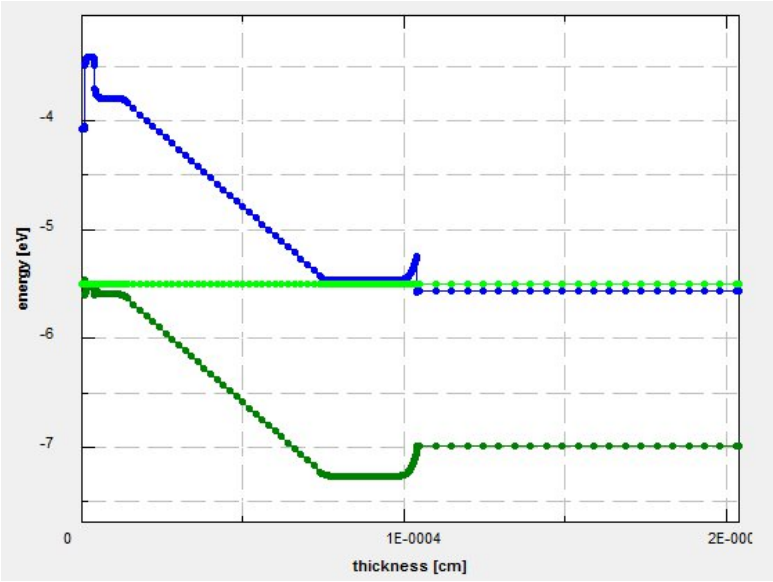

Figure 3.3: Real space band diagram at 0V bias of a p-i-n $Al_{0.3}Ga_{0.7}As$ solar cell. The GaAs substrate is also included on the right.

thus the short-circuit current and all the other figures of merit of the device are increased. For the window layer we used AlGaAs alloys that can be grown directly in the MBE chamber used for the manufacturing of the samples presented in this work. AlGaAs has a type I band alignment to GaAs, that can be modified by heavy doping in order to achieve a good ohmic contact for majority carriers and a reflection effect for minority carriers (see band diagram in figure 3.2). For an analogous reason (though there is no need for free surface passivation) also the base surface is separated from the wafer by a back surface field (BSF) [72], that has similar minority carrier reflection capabilities as the window layer. In this way the ohmic contacts can be fabricated over the window and BSF and these are not in contact with the minority carrier gases in the junction. In this way the open-circuit voltage can be increased [11]. The thickness of the window layer must be calibrated in order to avoid excessive light absorption before the junction: the use of a

few tens of nanometer thick high bandgap layer satisfies this need. In our case, to prevent oxidation of Al-containing layers, a 10nm-thick GaAs cap is grown. If anti-reflective coatings (ARCs) are to be deposited in the fabrication processes, usually thicker GaAs contact layers are grown to decrease contact resistance and are later removed by selective etching before the ARC deposition. This step has not been included in our processing, so the cap is not removed to prevent oxidation and it is kept thin to avoid a filtering effect.
The same considerations apply to p-i-n structures, that will be presented in this work (figure 3.3). The use of an intrinsic region ensures good charge collection (that is assisted by the static electric field in the intrinsic region) even in materials that show low diffusion length.

3.2 Numerical simulation

Several software packages are available for the simulation of photovoltaic devices, both commercial (like ATLAS [73], Sentaurus Device or LaserMOD PV module) and free (SCAPS [74], PC1D, AMPS, Afors-Het [75]). The advantages provided by commercial software packages are a good CAD environment for the structure design, a wide database of materials parameters, a modular structure that can be used to introduce different physical effect (from Auger to more complicated quantum transport effects, and recently to photon recycling effect [76], that is luminescence and re-absorption) and the possibility to run 2D or 3D simulations. However good results can also be obtained with more simple 1D free software packages. An introduction can be found in reference [77]. The main discrepancies between simulated and experimental data are due to inaccuracy in the parameters used for the simulation, like minority carrier mobility for example.
For the simulations performed in this work a wide set of data about the semiconductor parameters needed for the solution of the drift-diffusion equations was collected: only experimentally measured data for GaAs ([78] [79]) and $Al_{0.3}Ga_{0.7}As$ ([80]) were used, though a large number of models for mobility or diffusion length behavior have been proposed (see [81] to [85]).
Afors-Het version 2.4.1 was used to carry out the simulations re-

ported in this work. The software provides a graphical environment for the definition of the 1D structure of the solar cell and many measurement routines, like IV, EQE, CV, including temperature dependence and variable illumination spectra, totally controllable by the user. The precision used for the definition of the mesh grid used for solving the drift diffusion equations was set to 1 nm, while the energy precision was set to kT. Since no ARCs have been applied on our solar cells (yet), the optical model was a basic Lambert-Beer absorption discarding multiple reflections, that in our case are not important; the only reflective surface was set to be the front surface, calculated from Fresnel equations as for a thick film (no interference effects) with flat surface and light at normal incidence . The maximum number of iterations for the numerical solver was set to 10000 to avoid excessive simulation time. Flat-band ohmic contacts have been used, though the software implements also non-zero barrier height. Defects can be added in various fashions: single level, band tails or gaussian distribution, to be neutral or charged. The recombination model is Shockley-Reed-Hall, with defect energy levels and defects concentrations set by the user. The band diagram, including heterojunction offsets, is calculated automatically using user-defined work functions. Parasitic resistances (and capacitances) can be added in the external circuit, and were used to better match experimental data. As it will be shown in the next chapter, the presence of these resistances can be accounted for by non optimized post-growth processing.

It is important to remark that the role of numerical simulation in

Table 3.1: Comparison between the IV parameters of the best GaAs single junction photovoltaic cell fabricated in this work and numerical simulation of the same structure performed with Afors-Het.

	$J_{SC}(mAcm^{-2})$	ϕ_C (mV)	Fill factor	Efficiency
Simulation	17.70	982.8	81.9%	14.2%
Best GaAs	17.82	977.4	82.6%	14.0%

this work is to provide the structure for a performing solar cell made of GaAs and $Al_{0.3}Ga_{0.7}As$, in order to fabricate good devices, comparable with commercial or literature ones fabricated with similar techniques, and establish a reliable workflow that could be trans-

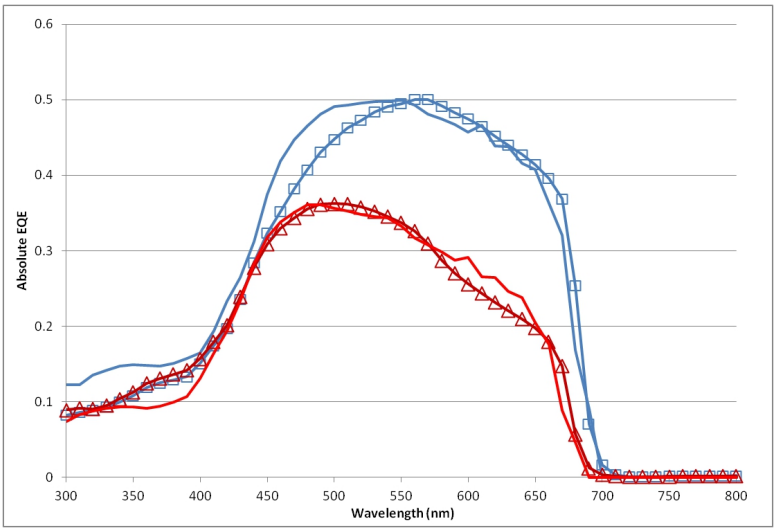

Figure 3.4: Comparison between measured data (with symbols) and simulations (continuous lines). Neutral traps were introduced in the n-type layers to account for small diffusion length. Red curves are p-n $Al_{0.3}Ga_{0.7}As$ solar cells, blue ones are p-i-n cells.

ferred to the quantum dot devices. This involved the understanding of growth and fabrication problems in the case of $Al_{0.3}Ga_{0.7}As$ photovoltaic cells, necessary to fix the issues encountered.
A small amount of defects was added in the n-base of the solar cells during simulations, in order to lower the unrealistically high open-circuit voltage (even 100mV higher that best literature-reported cells). The lowering of the V_{OC} in real devices comes from an increase in the dark current of the diodes due to recombination at the device edges, that cannot be simulated by 1D software, and this is the reason why simulations return higher V_{OC}s. In table 3.1 the figures of merit of our best GaAs cells are compared to the simulation results for the same structure, with fairly good match. The design of $Al_{0.3}Ga_{0.7}As$ photovoltaic devices proved to be more challenging, due to many troubles encountered (as discussed from the experimental point of view in chapter 5) that shift the measured IV characteristics from ideal simulated ones. As it will be explained

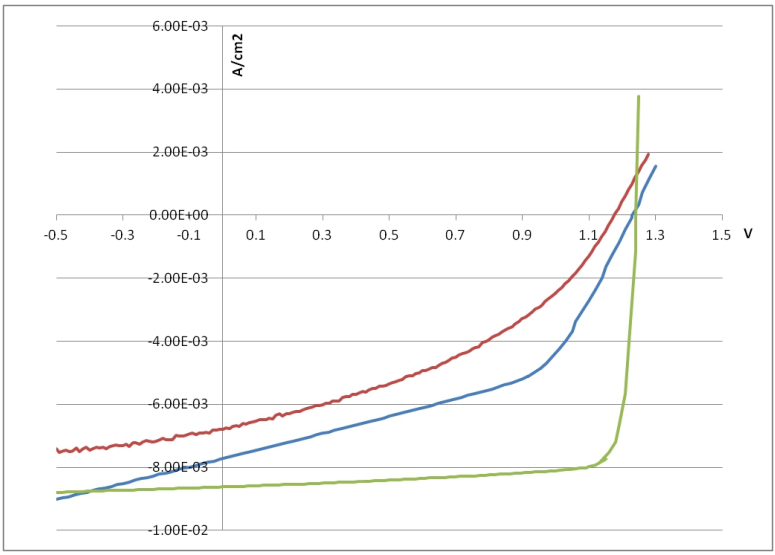

Figure 3.5: Comparison between measured data (red curve) and simulations of p-i-n $Al_{0.3}Ga_{0.7}As$. The green curve is the simulation without parasitic resistances, while the blue curve is with series and shunt resistances of values obtained from the fit of experimental data.

extensively in chapter 5, to match with experimental data it was necessary to introduce a significant (comparable to the doping level) density of traps, especially in n-type layers. This is because the diffusion length of minority holes is much shorter than predicted from the majority hole mobility data available, so charge collection is not complete. This effect can be accounted for in simulations by the introduction of trap levels, as it is shown in figure 3.4.
Parasitic resistance effects can also be simulated, and numerical calculation also proved very important in understanding the experimentally measured IV curves: in fact, as shown in figure 3.5 the effect of series and shunt resistance was added in simulation and a clear trend was obtained, that allowed to understand processing issues.

CHAPTER 4

DEVICE GROWTH AND FABRICATION

In this chapter the growth and fabrication processes used to realize our devices are described. In the first section Molecular Beam Epitaxy (MBE) is introduced from a very general perspective, since this technique was used to grow all of our samples. Nanostructured devices have been grown with the same machine, using the Droplet Epitaxy technique, that will be described in the second section. In the third section we will describe all the fabrication steps developed from scratch to realize working solar cells: the most critical points will be outlined in detail, showing experimental data of both working and non-working devices. This part of the work involved a great effort to assess a good and reliable process flow for the III-V devices.

4.1 Molecular Beam Epitaxy

Molecular beam epitaxy (MBE) is one of the most important techniques available for the growth of high quality semiconductor epilayers. One could describe MBE as an elaborated technique of

evaporation, that allows the growth of epitaxial layers with high crystalline quality, high homogeneity and control of alloy composition within 1%.
A typical MBE growth chamber, like the one present in L-Ness laboratory, Como, Italy, used for the growth of our samples, is illustrated in figure 4.1. MBE machines work in ultra high vacuum

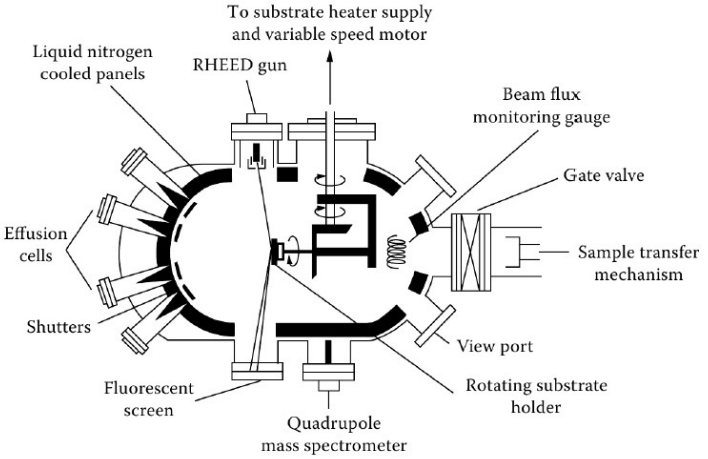

Figure 4.1: A typical MBE gen-II setup.

(UHV) regime, that is with pressures around or lower than 10^{-9} torr, to achieve not only ballistic transport towards the substrate, but also to ensure a high degree of purity and lack of contamination. In fact from simple mean free path calculations for an ideal gas, it can be found that at so low working pressures, the mean free path of atoms is some tens of meters. In gen-II research-scale machines, the distance between substrate and atomic sources is around 30 cm, so an upper limit to pressure of about 10^{-5} torr would be enough to ensure ballistic transport, that is atomic or molecular beams. The reason why ultra high vacuum is used is, as previously stated, to avoid the presence of any unwanted atomic species on the growth surface. This makes MBE unmatched from the point of view of impurity incorporation if compared to other

epitaxial techniques like MOCVD. UHV is achieved by combined use of turbomolecular pumps and cryopumps and at the occurrence, Ti sublimation pumps and ion pumps. The environment inside an MBE growth chamber must be kept particularly clean from unwanted atomic species, like carbon or oxygen for example. An introduction chamber isolated by a gate valve with a separate pumping system is used in a clean environment (such as a cleanroom or a laminar flowbox) to introduce and extract samples from the machine, and baking is used to degas the surfaces before the introduction to the growth chamber. The crystal quality can be monitored in-situ by a reflection high energy electron diffraction gun (RHEED). The RHEED is a high energy (tens of KeV) electron source, with a low grazing angle with the growth substrate: with a De Broglie wavelength of the order of 0.2 angstroms and the low grazing angle, RHEED electrons are Bragg reflected by the superficial atomic layers of the sample, giving a diffraction figure on a screen in case of a crystalline surface. The RHEED pattern can be interpreted as the 2D Fourier transform of the surface lattice, and gives important information about crystal quality, oxide desorption, 3D growth and surface reconstruction. For group III and group IV elements, solid source Knudsen cells are usually installed, while for V elements more complex designs are used, involving a cracking stage. Knudsen cells are basically made of a PBN[1] conic crucible with a tantalum heat shield, and are heated by tungsten filaments rolled around the crucible itself. Crackers consist of two stages, one is dedicated to the evaporation of elemental Ar, P or Sb (the most commonly used elements), while the other is kept at higher temperature to break the tetramers into dimers or monomers that ensure better growth quality. Mechanical shutters are placed in front of the effusion cells, that can be operated remotely fast enough to get abrupt or even single atomic layer interfaces. The control down to the atomic monolayer scale makes MBE probably the most powerful growth technique from this point of view. The possibility to install in a single chamber different effusion cells allows the growth of a large range of ternary and quaternary alloys of materials, whose composition can be precisely controlled within one percent.

[1] Pyrolitic Boron Nitride

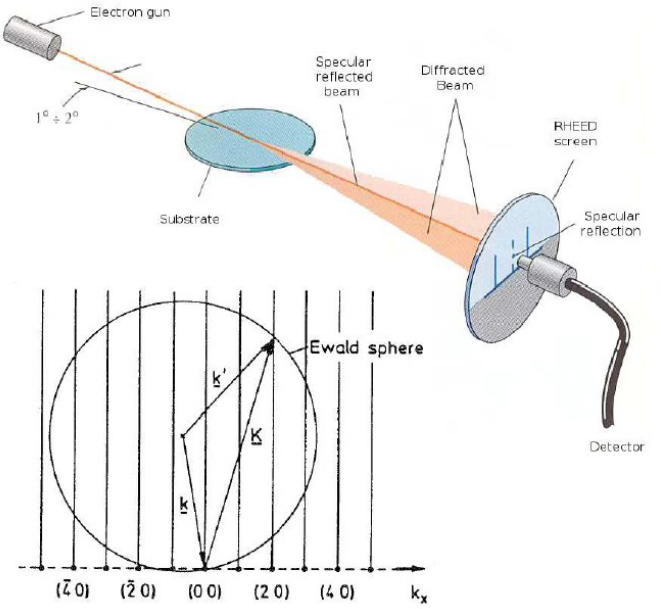

Figure 4.2: The drawing shows the geometry of the RHEED gun, and the inset represents the Ewald sphere in the plane of the sample, showing diffraction conditions.

MBE crystal growth results of a sum of different processes, as shown in figure 4.3. There is a dynamical equilibrium between atoms from the gaseous phase that stick to the surface and atoms from the solid phase (the sample surface) that re-evaporate. This equilibrium is determined by the partial pressure of that atomic species[2], the substrate temperature and the vapor pressure. Other important phenomena are interdiffusion between substrate and epilayer and surface diffusion. In particular surface diffusion is crucial for the crystalline growth: a high surface diffusion length allows the adatoms to bind at the proper crystal site during the growth. If the diffusion length is too small crystal defects may occur or in ex-

[2]But depending on the specific material chemistry, it may also depend on other species' partial pressures.

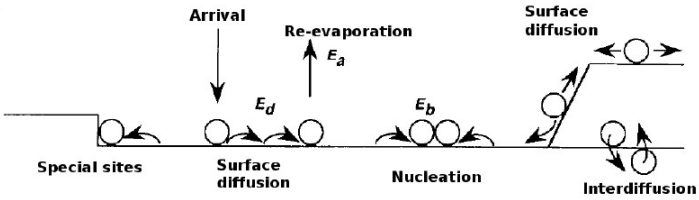

Figure 4.3: The figure shows the surface processes that lead to crystal growth from the gaseous phase: the main component comes from the balance between adsorption and re-evaporation. Surface diffusion plays an important role in determining crystal structure and shape, while interdiffusion affects mainly the composition of the grown layer.

treme cases, amorphous layers are grown. Surface diffusion is a key factor in three dimensional growth, as will be discussed in the following section, but also in the case of layer by layer growth. In fact when the growth starts, several nucleation seeds are formed, but the growth proceeds to completion of the monolayer before starting a new layer[3]. This explains the typical RHEED intensity oscillations, that are due to atomic layers interference that is fully constructive only when the new layer is complete. This phenomenon is exploited for precise calibration of the growth rate.

Vapor pressure is of utmost importance in determining the growth kinetcs. In fact, for the case of our interest, As has a very high vapor pressure at the usual growth temperature of 580°C, while for Ga or Al it is several orders of magnitude lower, as reported in figure 4.5. It is indeed true that those data refer to the phase diagram of the pure elements and not the compound (Al)GaAs, but it gives an idea of how different is the adsorption - desorption dynamics between these elements. A sticking coefficient can be defined for each couple atomic species - substrate, as the ratio between the number of incorporated atoms to the number of impinging atoms. For metals like Al or Ga or group IV elements like Si it is usually assumed that the sticking coefficient is one, while for group V el-

[3]This is indeed true in the case of homoepitaxy, where other driving forces like strain are not present.

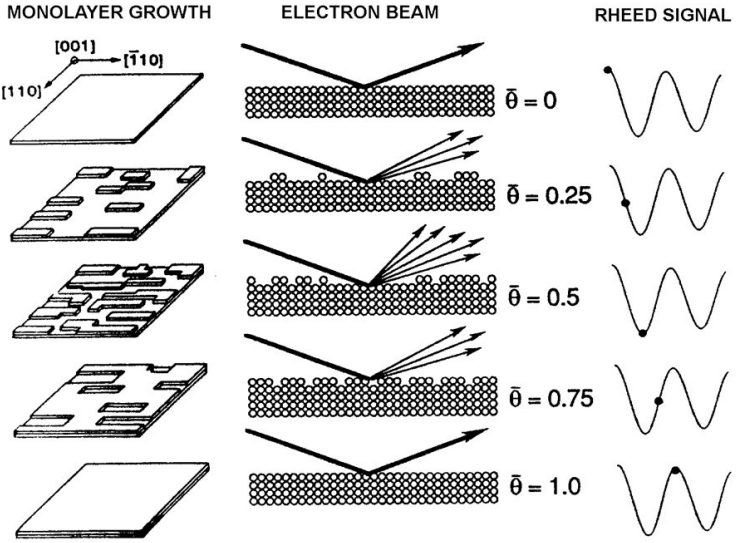

Figure 4.4: The drawing shows a graphical explanation of the RHEED intensity oscillations, in relation to monolayer coverage percentage.

ements, like As, this is not the case and the sticking coefficient is lower than one. This is the reason why arsenide crystals are grown by MBE in conditions of overpressure of As. Since at the usual growth temperatures excess As is not incorporated, only the metal components determine the growth rate of the film, in a very good approximation. The chemistry of As is more complicated, because that this element evaporates in the form of As_4 or As_2 molecules, even though the cracking stage increases the number of dimers in the beam flux. These clusters dissociate at the surface where As adatoms can diffuse to their crystallographic sites.

The growth can proceed in different ways: layer by layer, island mode, or layer plus island. Layer by layer growth (Frank - van der Merwe) is when each atomic layer is completed before another one starts to grow. This can occur when the diffusion length is high, so that adatoms can fill any empty lattice site. Island growth

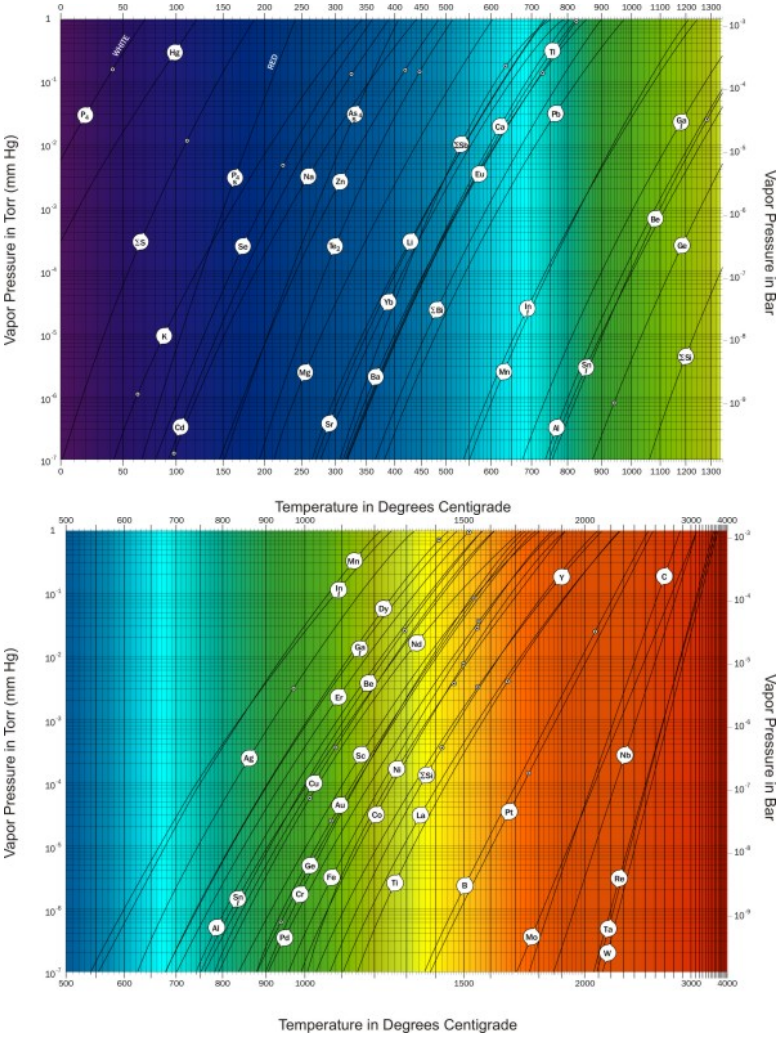

Figure 4.5: Vapor pressure charts of the elements, with the white circle indicating the melting point. From Veeco's website.

(Volmer- Weber), on the opposite, is when growth is three dimensional around the nucleation sites. This can occur in case of a

short diffusion length, so that each island behaves independently of the others. Layer plus island (Stranski - Krastanov) is somehow an intermediate way, because the island growth takes place only after a short layered growth. Island growth is strongly favored by lattice mismatch: in fact the substrate itself provides the pattern for the following crystal nucleation, so that the overgrown epilayer has to accomodate its lattice to the substrate lattice. In the case of homoepitaxy, substrate and film have the same characteristics and the film can be seen only as an extension of the underlying substrate: layer by layer growth usually occurs. In the case of heteropitaxy lattice mismatch is very frequent, so the epilayer has to deform its lattice in order to bind to the substrate. This condition is called psudomorphic growth, and usually occurs only to the very first atomic layers, depending on the lattice mismatch. When the elastic energy accumulated in the pseudomorphic layer overcomes a certain threshold, three dimensional structures are formed. The specific growth kinetics can dramatically change this near-equilibrium behavior, leading to a layered growth that is rich in crystal defects like dislocations.
Doping in AlGaAs alloys is obtained introducing an additional Si (for n-type) or Be (for p-type) flux to the main III and V element fluxes. These two elements are shallow dopants and are usually assumed to have a sticking coefficient equal to 1[4]. Since typical doping levels in solar cells can be as low as $10^{17}cm-3$, it is very difficult to calibrate the doping level relying only on the partial pressure of the dopant element as measured by the pressure gauges in the growth chamber, because this is comparable to the residual background pressure in the chamber. Post-growth characterization of doped films is usually performed to calibrate the doping levels. As an example we report in figure 4.6 the calibration of the Si and Be effusion cells in our machine: majority carrier concentration is computed after the measurement of resistivity and Hall mobility in a Van der Pauw geometry. An exponential dependence of the doping level on the effusion cell temperature is observed as expected, and data extrapolation was used to adjust the requested doping levels in the solar cells.

[4]As long as (001) growth surfaces are used.

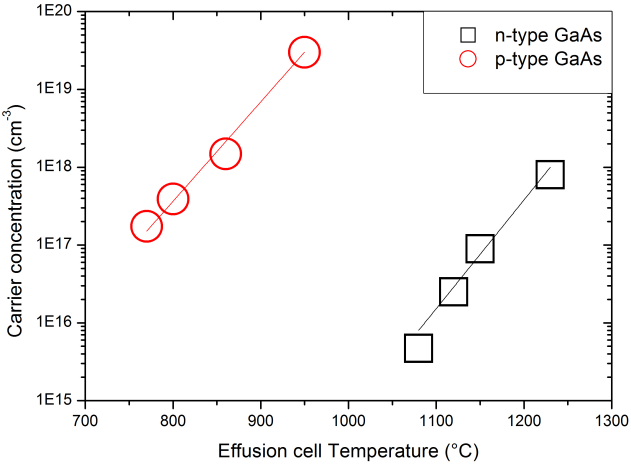

Figure 4.6: In the graph the calibration of the Si and Be GaAs-dopant effusion cells are reported.

4.2 Droplet Epitaxy

Droplet epitaxy is a technique developed in recent years to grow three dimensional structures [87] by MBE. Its strength resides in the fact that it can be applied also to lattice matched systems like GaAs and AlGaAs alloys [88]. In fact the growth method of nanostructures is radically different from the more diffused Stranski - Krastanov one. The latter is a self assembly method based on the accumulation of strain energy between substrate and epilayer and its release with the formation of three dimensional structures, that have a higher surface to volume ratio and can thus better relax strain. Drawbacks of this approach are the formation of a 2D wetting layer below the 3D nanostructures, and since the system is lattice mismatched, the high probability of defect nucleation. Highly stacked quantum dot layers have however been demonstrated with the use of strain compensation engineering [67]. Droplet epitaxy is instead based on the condensation of droplets of liquid metal

on the substrate, followed by crystallization when other elements are supplied during the growth. In the case of gallium arsenide, liquid gallium droplets form on the sample surface (in an As-free environment) that later crystallize when arsenic is supplied. This kind of growth occurs because there is a large difference between the vapor pressures of Ga and As, and so between their behaviors at the sample surface. Ga atoms stick to the surface, and in case of a Ga-rich surface reconstruction they don't bind to GaAs lattice sites, but the surface tension of liquid Ga is high enough to promote the formation of nanometric drops. The size and density

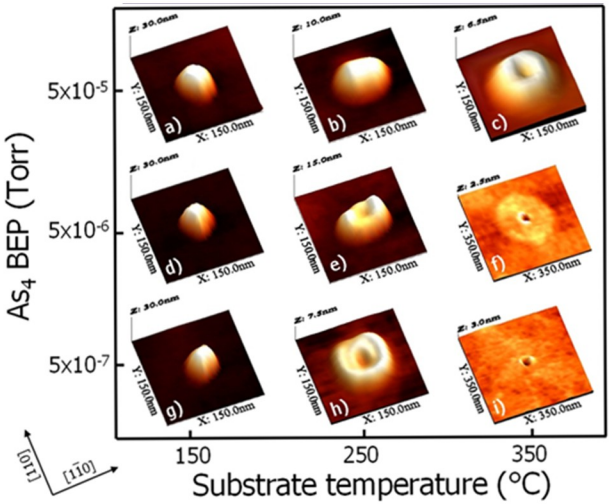

Figure 4.7: The figure shows AFM morphology of GaAs quantum nanostructures grown by droplet epitaxy as a function of the growth parameters.

of the droplets can be varied by careful tuning of the substrate temperature and the amount of Ga supplied. Densities as high as 10^{11} have been demonstrated [89]. The Ga droplet is the seed for the nanocrystal: in fact when As is supplied it reacts with the liquid Ga, diffusing into the droplet and crystallizing it. This can be seen in [88], where the RHEED pattern changes from blurry in the case of liquid droplets (liquid is a disordered phase so no

constructive interference occurs) to spotty after asrenization, that is when crystals are formed. The luminescence spectrum of these structures is in good agreement with semi-empirical single-band $k \cdot p$ calculations for the energy transitions. The optical quality is significantly improved by post growth annealing, due to the stabilization of the interfaces between the nanostructures and the barrier (see figure 4.8). In fact since droplet formation and arsenization are

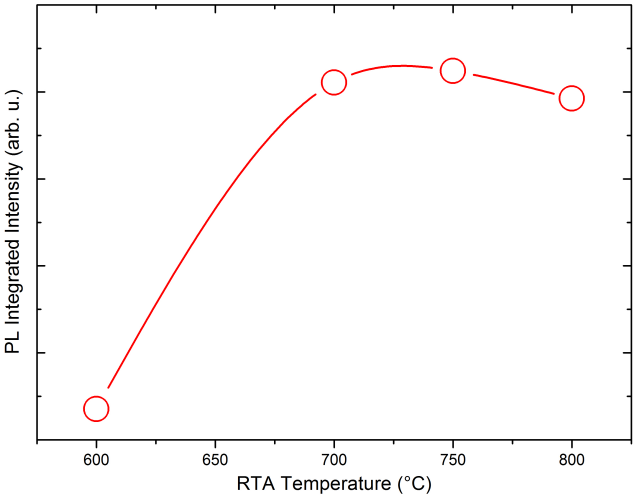

Figure 4.8: The graph reports the effect of a 4-minute RTA treatment on the PL integrated intensity of the droplet epitaxy grown quantum dots. The line is a guide for the eye.

low temperature (around 350°C) processes compared to bulk crystal growth (580°C), the barriers are also grown at low temperature to preserve the morphology, and this introduces non-radiative recombination centers, that are reduced when the interfaces stabilize with the annealing.
It has been shown [90] that it is possible to realize not only dots, but rings, multiple concentric rings, disks and combined structures like ring-dot or ring-disk [91], by changing the arsenic pressure or using pulsed supplies of arsenic. This may give an important de-

gree of freedom in further engineering of structures and their optical properties.
The big advantages of droplet epitaxy respect to the other quantum dot growth techniques from the intermediate band solar cell viewpoint lie in the fact that it is a completely strain-free technique, virtually allowing for the stack of an infinite number of quantum dot layers and thus increase the density of sub-gap absorbing states without introducing defects, that are detrimental for minority carrier device performance. The use of AlGaAs alloys as the barrier material can match the requirement of a 1.9 eV barrier material requested by intermediate band theory to achieve the ultimate energy conversion efficiency. The very high areal density of the quantum dots mitigates the need for a high number of stacked layers to achieve significant sub-gap absorption. With droplet epitaxy it is possible to avoid the nucleation of wetting layers [92], that introduce unwanted quantum-well-like energy states in the system, that can favor carrier escape mechanisms other from photon-induced transitions. The high aspect ratio that can be achieved is also very important for the design of the electronic states of the intermediate band: in fact, while usually one is interested in the fundamental (lowest-energy) confined states in the quantum dots (whose energy can be tailored by size tuning), the other (higher energy) confined states usually accumulate close to the conduction band of the barrier, favoring electron-phonon coupling that induces thermal coupling between the quasi-Fermi levels of the intermediate band and the barrier.

4.3 Fabrication process

The fabrication process used for the realization of our devices has been entirely developed from scratch at the MiB-Solar and L-Ness centres in Milano and Como.
The first step is metal contacts deposition. The electric contacts on a solar cell must be selective energy contacts, whose Fermi levels should be aligned with the hole and electron quasi-Fermi levels respectively in order to avoid drops in the output voltage or barriers to charge extraction. Several metal combinations have been explored in the past [93] that lead to very low specific contact resis-

tance. As an example Pd based metal alloys or multilayers lead to specific contact resistances lower than $10^{-6}\Omega cm^2$ on n-type GaAs layers. The more traditional AuGeNi alloy leads to comparable results once the deposition parameters are optimized. The same is true for p-type GaAs, with the most used AuZn metallization. We decided to use the alloys AuGeNi 82:12:6 and AuZn 85:15 for both GaAs and AlGaAs alloys, the former for n-type layers while the latter for p-type. This choice was motivated by our willingness to develop a process compatible to those used in industrial solar cell manufacturing. On the other hand, these alloyed contacts need a sintering step at high temperature to be effectively ohmic, so dopant or impurity diffusion can occur and one must be very careful in keeping the sintering environment very clean.
Au-based ohmic contacts to AlGaAs alloys are tunnel contacts, where a dopant element is allowed to diffuse into the crystal lattice creating a heavily doped region beneath the contact itself. In particular for n-type AlGaAs the AuGeNi contact provides Ni as a surface bagnability enhancer and Au as a lattice disrupting element that allows for the penetration of Ge, the n-type dopant. This process is activated by sintering at 430°C in Ar atmosphere. Analogously, AuZn on p-type AlGaAs alloys provide Zn as the p-type dopant; Ni can also be added but it is found not to decrease very much contact resistivity. To ensure reproducible conditions, the sample surfaces were always cleaned with nitrogen, surface oxide removed with concentrated HCl bath for 1 minute and blown dry again with nitrogen. The contacts are geometrically defined with Cu:Be shadow masks.
A thermal evaporator with current-heated Mo boats was used for the deposition of the electric contacts for all the samples fabricated for this work. For n-type contacts, Au Ni and Ge were mixed in the evaporation boat after precise measurement of their weight percentages, in the ratio 82:6:12, as reported in [93]. Thanks to the very low (around 360°C) melting temperature of the AuGeNi eutectic, it is very easy to prepare the alloy from single high purity elements directly in the evaporation boat. For p-type contacts however, no eutectic is formed and single element boats for Au and Zn were used, using a Au/Zn/Au deposition scheme, as reported in [93]. It has been found that the addition of a 2% weight Ni in the first Au layer improves mechanical resistance and adhesion of the metal film

to the surface of AlGaAs for our evaporation setup. The best results were obtained for 4nm AuNi/40nm Zn/400nm Au, measured by a piezoelectric sensor during the deposition. Both n-type and p-type contacts were sintered in Ar atmosphere at 430°C for 90 seconds.
Transfer length measurements [94] have been performed to determine the value of specific contact resistivity, using parallel bar-shaped contacts of different sizes in a lateral current flow geometry. The IV curve was measured for each pair of contacts and proved to be a linear characteristic within a 2V range, and the resistance was extracted from interpolation of the data. For all the samples the sheet resistance measured matched the expected value according to the calibration of the dopant cells performed with Hall measurements. It is well known [93] especially for n-type AlGaAs alloys

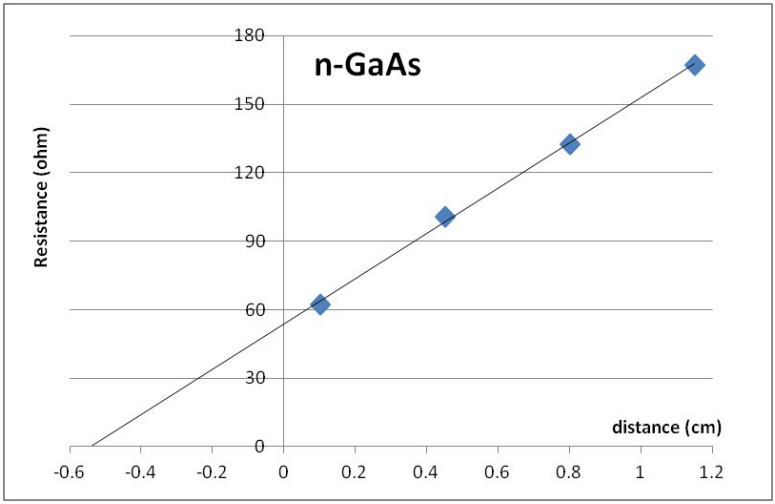

Figure 4.9: The graph shows a typical TLM measurement of n-GaAs for AuGeNi contacts. From the transfer length the specific contact resistance has been calculated.

that the doping level influences the ultimate value of contact resistance. We decided to test with films of $3 \cdot 10^{17} cm^{-3}$ doping in order to be sure to obtain the lowest possible value with our fabrication equipment and materials choice. Device contact layers have

at least a one-order-of-magnitude-higher doping level, so a much lower contact resistance is expected; moreover, a thicker (500nm) gold capping of the contacts has been used for device fabrication. For n-type GaAs we obtained a best value of $1.8 \pm 0.2\, m\Omega cm^2$ while for p-type GaAs $1.2 \pm 0.6\, m\Omega cm^2$. We measured values only 10% higher for $Al_{0.3}Ga_{0.7}As$ layers. These are clearly not record values for Au-based contacts on GaAs, but since the solar cells IV characteristics did not (apart from statistical deviations) suffer from series resistance issues[5], we decided not to invest further time in improving this fabrication step.

The device area definition was obtained via mesa wet etching. Traditional photolithography has been used for the definition of the mesas, with a single step exposure with AZ5214E photoresist used in direct imaging mode. The patterns used are squares 8x8 or 9x9 cm^2, chosen to develop a technology comparable with real-world photovoltaic devices. For GaAs and $Al_{0.3}Ga_{0.7}As$ solar cells a photomask printed on a transparent plastic pellicle was used. The precision of the process used for the manufacturing of the pellicle mask was $50\mu m$, that is good enough for large area featureless structures like mesa squares. The pellicle was $100\mu m$ thick, so little absorption in the UV range occurred. This type of photomasks has a big drawback in the severe degradation occurring after a few exposures to UV light, as can be clearly seen in figure 4.10. For this reason we decided to switch to Cr on quartz photomasks for the quantum dot devices. The edges of of the devices fabricated with the quartz photomask show a small micron-scale indentation (figure 4.11) likely due to a not-perfect-yet optimization of the photoresist softbaking and development parameters. For large area devices like in our case, these micrometric irregularities are negligible.

The sharpness of the mesa edge definition is of utmost importance in determining the device performance. This is because, as shown for example in [95], there is a strong perimeter recombination component in all III-V devices, and this is particularly evident for solar cells in the form of low shunt resistance or high ideality factor. Passivation techniques with sulfur-based chemicals or organic en-

[5]This is also because with our contact areas of $0.1\, cm^2$ the series resistance is of the order of 10 milliohms, that is negligible unless high concentration of sunlight is applied to the solar cell.

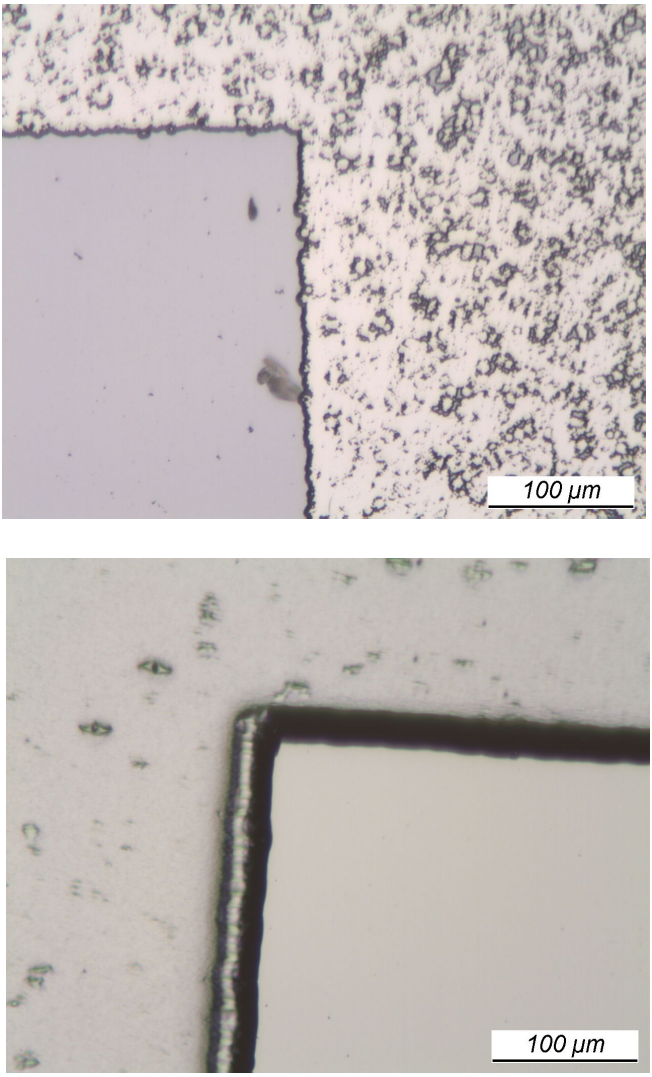

Figure 4.10: The two figures are optical microscope images of the mesa edges of $Al_{0.3}Ga_{0.7}As$ solar cells. The upper one was fabricated with a good (first use) pellicle photomask, while the lower one was fabricated with the same pellicle photomask, spoiled after several photoimpressions.

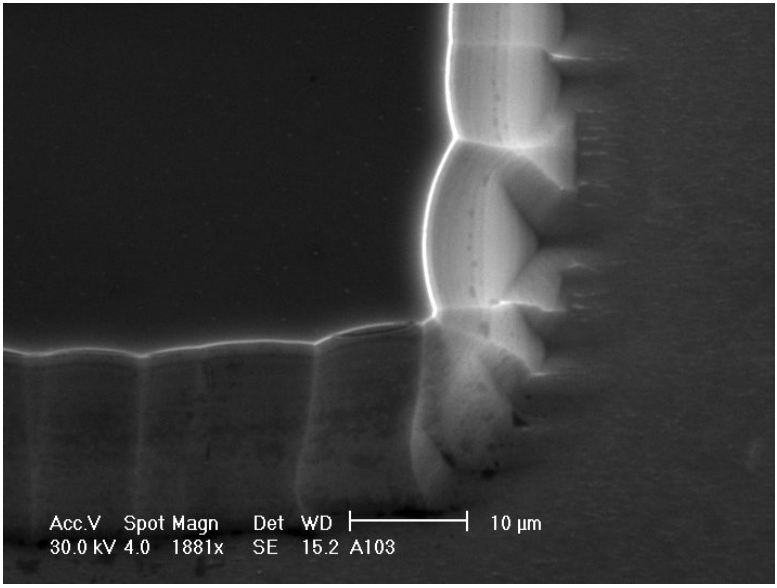

Figure 4.11: The figure shows a SEM micrograph of the mesa edge of an $Al_{0.3}Ga_{0.7}As$ solar cell. The device edge is straight, apart from micrometer scale indentations that are probably due to non perfect optimization of the photoresist development process.

capsulants is often employed in the literature, but it wasn't used in this work. The effect of a rough device edge with a longer perimeter is detrimental on device performance: it introduces an important recombination path that lowers the filling factor of the solar cells and leads to low shunt resistance and not fully rectifying diodes. Moreover pinning of the Fermi level at midgap energy defect levels leads to low open-circuit voltage outputs for the solar cells and, since the roughness and presence of electrically active defects at the edges is random, an extremely large variability in the figures of merit of the devices is observed, leading for example to a spread of 150% in the short-circuit current density[6] values. This is clearly shown in figure 4.12, where we report some IV characteristics of single junction $Al_{0.3}Ga_{0.7}As$ cells under AM1.5G spectrum: these devices were fabricated using an aged pellicle photomask. In figure 4.13 instead we report the devices fabricated with good mesa edges. The etching process used for the mesa pattern transfer on the samples has been set up for GaAs solar cells at the beginning of this work. There is a huge amount of literature (see for example [96]) on wet etching of III-V compounds. In our case the devices are grown on n-type GaAs substrates, that are used to fabricate the negative electric contact. For this reason we don't have particular constraints on the depth of the etched mesas, and also fast etchants can be used. We also don't need any selectivity between GaAs and AlGaAs alloys. For these reasons, a moderately fast $(0.5\mu m/min)$[7] $1HCl : 1H_2O_2 : 3H_2O$ solution was used. It proved to be non selective and very effective for both GaAs and AlGaAs devices. The mesa sidewalls were aligned 45° off the primary flat of the GaAs wafer (that points in the [110] direction) in order to overcome the crystallographic selectivity of the etchant solution. In fact III-planes and V-planes have different etch rates, that lead to different slopes in the etched sidewalls, and this effect is easily suppressed by tilting the mesa edges in order to show non-polar planes.

The final step is the dicing of the single solar cells out of the wafer. This was done by multiple scribing of $50\mu m$ wide lines with a 7W pulsed fiber laser (1070nm wavelength) in the trenches left between

[6] This is not imputable to variations in device area only, since these are of the order of less than 1%, as measured by optical microscopy.

[7] Calibrated with profile depth measurements.

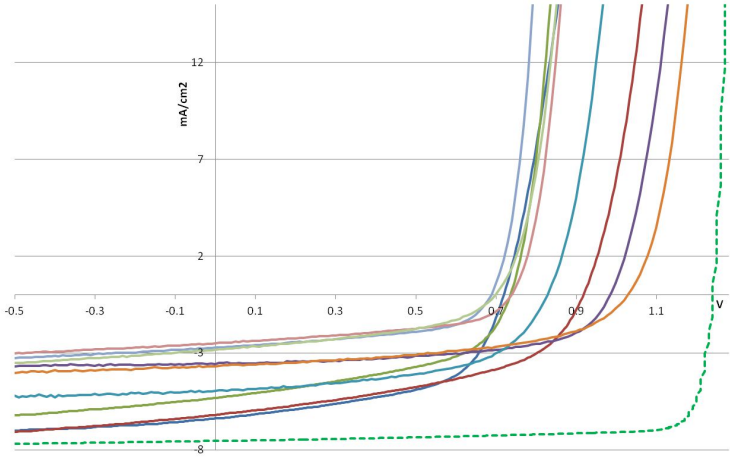

Figure 4.12: The graph collects several AM1.5G IV characteristics of various $Al_{0.3}Ga_{0.7}As$ devices fabricated with an aged pellicle photomask. The dashed curve is a numerical simulation of the same junction structure.

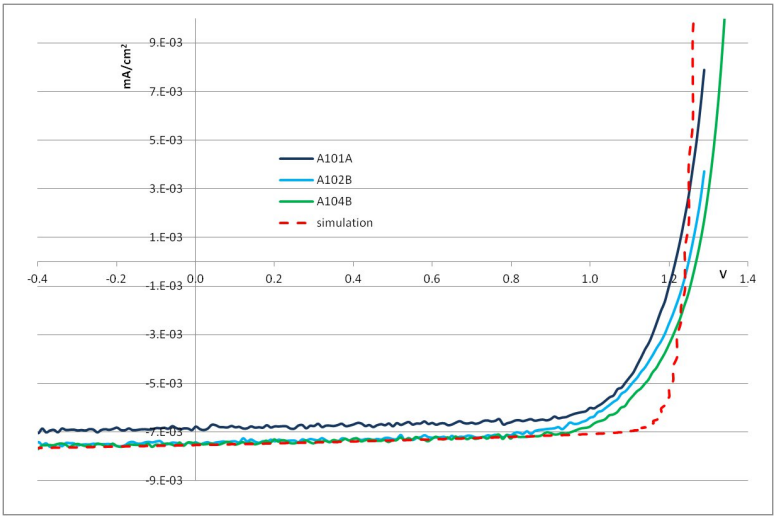

Figure 4.13: The graph reports the IV characteristics of $Al_{0.3}Ga_{0.7}As$ solar cells under AM1.5G illumination compared with a numerical simulation of the same junction structure. Devices were fabricated with a Cr-on-quartz photomask.

the devices after the etching process. The cells are easily diced with small pressure over the wafer after the scribing process.
A totally optimized process for solar cell fabrication may include two further steps: selective removal of the capping layer and deposition of an anti-reflective coating (ARC). Since all of our devices have a front window layer made of $Al_{0.85}Ga_{0.15}As$, direct air exposure would result in strong oxidation and degradation of the solar cell. To avoid this a thin layer (10 nm) of GaAs is deposited as a capping layer (see chapter 3 for the device design). Since the final goal of our project is the coupling of the solar cell quantum dot absorbing layers with metallic structures designed to enhance the IB-to-CB optical transition, no ARC has been deposited on top of the devices, neither the GaAs capping layer has been removed.

CHAPTER 5

MEASUREMENT OF SINGLE JUNCTION DEVICES

In this chapter the measurements of fabricated single junction devices are reported, illustrating the experimental setup assembled to carry out the most important spectral characterizations. Particular emphasis will be given to the feedback to design, growth and fabrication steps, here described from an experimental point of view. The measurements of single junction GaAs and $Al_{0.3}Ga_{0.7}As$ solar cells will be discussed in relation to the achieved assessment of the device making, from design to post-growth processing. These devices served to establish the processing workflow in order to minimize the variability in the fabrication of quantum dot devices.

5.1 Experimental setup

Several experimental systems have been used in this work for the optimization of the photovoltaic devices, like photoluminescence to

test the quantum dot energy structure or profilometry to calibrate the metal contact depositions or mesa etch rate. For the sake of clarity, we describe here only the most important two, that allowed the measurement of the performance of the solar cells: the solar simulator and the photoresponse (quantum efficiency) system. A variant of the latter has been set up for the low temperature and double-photon absorption measurements.

Some of the most important figures of merit of a solar cell, defined in section 1.3, can be directly measured from the current-voltage (IV) characteristic, either in the dark or under illumination. The probing station used for this purpose is based on a Keithley 2420 sourcemeter in four-wire configuration: it acts as a variable load connected in series to the device under test. The four-wire configuration is used to ensure maximum accuracy avoiding the effect of the generator's series resistance[1]. To perform IV measurements under illumination, sunlight is simulated by a Xe high pressure arc lamp and an appropriate set of filters. In fact the emission spectrum of a Xe high pressure lamp resembles a blackbody at the temperature of 5700K superimposed to intense and sharp atomic emission lines. These are attenuated and the effect of atmospheric absorption is simulated by a set of filters that allow us to simulate the AM0, AM1.5D and AM1.5G spectra. Excess IR radiation is reduced by dichroic mirrors. In this work only the AM1.5G spectrum has been used, that is the commercial reference spectrum for terrestrial unconcentrated photovoltaics.

Variations in the lamp power supply change not only the integral power of the emitted light, but also its spectral components, since the blackbody temperature changes. For this reason one must always take a lot of care to be in spectral match conditions between the simulated spectrum and the device under test [97] [98]. To this end, the lamp power was adjusted every time using a commercial GaAs or $InGaP_2$ single junction solar cell[2], according to range of

[1] The sourcemeter sets each measurement point of the IV curve working as a current generator (this allows generator series resistance to be neglected): it sets the current in a feedback loop such that the measured voltage matches the expected setpoint within a certain precision range. So the proper way to look at the IV curve is a voltage measured as a function of the injected current.

[2] The devices were kindly provided by CESI S.p.A., Milano, Italy as a courtesy by Roberta Campesato.

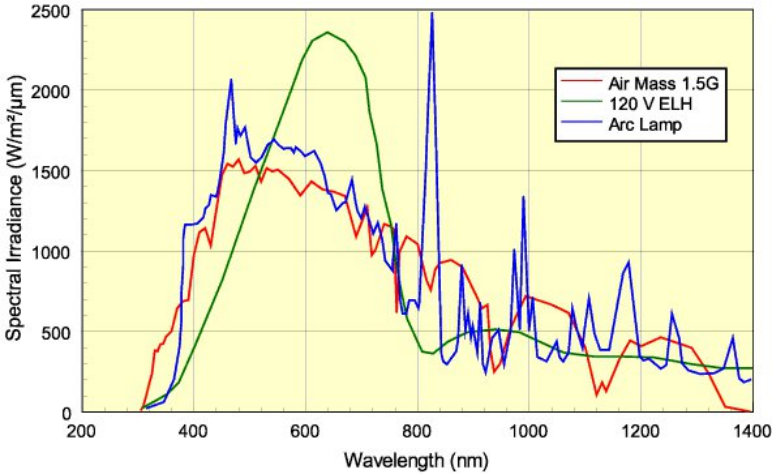

Figure 5.1: Example of the typical spectral mismatch between the reference solar spectrum and two typical sources used to simulate sunlight: a high pressure arc lamp and a ELH lamp with dichroic filter. From www.pveducation.org.

photoresponse of the devices to be measured. The spectral response of these cells was measured (see next paragraphs) and integrated in order to calculate the short-circuit current under AM1.5G spectrum.

$$J_{SC} = q \int_0^\infty SR(\lambda) \cdot AM1.5G(\lambda) d\lambda \tag{5.1}$$

The power of the Xe lamp can then be adjusted so that the measured sort-circuit current matches the calculated value. More accurate calibration requires the spectral power density of the solar simulator to be measured and spectral mismatch corrections to be applied [99]. By experience with Si and CIGS devices we assume that our calibration error is within 5%, that is comparable to the precision of our IV measurements. The lamp was tested to be stable (less than 2% variations) within one hour. Collimation and homogeneity of the simulated sunlight on a $5x5cm^2$ area is ensured by condenser optics.

The other main characterization equipment used in this work is the

spectral response measurement system. We used two different setups, whether temperature dependence of the photoresponse had to be measured or not. For room temperature measurements we used a commercial ReRa SpeQuest Quantum Efficiency system (figure 5.2). It is a single beam photoresponse measurement system with a

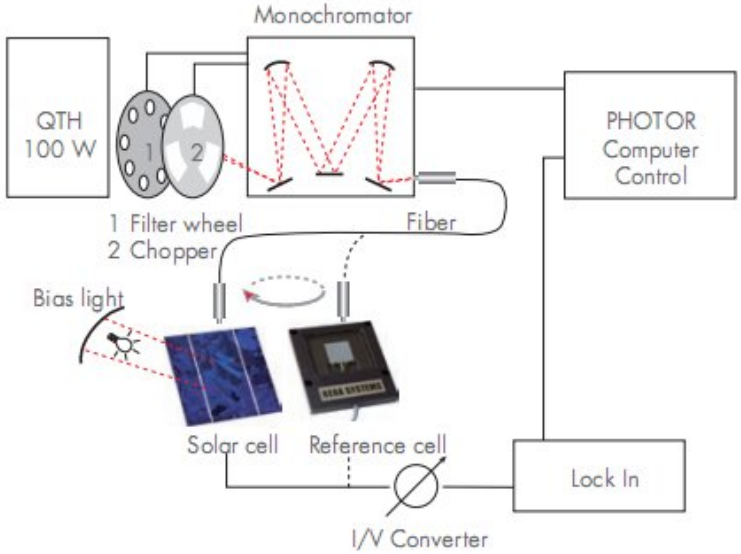

Figure 5.2: Scheme of ReRa Spequest Quantum Efficiency system. From ReRa website.

100W stabilized halogen light source illuminating a single grating Lot-Oriel Omni 300 monochromator equipped with 3 automatically interchangeable gratings to span the 300 - 1800 nm spectral range, with 4nm bandwidth. At the entrance slit of the monochromator the light is chopped in the frequency range 1 - 400Hz, while at the exit slit an automatic order sorting filter wheel is placed. The monochromatic light is focused on the device by a spherical mirror. The signal is collected by a large dynamic range Melles Griot 13AMP003 transimpedance preamplifier (that sets the device under test at zero voltage bias) and detected by a Stanford Research Systems SR830 lock-in amplifier. Light bias can be applied to the solar

cells by stabilized adjustable 20W halogen lamp and LEDs (450nm or 810nm) to simulate illumination conditions during the measurement. The continuous current is filtered by the lock-in. Bias light was only used to accurately measure the calibration cells, otherwise it was not used just to be capable of higher amplifier gains. The power of the monochromatic light was measured with a calibrated Si photodiode. Several measurements performed within 4 hours (provided the system has warmed up for 1 hour or more) proved that the power of the monochromatic light is stable within 2%. This means that fluctuations in the power supplies that can affect single beam systems are negligible in our case. All of the single junction GaAs and $Al_{0.3}Ga_{0.7}As$ cells used to develop a standard process flow for device making have been measured with this system.
To test quantum dot devices instead, a different set-up was used, that allowed for two-photon absorption measurements to be performed in the same configuration from 15K to 300K. This second set-up is conceptually no more than the replica of the former, for it consists of a 100W QTH lamp illuminating a single grating Jobin-Yvon H25 monochromator with fiber-coupled exit (bandpass used is 3nm); the monochromatic light is chopped and second order filtered, then fiber-guided and finally focused into a cryostat by an achromatic doublet. The deviced is sticked to the cold finger of the cryostat with an insulated (anodized) aluminum plaquette and thermal contact is ensured by tight screws and thermal paste. The photocurrent is collected by twisted shielded wires wrapped along the cold finger and sent to a Femto DLPCA-200 low noise transimpedance preamplifier that sets the device under test at zero voltage bias. The signal is eventually measured by a Princeton Applied Research 5207 lock-in amplifier. The signal to noise ratio of the overall system is some 10^4, compatible with the generally accepted stray light levels of single grating monochromators. The equipment is controlled by a LabView program developed by the author. A calibrated silicon solar cell was used to measure the power of the monochromatic light prior to the measurement of quantum dot devices.
Two photon absorption measurements can also be performed in the same configuration. A 10W hot filament provides broadband IR light to the sample, through a pair of focalizing mirrors. A suitable ZnSe cryostat window was installed to ensure transparency

up to $20\mu m$. The IR light is filtered with a Ge wafer, in order to have photons with energy below 0.9eV, that is below the bandgap of both $Al_{0.3}Ga_{0.7}As$ and GaAs, to excite transitions from the confined state of the quantum dots to the conduction band of the barrier.

5.2 GaAs solar cells

In the following the most important results we obtained on GaAs solar cells are reported. These devices were grown in order to assess a reliable and performing design and processing workflow that could lead to state-of-the-art photovoltaic cells. We compared our results with a commercial GaAs solar cell that we used as a benchmark, without antireflective coating. Starting from literature reports ([100], [101][3]), a single junction solar cell structure was designed using numerical simulation software (see chapter 3). Relying on the high quality of the MBE-grown GaAs, these first devices were used to test various processing schemes and develop the final process outlined in chapter 4. For the sake of simplicity here only the most relevant results are reported. The optimized sample structure is reported in figure 5.3. At first, without the possibility to fabricate mesa etched structures, the devices were cleaved out of the wafer and 200nm-thick metal contacts were evaporated. The sintering of metal contacts was performed in argon atmosphere at the temperature of 420°C for 5 minutes. This process led to the an extreme variability in the devices IV curves, as can be seen in figure 5.4. This, as seen from a more experienced point of view, is due to a wrong device processing flow. In fact series resistance was probably due to non-optimized (too thin) contacts, while shunt was due to contamination at the device edges during the sintering process. This is demonstrated by the fact that edge mechanical polishing could completely remove the shunt in the IV characteristics, as can be seen in figure 5.5. III-V devices, and GaAs solar cells in particular [102], can show a strong recombination current originating from the unpassivated edge defects. In our case, contamination

[3]These reports are about conventional fabrication technology, while nowadays epitaxial lift-off techniques and plasmonic antennas have pushed GaAs solar cells very close the their thermodynamical limit [17].

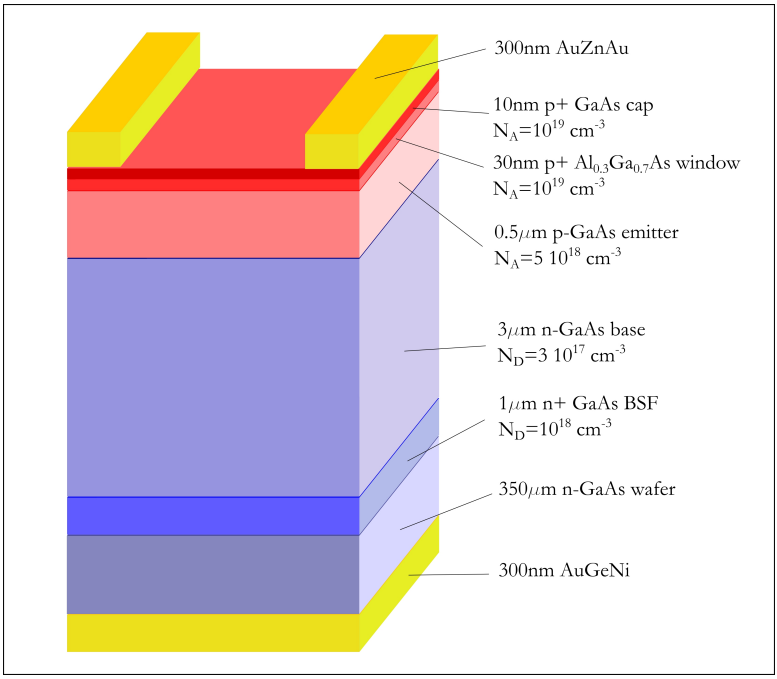

Figure 5.3: Structure of the GaAs solar cells presented in this work.

increased this effect to such an extent that the IV curves appeared heavily shunted and with large statistical deviations. The remaining variability and poor performance after polishing was likely due to defects induced by the rough mechanical polishing process itself, that may introduce microscopical cracks and indeed irregular edge shape. It is important to notice however that solar cells are usually diced with a diamond saw, that might lead to analogous edge irregularities[4]. In our case the effect was so evident because the polishing was performed by human hand, while in the industry there are machines ensuring high reproducibility. For all these reasons, we set up a photolithography system to define regular mesa structure

[4]These are mitigated in commercial devices by the fact that the perimeter recombination becomes less and less important as the size of the solar cells is increased.

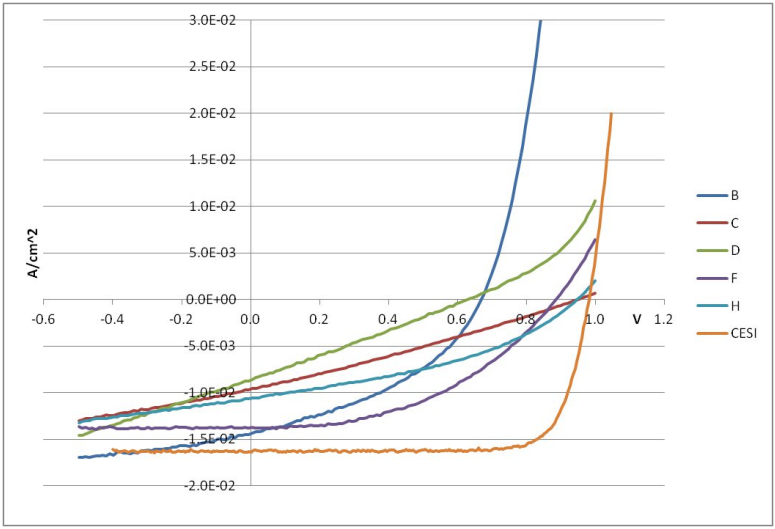

Figure 5.4: The graph reports the IV characteristics of the very first devices fabricated in our laboratories. Extreme variability and poor figures of merit are evident in the comparison with our commercial (CESI) benchmark.

and lowered the sintering time to 2 minutes to prevent excessive metal diffusion. At first, since the features to be defined were simple squares of about 1 cm per side, a printed plastic photomask was used, for its simplicity of realization and its extremely low cost, nearly one hundredth of a regular Cr on quartz photomask. It proved to be good enough for our purposes, though it degrades too fast for reliable use, as will be shown in the next section. The best result obtained for GaAs single junction solar cells matches our benchmark, as shown in figure 5.6. From the data in table 5.1 we can draw some important conclusions: first of all the short-circuit current density is slightly lower in our devices. This can be quite easily understood by looking at figure 5.7, where the external quantum efficiency of the devices is reported: our devices respond less than the benchmark in the blue end of the spectrum. This is due to the different passivation windows used, that are $InGaP_2$ for CESI's cell and $Al_{0.35}Ga_{0.65}As$ capped by GaAs for our devices.

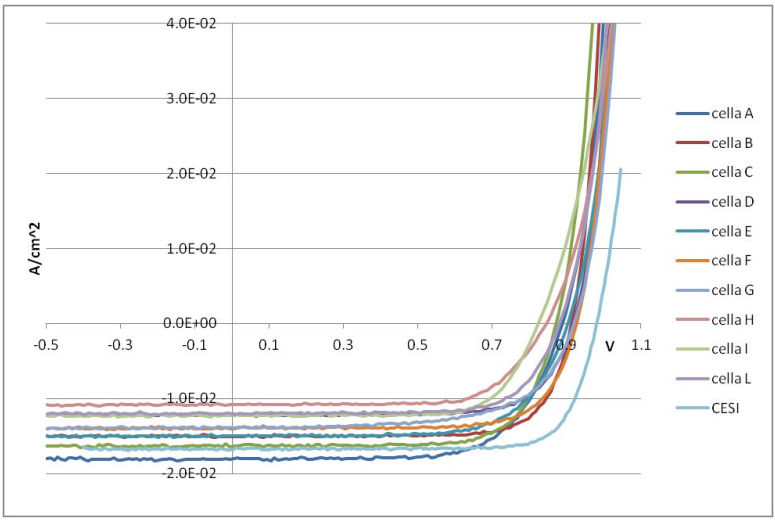

Figure 5.5: The graph reports the IV characteristics of the first GaAs solar cells after mechanical edge polishing. The shunt effect is greatly reduced, if not completely removed.

Table 5.1: The figures of merit of the devices shown in figure 5.6 are reported here.

Sample	Dark current (Acm^{-2})	J_{SC} ($mAcm^{-2}$)	V_{OC} (mV)	Fill factor	Efficiency
C6-A	$4 \cdot 10^{-8}$	17.82	937.7	77.8%	13.0%
C6-B	$3 \cdot 10^{-8}$	17.29	977.4	82.6%	14.0%
C6-C	$7 \cdot 10^{-8}$	17.52	769.2	70.7%	9.5%
CESI	$1 \cdot 10^{-5}$	18.09	926.2	77.7%	11.8%

The need to cap Al-containing layers to prevent oxidation forced us to cap the device with a thin (10 nm) layer of GaAs, that acts as a filter, especially in the blue; no capping layers are required for $InGaP_2$ windows. Our GaAs cells can reach open-circuit voltages that are better than CESI's benchmark: this is strictly correlated to the extremely low dark current density (interpolated from the IV

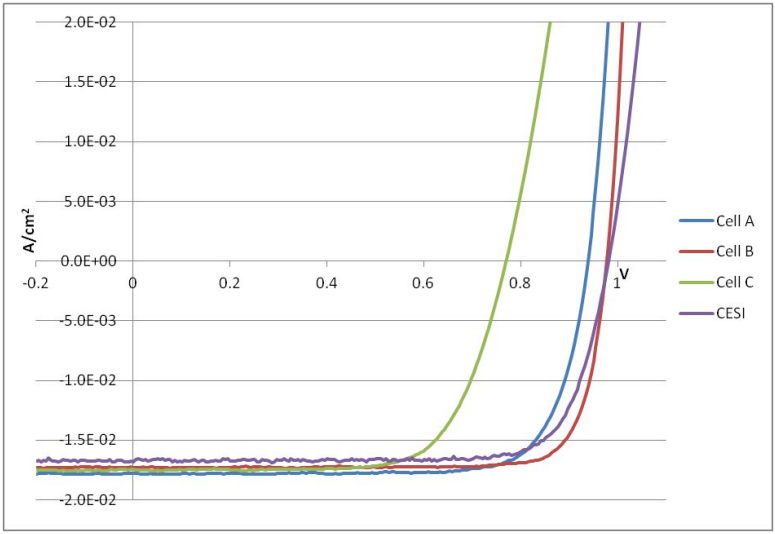

Figure 5.6: The graph shows the best two GaAs devices fabricated (cell A and B) compared with the benchmark (CESI). Cell C has a mesa defect, and it is shown here to remark once again the importance of good edge fabrication in order to have the best device performance.

curve at zero bias) in the diode equation. This so low dark current and the high fill factor of our devices can be explained by the wet etching process used for the definition of the mesas. As said before, commercial devices are usually sawed or cleaved and present edges with high electrical activity (recombination), that is reflected in the IV characteristic by higher dark current and lower fill factor.
From these data we can say that we have established a good[5] growth and fabrication process, that can ensure high quality GaAs devices, comparable to state-of-the-art ones[6]. The variability in the figures of merit of the devices is within 4%, a value that we considered acceptable for the assessment of the growth and fabrication processes according to our needs.

[5]Even though not good enough, as will be shown in the following.

[6]It's good to point out again that we refer to conventional fabrication methods. The best GaAs solar cells use plasmonic antennas and are fabricated with epitaxial lift-off techniques [103].

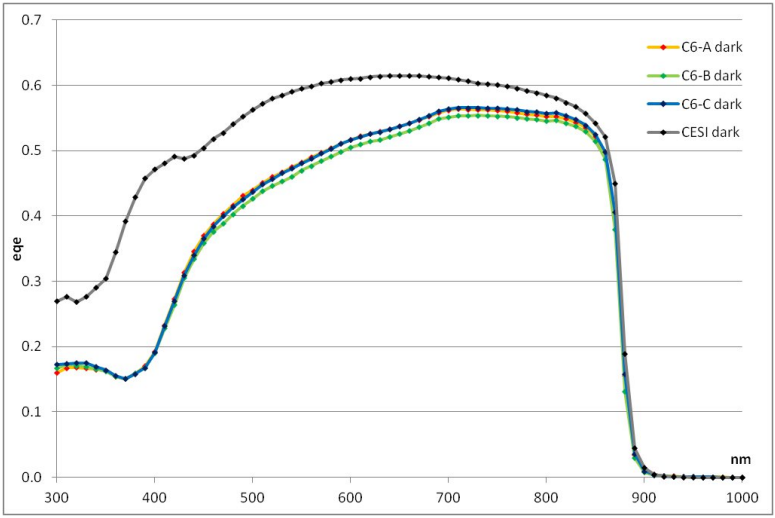

Figure 5.7: The graph shows the external quantum efficiency of the best GaAs devices, compared to CESI's benchmark. The lower response in the blue end of the spectrum is due to the GaAs capping layer. No light bias was applied in the measurements, as meant by the dark label in the legend.

5.3 $Al_{0.3}Ga_{0.7}As$ solar cells

In this paragraph, if not differently explicitly stated, we call simply AlGaAs what is actually $Al_{0.3}Ga_{0.7}As$ with 30% aluminum molar fraction.
AlGaAs proved to be a more challenging material for the growth of solar cells by MBE, with many problems related to material quality overlapping to some other fabrication problems. As a benchmark of our results we used literature data [104], [105], [106], [107]. Much fewer works have been published on AlGaAs active devices than on GaAs solar cells, and also when a high bandgap (1.8eV) material is needed (for example for passivating window layers or top junction in tandem solar cells), $InGaP_2$ is the material of reference, for it proves to be much more stable to oxidation and easier to optimize in commercial solar cell manufacturing (that are mainly based on

MOCVD technology). The structure of single junction p-n AlGaAs photovoltaic cell presented here is reported in figure 5.8.

We could recognize two different sets of problems from the large

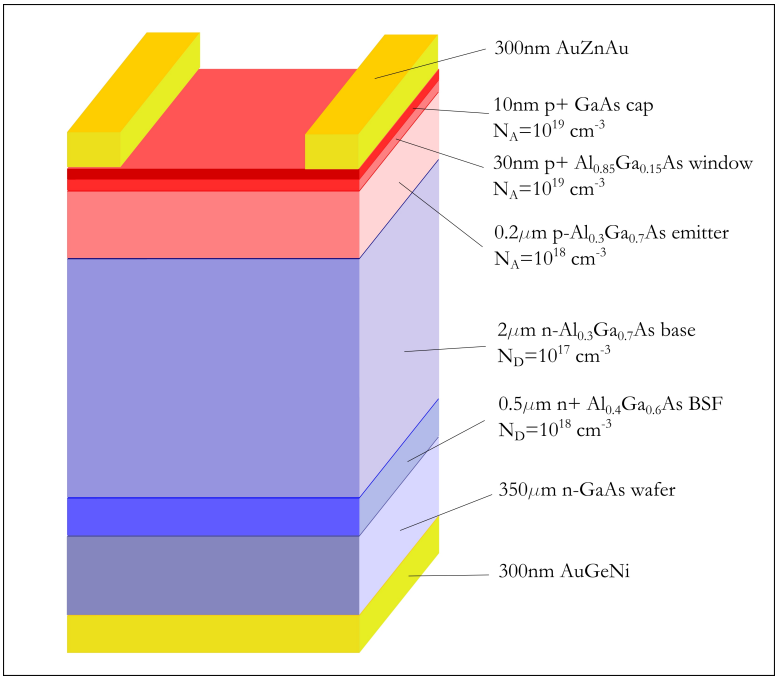

Figure 5.8: Structure of the AlGaAs p-n solar cells presented in this work.

variability (as large as 150% in the sigma of the mean value of the figures of merit) in the IV curves of the fabricated devices and from the very poor mean value of the figures of merit of the devices (figure 5.9). In particular, the average short-circuit current is 37% lower than the numerical simulations, while the open-circuit voltage is 34% lower. This has to be compared to the same situation occurred for the very first GaAs solar cells: if the sigmas from one side were as large as the AlGaAs case, on the other side the mean values were only 15% lower than the numerical simulation values. Variability issues were due to the progressive degradation of the

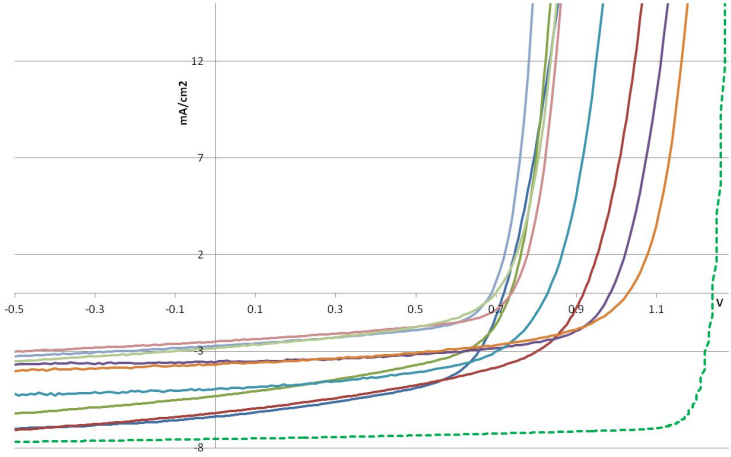

Figure 5.9: IV characteristics of our first AlGaAs solar cells, compared to the numerical simulation of the same device structure.

plastic photomask used for the mesa pattern definition, while poor average performance was due to growth temperature issues, as will be explained in the following.

AlGaAs alloys have an electron mobility that is much lower than the GaAs counterpart [80]. This is due specifically to alloy scattering, that reduces mobility; moreover, for n-type doping, other phenomena like intervalley scattering can occur at aluminum molar fractions close to the turning point from direct to indirect bandgap: this is known to be around 40% [80], not that far from our case. This turn-over has also the effect of increasing the ionization energy of shallow donors (figure 5.10), so that the effective free carrier concentration can be significantly lower than the doping, even at room temperature. We could observe the impact of this directly on the device characteristics, varying the junction structure. The p-n junction was changed into a p-i-n structure: this has the twofold effect of increasing carrier mobility and assisting the collection of photogenerated carriers with the static junction electric field. The structure of PIN cells is reported in figure 5.11 It can be seen in figure 5.14 how the spectral response decays at longer wavelengths,

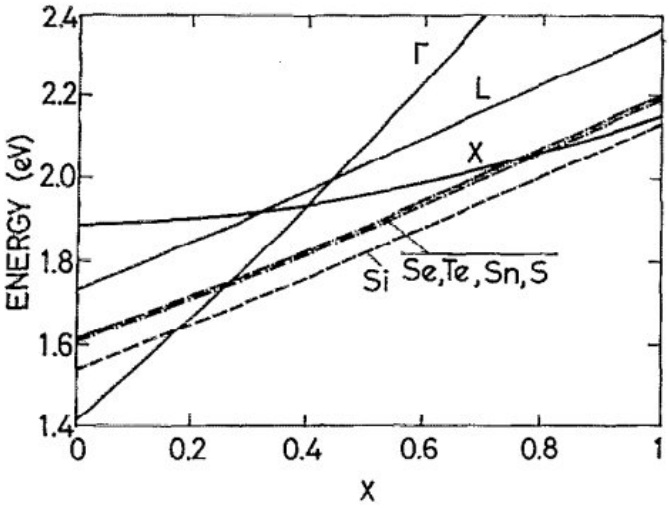

Figure 5.10: Calculated conduction band structure (zero energy is at top of the valence band) for $Al_xGa_{1-x}As$ alloys as a function of the Al molar fraction. The energy level of donors is reported. From reference [109].

that is in the n-type base of the cell, due to the longer penetration depth at those wavelengths. Since the solar cell is thick enough ($2\mu m$) to absorb all the light above gap, the decay can be understood in terms of missed collection in the case of p-n junctions. EBIC[7] measurements performed on the same devices show a greater signal decay as the electron beam is focused farther away from the junction for p-n cells than for p-i-n cells (figure 5.15). For this reason we decided to fix the design of our AlGaAs cells to P-I-N.

As can be clearly seen in figure 5.14, the new structure allows a much better collection of photogenerated carriers, so that a higher short-circuit current can be extracted from our PIN cells. From the diode equation it is clear how this should impact on the other figures of merit of the devices, especially increasing the open-circuit voltage. However, though we could see a 50% improvement in the short-circuit current, no significant variations in the open-circuit

[7]Electron beam induce current.

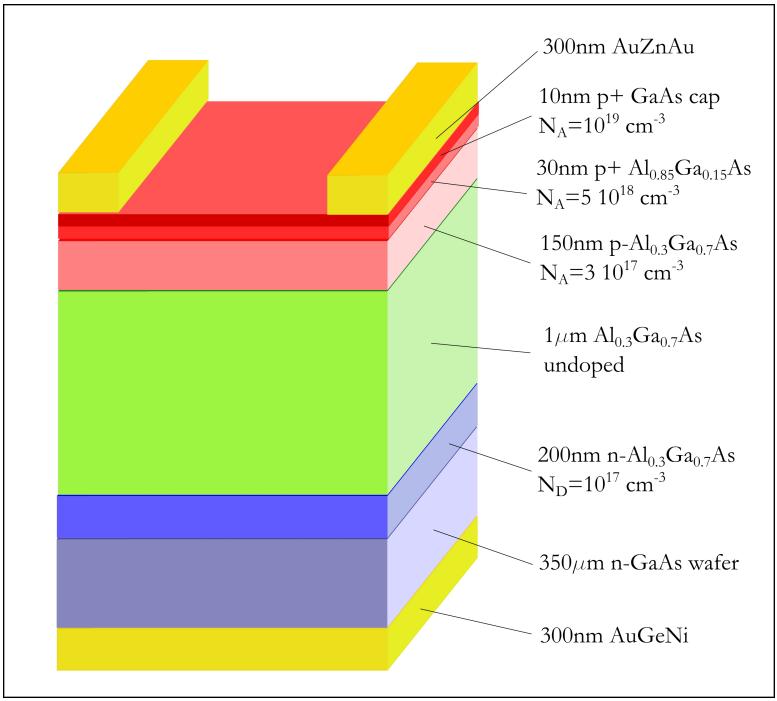

Figure 5.11: Structure of the GaAs solar cells presented in this work.

voltage were observed. A bigger advancement in our results was obtained increasing the growth temperature from 580°C (standard temperature used for the MBE growth of GaAs) to 650°C. In fact the best devices reported in the literature are grown at much higher temperatures (up to 750°C, as shown in [106]), and better results are obtained by MOVPE/MOCVD than MBE [108], in spite of the bigger amount of carbon impurity incorporation, thanks to the higher growth temperature. This is related to the surface mobility of Al adatoms, that is lower than Ga's value, and can lead to electrically active scattering or recombination centers, such as antisite defects. The combined effect of better carrier collection (achieved by changing the device structure to PIN) and increase in growth temperature proved to be effective in nearly matching the target

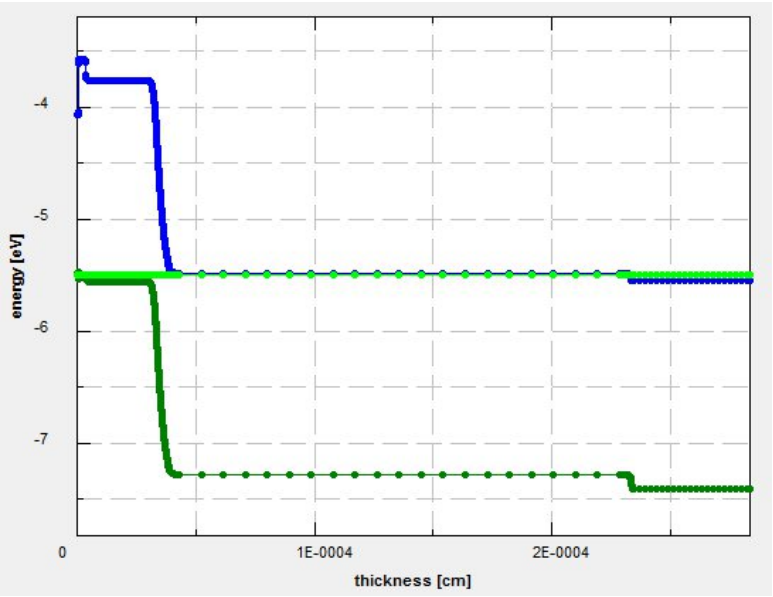

Figure 5.12: Real space band diagram of the pn AlGaAs solar cell.

values for our devices, as can be seen in figure 5.16; the differences among the devices were also greatly reduced because the mesa edges were aligned along the [010] and [-100] direction, in order remove the selectivity between III and V planes during the wet etching. As can be seen from the results of figure 5.16, the quality of the grown material is fundamental to obtain a good match of the figures of merit of the solar cells with the simulated values; for reproducibility and good performance the edge definition process has however proved to be fundamental. For this reason we eventually switched to a Cr-on-quartz photomask (that does not suffer from degradation, as shown in chapter 4), while keeping all the other processing steps identical. By this final tuning of our processing method we could fabricate AlGaAs solar cells that are definitely better matching with the simulated target (figure 5.17) and literature data, as shown in table 5.2.

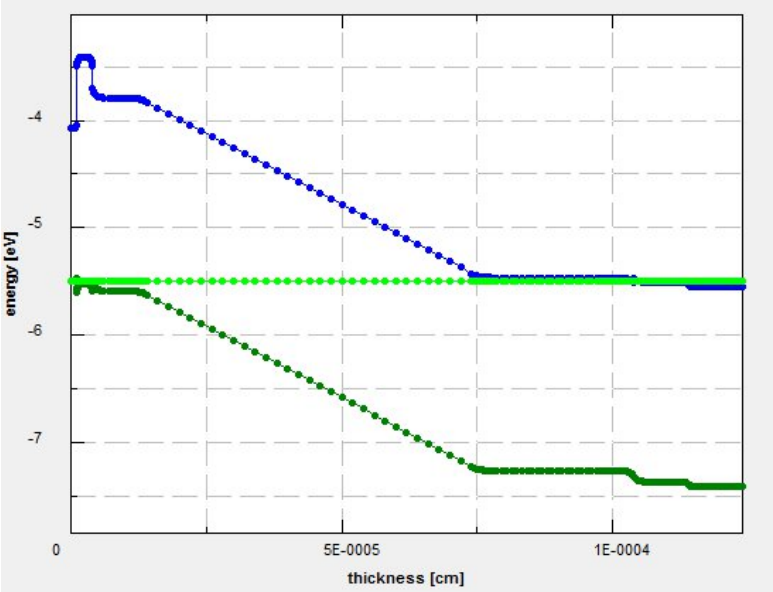

Figure 5.13: Real space band diagram of the p-i-n AlGaAs solar cell.

Table 5.2: The figures of merit of the devices shown in figure 5.17 are reported here. Data from [108] show much higher current (and efficiency) due to ARC deposition, that was not deposited in our devices.

Sample	J_{SC} $(mAcm^{-2})$	V_{OC} (mV)	Fill factor	Efficiency
A10-1A	6.91	1215	73.9%	6.1%
A10-2B	7.42	1245	69.7%	6.5%
A10-4B	7.44	1268	71.5%	6.8%
Simulation	7.48	1243	84.0%	7.2%
Literature [108]	16.3	1220	81%	16.1%

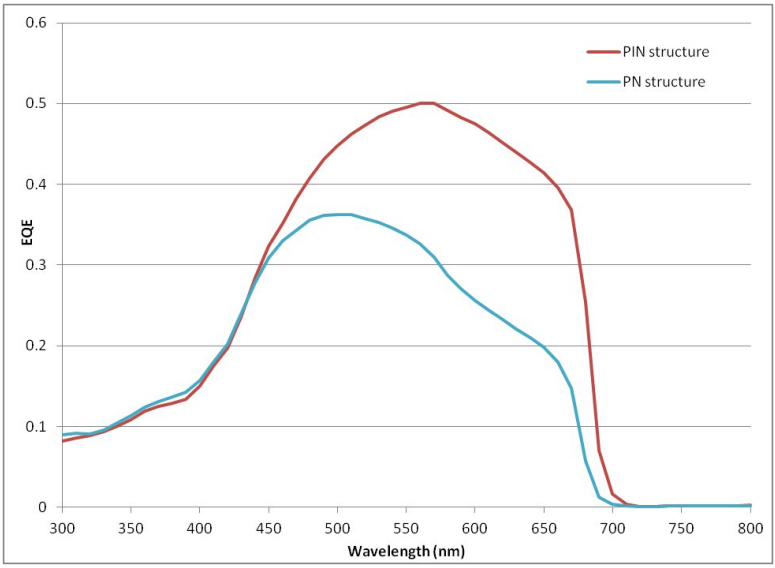

Figure 5.14: Measured external quantum efficiency graph of the PN and PIN structures of AlGaAs solar cells. PN devices show a decay at above-gap long wavelengths, due to missed charge collection for the presence of scattering centers. The light shift in the bandgap energy between the two devices is due to a small (1%) fluctuation in the Al molar fraction during the growth.

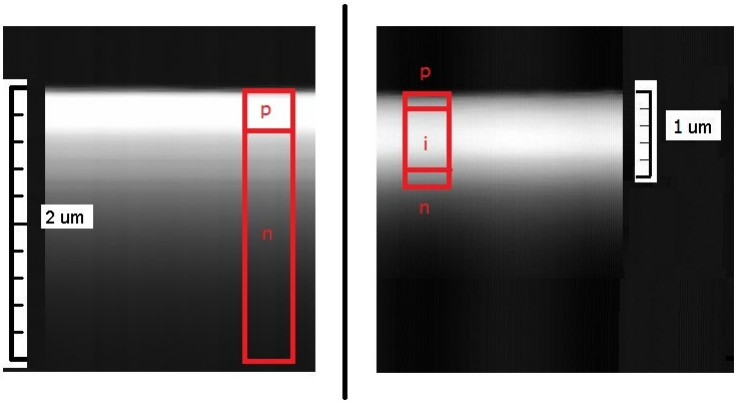

Figure 5.15: SEM-EBIC cross section of PN (left, $2\mu m$ thick device) and PIN (right, $1\mu m$ thick device) AlGaAs solar cells. The white regions indicate good charge collection. Quantitative analyses are very complex in this case, where the generation volume is comparable to the junction thickness, and hence they have not been performed. From a qualitative point of view, it is still possible to see that the signal strongly decays in the PN cell as we go far away from the junction, while in the PIN device it is nearly constant throughout all the active region.

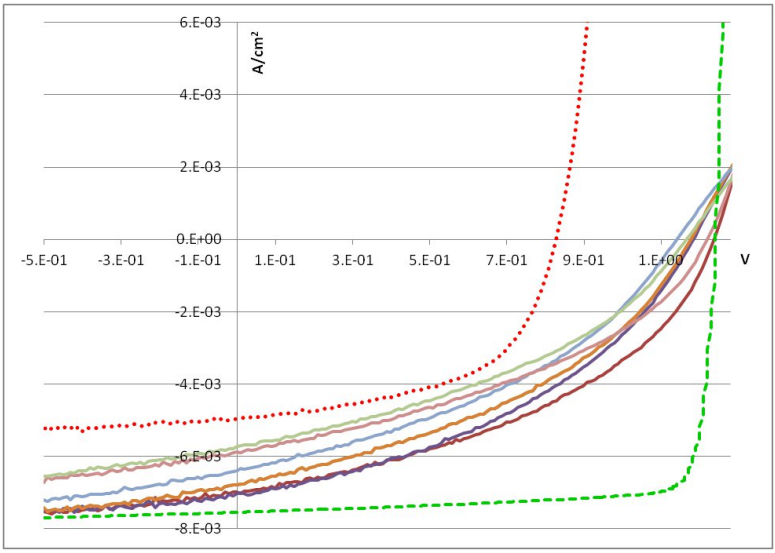

Figure 5.16: IV characteristics of AlGaAs solar cells grown at 650°C, compared to the numerical simulation of the same device structure (green dashed curve). The red dotted curve is the averaged IV curve of the devices reported in figure 5.9.

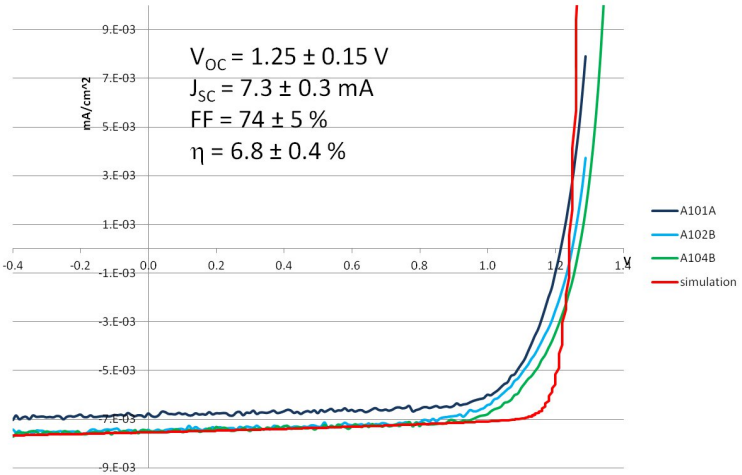

Figure 5.17: IV characteristics of the best AlGaAs solar cells compared to the numerical simulation of the same device structure.

CHAPTER 6

INTERMEDIATE BAND DEVICES

In this chapter the results obtained on quantum dot photovoltaic cells are presented. After assessing the device growth and the post-growth processing steps, we introduced GaAs quantum dots in a P-I-N $Al_{0.3}Ga_{0.7}As$ solar cell, designed according to the high density and high aspect ratio requirements outlined in chapter 4. The key intermediate band working principle of two-photon absorption is demonstrated and discussed in detail, in order to give a better understanding of the phenomenon already observed for InAs quantum dots in GaAs solar cells [22].

6.1 Device performance

Quantum dot photovoltaic cells were grown by droplet epitaxy, with the structure reported in table 6.1. Since the quantum dots are embedded in the intrinsic (electrostatic field) region of the solar cells, 200nm-thick spacers have been introduced in order to avoid tunneling between the QD layers. The Ga droplets were formed and arsenized at 150°C, and QDs were capped by $Al_{0.3}Ga_{0.7}As$ grown

Table 6.1: Structure of quantum dot solar cell sample QD1. The quantum dot + spacer layers are repeated identically 3 times.

Layer composition	Thickness (μm)	Doping level (cm^{-3})	
n+ GaAs substrate	350	$> 2 \cdot 10^{18}$	
n+ GaAs buffer	0.1	$2 \cdot 10^{18}$	
n-$Al_{0.3}Ga_{0.7}As$	0.2	$1 \cdot 10^{17}$	
$Al_{0.3}Ga_{0.7}As$	0.2	undoped	
QD layer	3ML Ga 150°C + 5nm $Al_{0.3}Ga_{0.7}As$	(Si) $5 \cdot 10^{10}$	x3
$Al_{0.3}Ga_{0.7}As$ spacer	0.2	undoped	x3
$Al_{0.3}Ga_{0.7}As$	0.2	undoped	
p-$Al_{0.3}Ga_{0.7}As$	0.2	$3 \cdot 10^{17}$	
p-$Al_{0.85}Ga_{0.15}As$	0.03	$5 \cdot 10^{18}$	
p-GaAs	0.01	$1 \cdot 10^{19}$	

by migration enhanced epitaxy at 350°C. For all the other layers we used 650°C growth temperature. The sample was annealed at 800°C for 4 minutes before the deposition of the electric contacts, to enhance the dot/barrier interface quality. Figure 6.1 is an AFM image of an uncapped QD sample with the same characteristics of the QD1 device. The areal density of the QDs is about $6 \cdot 10^{10} cm^2$, while the average height and base radius are 6 ± 1nm and 18 ± 3nm respectively. The effect of post-growth annealing on device performance is shown in figure 6.2, as an enhancement of the photoresponse, both at high energy and at sub-gap energy (figure 6.3). In fact a clear extension of the spectral response at low energies appears after annealing, because, as shown previously for PL (see chapter 4), the reduction of interface defects reduces non-radiative recombination processes. The IV characteristic under AM1.5G spectrum of the QD1 solar cell at room temperature is reported in figure 6.5. This device has poor performance, probably induced by the presence of a large number of electrically active traps in the $Al_{0.3}Ga_{0.7}As$ barrier, due to the low temperature growth steps required by the droplet epitaxy. This effect has been shown in the previous chapter for $Al_{0.3}Ga_{0.7}As$ single junction solar cells. If on one side the reduction in the V_{OC} is consistent with what has been observed by other researchers (see for example [23]), we also

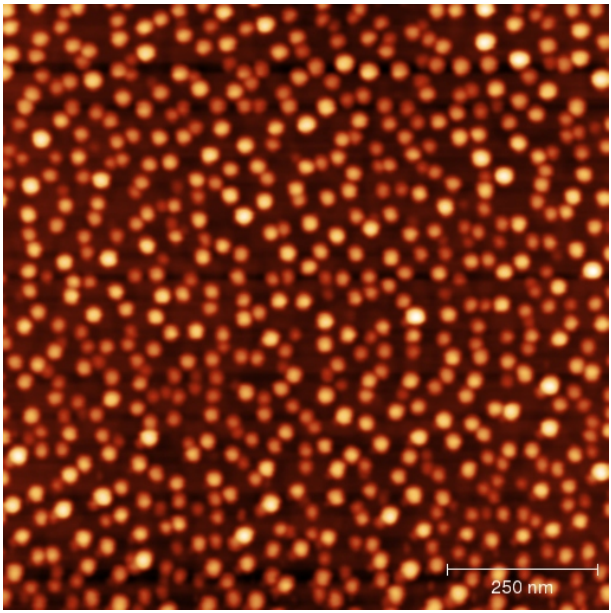

Figure 6.1: AFM image of an uncapped quantum dot sample grown with the same parameters used for QD1 solar cell sample.

observe a significant reduction in J_{SC} in comparison with the AlGaAs reference sample. It must be noted however that we are now comparing the QD devices with a reference grown at high temperature, 650°C, without the low temperature steps performed in the droplet epitaxy growth. It is reasonable then that a lower current is extracted since the low temperature layers are much richer in traps[1].
To reduce this effect, a different sample was grown with one single layer of quantum dots (details in table 6.2). The areal density of the QDs is about $3.5 \cdot 10^{10} cm^2$, while the average height and base

[1] A proper comparison must be done with an AlGaAs reference cell grown performing the same steps of temperature variation needed for the droplet epitaxy. Impurity gettering or antisite defects can occur in low temperature growth conditions, that lead to less performing devices. This sample is being prepared at the time of the submission of this thesis, so the results will be published elsewhere.

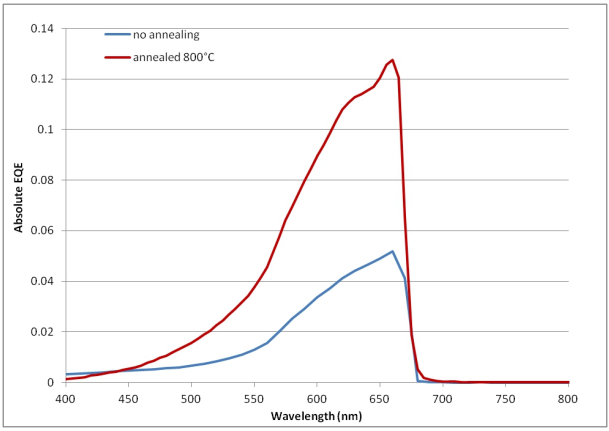

Figure 6.2: Absolute external quantum efficiency measurement for the QD1 solar cell sample, before and after RTA at 800°C.

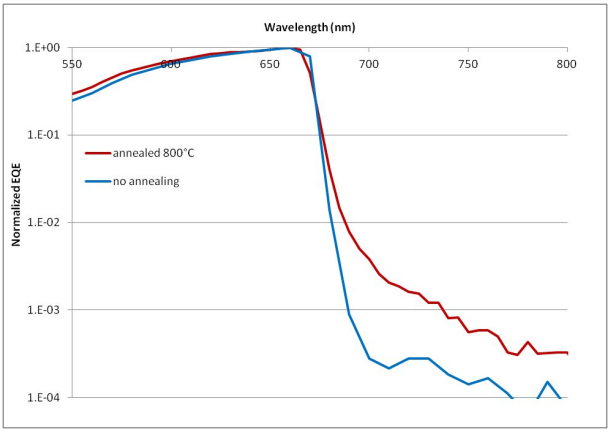

Figure 6.3: Relative external quantum efficiency measurement for the QD1 solar cell sample, before and after RTA at 800°C. The sub-gap photoresponse increases due to the annealing process.

radius are 4nm and 20nm respectively. The dots have lower aspect ratio in this sample (QD2) because the nucleation temperature for the Ga droplets was 180°C. In figure 6.4 the photoresponse mea-

Table 6.2: Structure of the quantum dot solar cell, sample QD2. Measurements are discussed in the following. Sample QD2 was annealed after growth at 750°C for 4 minutes.

Layer composition	Thickness (μm)	Doping level (cm^{-3})
n+ GaAs substrate	350	$> 2 \cdot 10^{18}$
n+ GaAs buffer	0.1	$2 \cdot 10^{18}$
n-$Al_{0.3}Ga_{0.7}As$	0.2	$1 \cdot 10^{17}$
$Al_{0.3}Ga_{0.7}As$	0.1	undoped
QD layer	3ML Ga 180°C + 5nm $Al_{0.3}Ga_{0.7}As$	(Si) $1.5 \cdot 10^{11}$
$Al_{0.3}Ga_{0.7}As$	0.8	undoped
p-$Al_{0.3}Ga_{0.7}As$	0.2	$3 \cdot 10^{17}$
p-$Al_{0.85}Ga_{0.15}As$	0.03	$5 \cdot 10^{18}$
p-GaAs	0.01	$1 \cdot 10^{19}$

surements of the two different quantum dot devices are compared with a reference cell without quantum dots. The photogeneration capability of the QD devices has been clearly extended to lower energies. The reduction to one single layer grown at low temperature improves the quality of the devices, as can be seen from the IV characteristics in figure 6.5.
The sub-gap photoresponse at room temperature can be observed because electrons in the QD confined levels can escape to the CB and be collected thanks to thermal energy. At 15K the thermal escape is no longer possible, and in fact no sub-gap photocurrent is detected (figure 6.6). The great reduction in sub-gap photoresponse at low temperature proves the high quality of the quantum dots, since the escape mechanism is purely thermal and not assisted by dot-barrier interface defects.

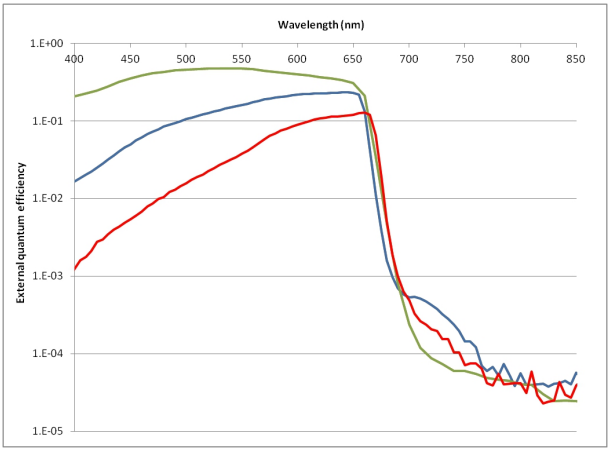

Figure 6.4: Comparison of the external quantum efficiency measurements of the QD1 (red) and QD2 (blue) samples with the reference AlGaAs sample (green), showing the effect of quantum dot sub-gap current generation.

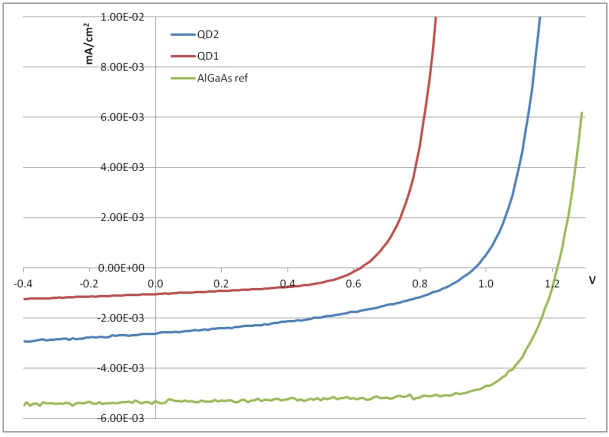

Figure 6.5: IV characteristics of the QD1, QD2 and the reference AlGaAs samples.

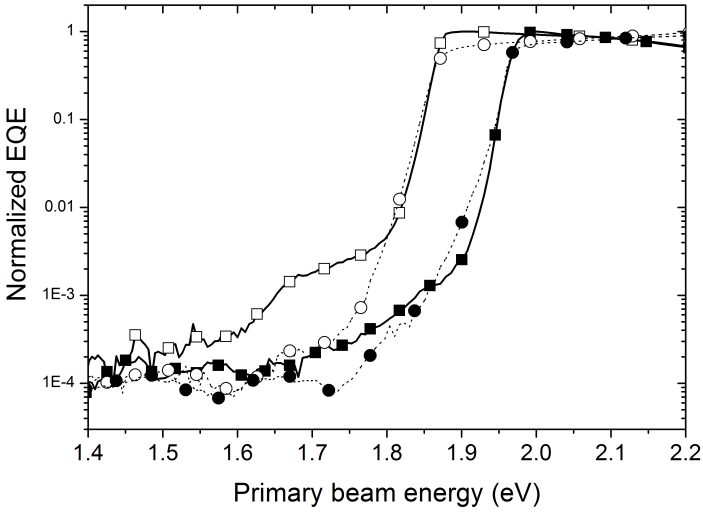

Figure 6.6: The figure shows the quenching of thermal escape at low temperature in the QD2 solar cell (squares) as compared to the control AlGaAs sample (circles). Open symbols is room temperature measurement, full symbols 15K.

6.2 Energy levels

In order to understand the energy level structure of the solar cells, we performed photoluminescence and electroluminescence measurements on the material structure and the devices. In fact when carriers are injected and recombine (radiatively) we can directly measure the differences between the electron and hole lowest energy states in the QDs[2]. Knowing the band alignment (that depends on the materials pair) and the size of the quantum dots, the confined energy levels for electrons and holes can be calculated and compared with the measured PL transitions. This can be seen in figure 6.7, where the PL spectrum is compared with $k \cdot p$ calculations for a dot of average size. The PL emission is compatible with

[2]The barrier bandgap signature may also be observed, depending on how fast is its relaxation time compared to the QDs transitions.

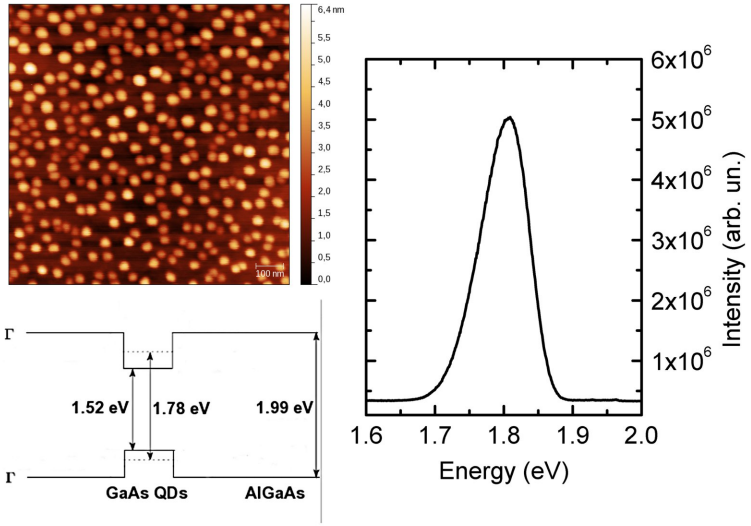

Figure 6.7: Left side: AFM image of the uncapped quantum dots of the same type of those grown in the QD2 sample. At the bottom the fundamental energy levels calculated by semi-empirical single band $k \cdot p$ method from the average dot shape. Right side: 15K PL spectrum of the QD2 sample.

the observed sub-gap absorption (shown in figure 6.6), considering the temperature-induced red shift of the $Al_{0.3}Ga_{0.7}As$ bandgap, about 0.1 eV, between 15K and room temperature. In fact from the photoresponse cut-on shown in figure 6.6 we can identify the main VB-CB bandgap to be 1.85eV at room temperature (1.95eV at 15K). The sub-gap photoresponse cut-on is however around 1.6eV (at 15K we assume a 0.1 blue shift, like for the main bandgap): this means that the IB lower band edge is about 1.6eV (1.7eV at 15K) higher than the VB edge. By PL we can estimate the width of the IB, from the width of the emission, to be about 0.1eV. Thus we can think of the VB-IB bandgap as being 1.7 ± 0.1eV (1.8 ± 0.1eV at 15K), and eventually the IB-CB bandgap being 0.15 ± 0.1eV (figure 6.8). We also report EL measurements on the QD2 devices (figure 6.9). The emission spectral range is the same reported in figure

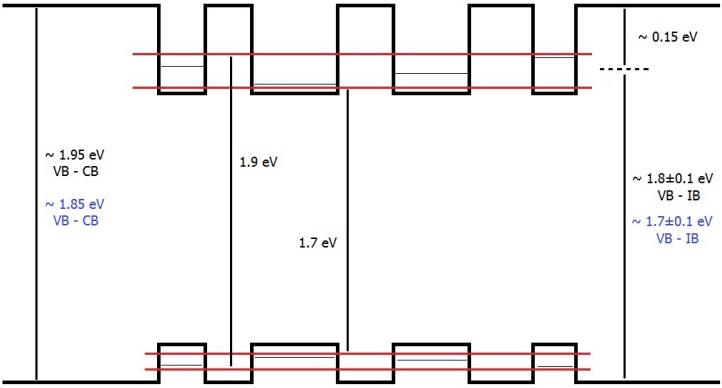

Figure 6.8: Proposed band diagram in real space for the QD layer (position axis spans in the plane of the cell, so the junction electric field bending is of no importance) of sample QD2. Black numbers refer to low temperature values, while blue numbers are proposed for room temperature, according to the photoresponse shift, as shown in figure 6.6.

6.7, confirming the dot optical activity also in the device structure [3]. The differences in the shape with the PL spectrum can be explained in terms of a difference of the injection conditions between PL and EL measurements, that can enhance emission from excited states in the quantum dots.
As proposed in [52] and [111], EL measurements can provide important information about the quasi-Fermi levels splittings in IB devices, but a more complete characterization of our samples is needed.

6.3 Two-photon absorption

Two-photon transitions constitute somehow the essence of the IB theory (see chapter 2), since the IB states can be seen as a helping step for sub-gap photons to be absorbed and generate electron-hole

[3]That differs from the PL sample for the doping levels and the junction electric field

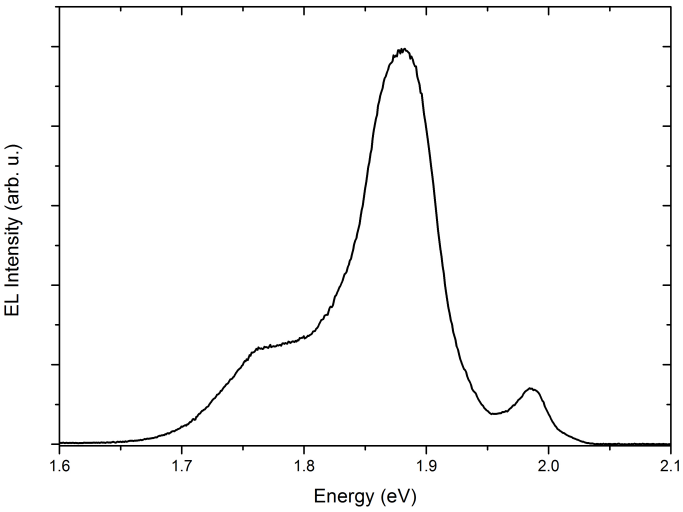

Figure 6.9: Electroluminescence measurement at 15K of the QD2 sample, input current $20mA/cm^2$ at 2.34V bias. The peak at 1.98 eV can be attributed to the CB-VB transition, while the large band between 1.7 and 1.95 eV can be attributed to IB-VB transitions, after the assumption that the barrier's VB edge merges with the confined hole levels.

pairs in the conduction (CB) and valence bands (VB). In particular, for proper IB functioning, two sub-gap photons are required to generate one electron-hole pair. The first photon triggers the transition from VB to IB, while the second photon promotes the excited electron from IB to CB. In ideal IB photovoltaic cells, no mechanisms other than photon absorption can induce IB-related transitions; in practice however, tunneling through quantum dot or defect states can occur, as well as phonon interaction, that is thermal escape from the IB. Nevertheless two-photon absorption can be looked for at low temperature, as thoroughly described in [22] and [68]. A monochromatic sub-gap light beam is shone on the device together with broadband IR light: the monochromatic beam (primary) pumps electrons from the VB to the IB, while the IR beam (secondary) promotes the electrons from the IB to the

CB, where they can be collected and an electric signal measured (see figure 6.10). If the primary beam provides photons with energy

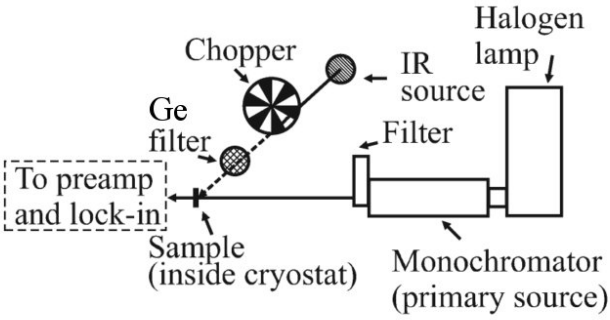

Figure 6.10: Scheme of the experimental setup used for the two-photon absorption measurement. Modified from reference [22] in accordance to the differences in the filter used. The IR source is also referred to as secondary beam in the text.

above the main bandgap (VB-CB), electrons are injected into the CB (and holes into the VB), that can be captured by the quantum dots (that constitute the IB levels); after capture, these carriers can recombine if a hole is also captured, or escape from the IB via tunneling, phonon interaction or photon interaction. Photon-assisted IB to CB transitions can be triggered by the long wavelength photons present in the secondary beam, since the IB-CB bandgap is small (the maximum value being the difference of bandgap between the barrier and dot material). As the wavelength of the primary beam is changed in order to provide sub-gap photons (with energy lower than the VB-CB bandgap), no electrons are generated in the barrier, but still they can be pumped from the VB to the IB. At this point the secondary beam photons can complete the transition to the CB: in this case a true sub-gap two-photon photocurrent can be measured. The measurement is performed as follows: the secondary beam is chopped while the primary beam is scanned in wavelength and the signal is detected by a lock-in amplifier. The secondary beam cannot generate photocurrent since only sub-gap photons are supplied: to ensure this we filtered an infrared source

made by a hot tungsten filament with a Ge wafer $200\mu m$ thick. The secondary beam is thus constituted by the broadband tail of the blackbody emission of the filament cut at wavelengths above $1.5\mu m$ (0.83 eV).[4] This value is much lower than the bandgap of both $Al_{0.3}Ga_{0.7}As$ and GaAs, so we are sure that only IB to CB transitions can be excited by the secondary beam. Any signal detected in this configuration must come from IB-CB transitions, and if it occurs only when the primary beam is also supplied, this is evidence of a two-photon absorption process. In our case, the power of the secondary beam is about 0.5mW, while the primary of the monochromatic beam is some microwatts, depending on the wavelength. Such low excitation powers, combined with the small (if compared to the bulk) density of absorbing states, leads to a very low (below nanoamp scale) photocurrent signal. For this reason, we took particular care in using low-noise low-signal measurement tricks, such as twisted shielded wires for signal collection and low-noise preamplification before lock-in detection. The use of a transimpedance preamplifier also ensures that the solar cell is biased at zero voltage, that is in the so-called photovoltaic mode. Experimental setup details can be found in chapter 5.1.
We performed the two-photon photocurrent measurements on the samples QD1 and QD2, and results are reported in figures 6.11 and 6.12. The measurements were performed at 15K in order to minimize the thermal coupling between the IB and the CB, that would lower the population of the available electrons in the IB to be promoted to the CB by the secondary beam. We could detect a two-photon signal that is distinctly higher than the noise level, with a spectral shape extending also below the bandgap of the $Al_{0.3}Ga_{0.7}As$ barrier, and only for the quantum dot samples. No such signal is present when the IB (the quantum dots) is not present, like in a reference $Al_{0.3}Ga_{0.7}As$ solar cell (figure 6.14). This is clear evidence that our quantum dot solar cells show an intermediate band behavior. The extension of the sub-gap signal for QD1 and QD2 is different, and this is in agreement with the different size of the quantum dots. For sample QD2 the signal is weaker than what is for sample QD1 at sub-gap wavelengths, but we can

[4] This value comes from the direct bandgap of Ge; the indirect (fundamental) bandgap is 0.67eV, so some light in the 0.67 - 0.83 eV may still pass through the filter.

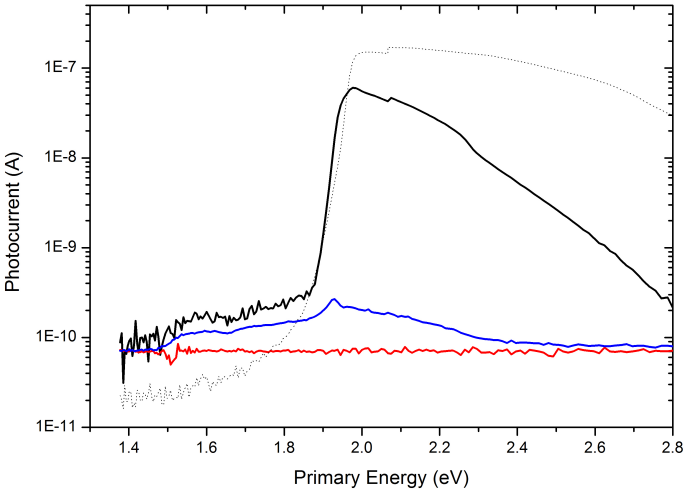

Figure 6.11: The graph reports the two-photon photocurrent measurement for the QD1 sample. Black curves are the single-photon photocurrents (dashed is the AlGaAs control sample, continuous QD1 sample), blue curve is the two-photon signal, red curve is the noise level. The small kink at 2.06 eV is due to the insertion of a long-pass filter.

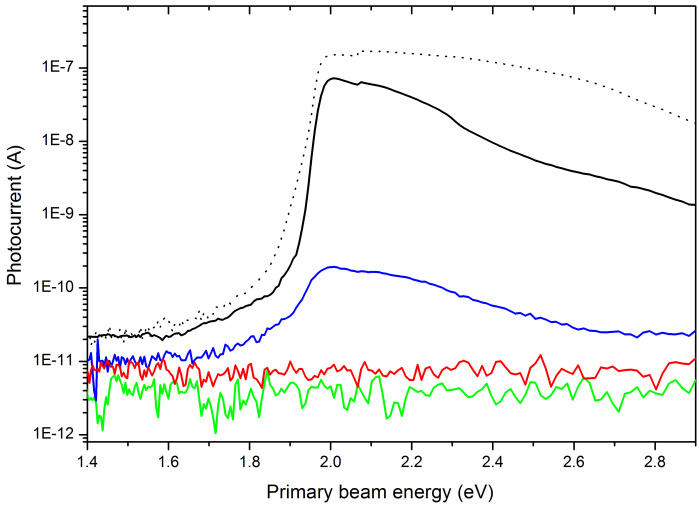

Figure 6.12: The figure shows the photocurrent as a function of the primary beam wavelength, whose bandpass is 3nm. The dashed curve is the reference AlGaAs sample, while the continuous black curve is the QD2 sample, measured in single-photon (primary beam only) mode. The two-photon signal is the blue curve, clearly above the noise level of the experiment, that was measured by blanking either the primary or the secondary beam according to the configuration (single or two photon) used. The small kink at 2.06 eV is due to the insertion of a long-pass filter.

clearly see that the decay is different from that of the single photon photocurrent. In fact the ratio of the normalized two-photon signal to the normalized one-photon signal shown in figure 6.13 highlights the subgap transition ranging between 1.7 and 1.95 eV, in correspondence to the proposed IB band diagram of figure 6.8.
The temperature dependence of the intensity of the two-photon photocurrent below the bandgap of $Al_{0.3}Ga_{0.7}As$ was measured as follows: the bandgap position was extracted from the slope of the single-photon eqe measurements in function of the temperature, and the two-photon photocurrent was measured taking fixed primary beam excitation at 50 meV below the bandgap. This way

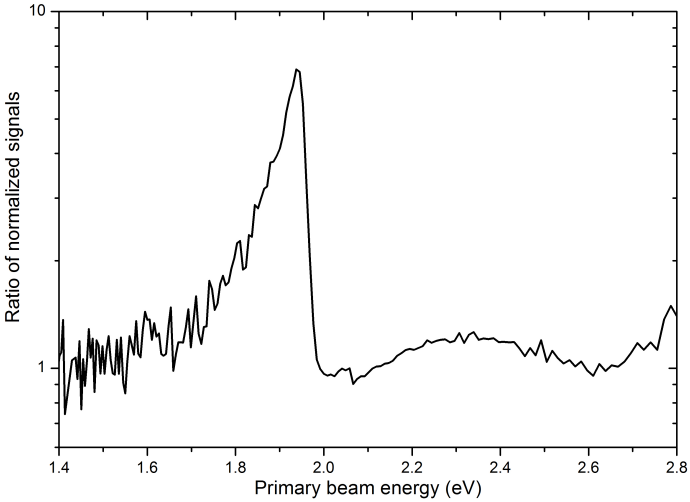

Figure 6.13: The figure reports the ratio of the normalized photocurrent signals of the QD2 sample measured in two-photon and single-photon mode. The two measurements were offset to a positive (non zero) value to avoid zero by zero ratio divergence.

is more accurate than what is reported in [68]: in the reference the authors kept a fixed primary beam excitation energy, but as the temperature is risen the intermediate band states shift to lower energies, so a varying density of IB states is probed. By changing the excitation energy accordingly to the bandgap shift instead, the same states of the IB are excited. We observe an exponential decay of the photocurrent until disappearing at noise level at 120K (figure 6.15). The data show a behavior that can be ascribed to an activation energy law, where the activation energy parameter is related to the IB-CB quasi-Fermi level split:

$$I = \frac{I_0}{1 + C \cdot exp\left(\frac{E_a}{kT}\right)} \tag{6.1}$$

This may give some other insight into the balance of the photon-induced transition (probed by the two-photon experiment) and

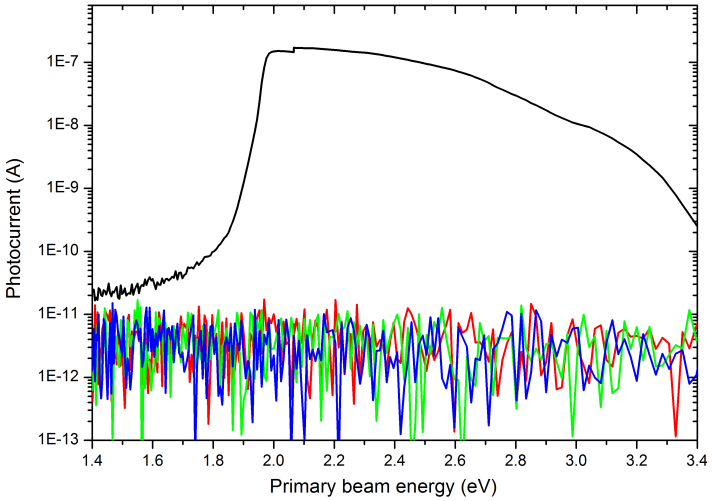

Figure 6.14: The graph shows the photocurrent measured as a function of the primary beam energy, for the AlGaAs reference sample without quantum dots. The black curve is the single photon photoresponse to the chopped primary beam, the blue curve is the two-photon photoresponse to the chopped secondary beam when the primary is on, while the green curve when the primary beam is off; the red curve is the zero level of the experiment, with the seconday beam off.

phonon-assisted transitions (probed by the decay of the sub-gap single-photon photoresponse). However, the fitting of the data in figure 6.15 is not reliable, since the spread in the size of the QDs introduces different activation energies for the system and other exponential terms must be added for good fitting. In figure 6.15 the best fit of the data is obtained with a second exponential term added to equation 6.1: the results are $E_1 = 46 \pm 5meV$ and $E_2 = 5 \pm 5meV$. In spite of the accuracy of these parameters, due to the size spread of the quantum dots, it is important to remark here that the two-photon photocurrent signal can be detected up to 120K.

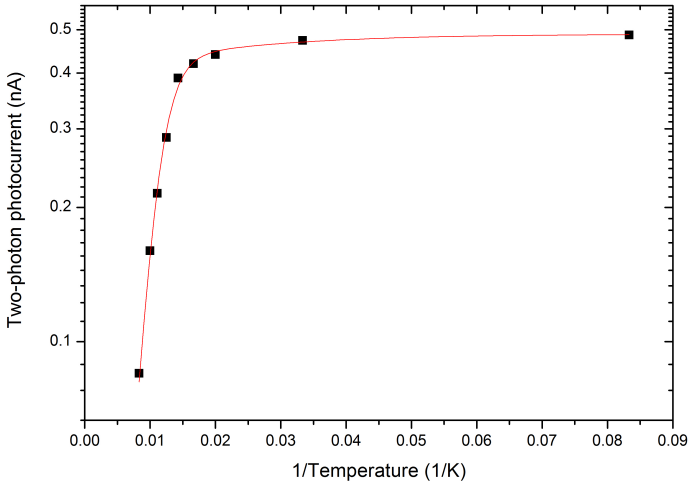

Figure 6.15: The graph reports the two-photon photocurrent temperature behavior for sample QD2. The continuous line is a fit of the data with a modified form of equation 6.1 including two exponential terms.

6.4 The role of defects

$Al_{0.3}Ga_{0.7}As$ photovoltaic cells grown at low temperature or with low temperature steps show poor performance, due to the presence of electrically active traps (see chapter 5). To investigate the presence and effect of traps, we performed the single and two-photon experiments with a 1064nm laser as the secondary beam. To avoid any possible heating of the sample the laser intensity was attenuated and the beam expanded in order to have the same secondary beam power used during the measurements with the Ge-filtered hot filament.

From figure 6.16 we can see how increasing the laser power changes the two-photon photocurrent signal. When the primary beam is blanked the signal does not disappear, but it sets to the background level indicated by the dashed horizontal lines. The increase of the background signal as increasing laser power is linear. If any DC re-

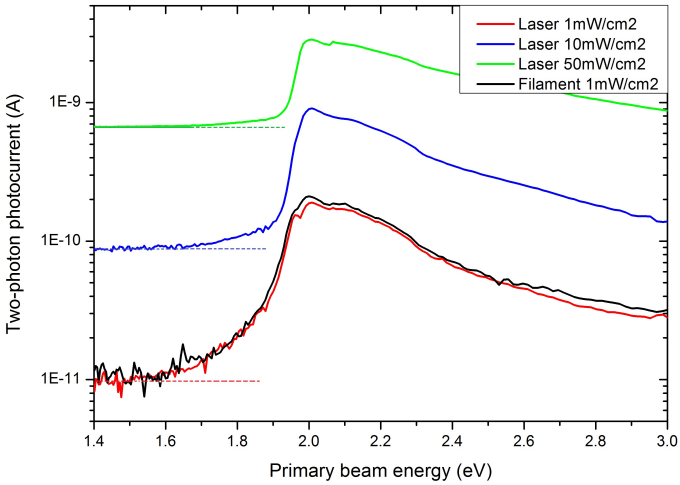

Figure 6.16: The graph reports the two-photon photocurrent of sample QD2 for different sub-gap excitation powers (device area is $0.5cm^2$). The comparison is between a hot filament filtered by a Ge wafer and a 1064 nm Nd:YAG laser. The dashed horizontal lines refer to the signal level when the primary beam is off.

sponse to the laser excitation exists in the quantum dot devices, it is so low that it was not possible to detect it with our IV characterization setup: in fact the AC signal detected by the lock-in amplifier is less than 1 nA even with $50mW/cm^2$ excitation. If we consider that the 1 sun AM1.5G excitation represents a power density of $100mW/cm^2$ and generates a short circuit current of $2.6mA/cm^2$, it is clear how the laser-induced photocurrent is negligible.

We believe that this signal comes from the traps in the $Al_{0.3}Ga_{0.7}As$ barriers, for the following reasons. First of all, the low-temperature (single-photon) spectral response decreases when the laser excites the QD samples (figure 6.17). This is consistent with the presence of traps that are activated by the laser light. Then, the low-temperature IV curve (figure 6.18) is shunted under white light illumination, and again this is consistent with the presence of a large number of traps and/or defects in the device.

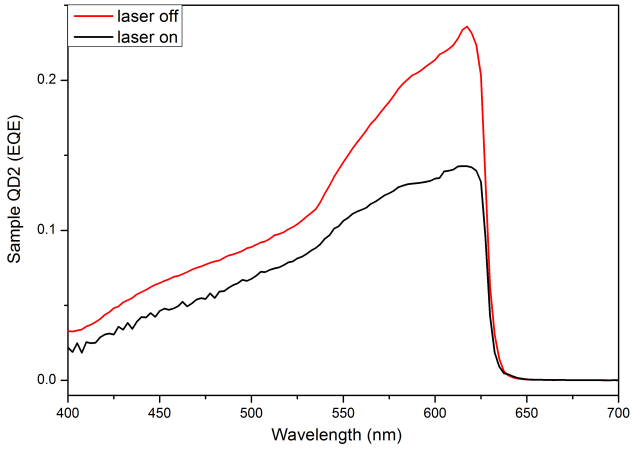

Figure 6.17: External quantum efficiency measurement at 15K of the sample QD2, with and without a 1064nm laser bias of $50mW/cm^2$.

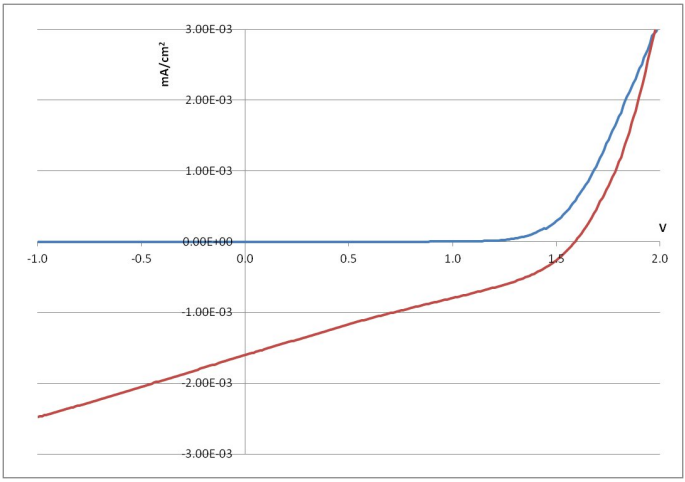

Figure 6.18: IV characteristic of sample QD2 at 15K under white light bias ($50mWcm^{-2}$ halogen lamp, blue curve) and in the dark (red curve).

The results of the laser-biased measurements prove that a significant number of traps or defects is present in the samples, but it is very improbable that the spectral effect of these defects changes by changing the size of the QDs, that is between sample QD1 and QD2. In fact the two samples show different two-photon photocurrent signals, in agreement with the different size of the quantum dots.

The final confirmation comes from the comparison between the

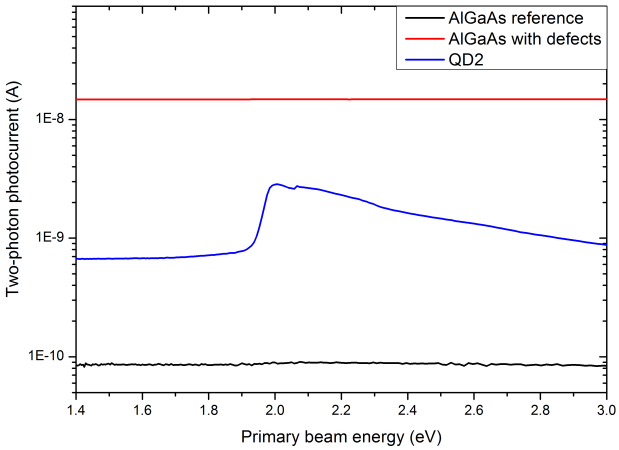

Figure 6.19: Two photon photocurrent measurement with a $50mW/cm^2$ 1064nm laser as secondary beam. The background (without primary beam) of the measurement increases as the number of traps is increased in the samples. Sample named AlGaAs defects is a single junction PIN device grown at 580°C that, as shown in chapter 5, leads to a large number of defects. The zero level (secondary beam off) of the experiment is $5 \cdot 10^{-12}A$.

two-photon photocurrent measurements with the 1064nm laser at the maximum power allowed by the experimental setup ($50mW/cm^2$), that are shown in figure 6.19. It is striking how there is absolutely no spectral dependence on the primary beam for the samples without quantum dots; the comparison between the AlGaAs reference sample and and old AlGaAs defected sample grown at lower temperature (and thus with a large amount of traps, as discussed in

chapter 5), highlights the role of traps in increasing the background level of the two-photon signal. Since the spectral dependence is present only for the QD sample, we can attribute with certainty that signal to IB-related transitions.

We have demonstrated that the key IB solar cell working principle, two-photon absorption, is fulfilled in GaAs/$Al_{0.3}Ga_{0.7}As$ quantum dots photovoltaic cells grown by droplet epitaxy. Both single and two-photon photoresponse experiments agree with PL data on the energy levels of the quantum dot system. Due to the relatively low growth temperature employed for the quantum dot layers, the $Al_{0.3}Ga_{0.7}As$ host device is rich of traps (like for example III to V antisites) that badly affect the overall device performance and are optically active at subgap wavelengths. However there is no two-photon photoresponse from these defects, as confirmed by the independence of the primary beam excitation, while this is found only in quantum dot samples. This confirms that the IB behavior observed is a property of the quantum dots themselves, and can eventually be engineered in order to tune and increase their absorption coefficient and obtain a separate quasi-Fermi level for the IB.

CHAPTER 7

CONCLUSIONS

The aim of this work was to develop the technology to grow and characterize quantum dot based photovoltaic cells at the MiB-Solar and L-NESS research centres, and demonstrate the feasibility of intermediate band solar cells with quantum dot/barrier lattice matched materials grown by droplet epitaxy.
A great part of the work has been devoted to the establishment of the design, growth and fabrication steps necessary to realize the (Al)GaAs solar cells that would host the quantum dots.
GaAs quantum dots grown by droplet epitaxy have been shown to exhibit intermediate band behavior in $Al_{0.3}Ga_{0.7}As$ photovoltaic devices. Sub bandgap photon-induced transitions have been measured that are in agreement with the electronic structure of the quantum dots. In spite of that, quantum dot devices do not show any performance improvement, more or less like what happened at the beginning of the development of InAs/GaAs IB solar cells. On the basis of our experience of $Al_{0.3}Ga_{0.7}As$ single junction devices and the optical quality of quantum dot structures, we believe that defects related to the low temperature growth steps in droplet epitaxy affect our devices, in particular the $Al_{0.3}Ga_{0.7}As$ barrier. The presence of defects in the barrier material is in agreement with the measured IV and spectral response characteristics.

Again, this is not so different from the effect of dislocations in the early InAs/GaAs IB cells, and we expect to improve in the near future. The presence of defects is strictly related to the growth temperature of the barrier material, to which we are constrained by the specific setup of our MBE machine. Other systems and different epitaxial techniques can easily achieve higher growth temperatures, so the defect issue is expected to be overcome.
We have also shown that thermal escape from the IB at low temperature is greatly reduced, proving that the quality of our nanostructured material is high.

Droplet epitaxy can be adapted to other types of barrier materials, like $In_xGa_{1-x}P$ for example, to keep the lattice match and improve the barrier quality.
Quantum dots with high aspect ratio can be grown by droplet epitaxy, approaching unity on high index surfaces, that are considered the ideal target for the IB design thanks to their optical transition characteristics. The sub-gap photocurrent generation can be enhanced by growing higher density quantum dot layers and stacking multiple layers in a single device.
Better performance is expected if light at the IB-CB transition energy is strongly concentrated, for example by surface plasmon resonances of nano metal antennas patterned on the surface of the device. This approach would also reduce the thickness required for efficient light absorption in the active material. To this end, a complete characterization of the optical IB-CB transition is needed, that is currently lacking in the literature.

BIBLIOGRAPHY

[1] International Energy Agency (IEA), *Key World Energy Statistics*, 2011

[2] L. Maugeri, Science 304 (2004) 1114

[3] The World Wind Energy Association (WWEA), *2011 Report*

[4] European Photovoltaic Industries Association (EPIA), *Solar Generation 6*, 2011

[5] A. de Vos, *Thermodynamics of Solar Energy Conversion*, Wiley-VCH (2008)

[6] EPIA, *Global Market Outlook until 2016*, 2012

[7] S. M. Sze and Kwok K. Ng, *Physics of Semiconductor Devices*, Wiley, 2007

[8] The American Standard for Testing and Measurements, ASTM G173-03

[9] J. D. Jackson, *Elettrodinamica Classica*, Zanichelli 2001 - Italian version of *J.D. Jackson, Classical Electrodynamics*

[10] O. S. Heavens, *Optical properties of thin films*, Reports on Progress in Physics 23 (1960) 1-65

[11] J. Gray, *The physics of the solar cell*, Chapter 3 of the *Handbook of photovoltaic science and engineering* edited by A. Luque and S. Hegedus, Wiley, 2003

[12] A. Luque and A. Martì, *Theoretical Limits of Photovoltaic Conversion*, Chapter 4 of *Handbook of photovoltaic science and engineering* edited by A. Luque and S. Hegedus, Wiley, 2003

[13] P. T. Landsberg et al. *Entropy fluxes, endoreversibility and solar energy conversion*, J. Appl. Phys. 74 (1993) 3631

[14] P. T. Landsberg, P. Baruch, *The thermodynamics of the conversion of radiation energy for photovoltaics*, J. Phys. A 22 (1989) 1911-1926

[15] M. A. Green, *Third generation photovoltaics*, Springer series in Photonics, 2006

[16] Shockley, Queisser, *Detailed balance limit of efficiency of p-n junction solar cells* J. Appl. Phys. 31 (1961) 510

[17] M. A. Green et al., *Solar cell efficiency tables* (version 40), Prog. Photovolt: Res. Appl. 20 (2012) 606-614

[18] A. Le Donne, A. Scaccabarozzi, S. Tombolato, S. Binetti, M. Acciarri, A. Abbotto, *Solar photovoltaics: a review*, Reviews in Advanced Science and Engineering 2 (2), June 2013 - IN PRESS

[19] G. Conibeer, *Third generation photovoltaics*, Materials Today 10 (2007) 42-50

[20] O. Semonin et al., *Peak external photocurrent quantum efficiency exceeding 100% via MEG in a quantum dot solar cell*, Science 334 (2011) 1530

[21] A. Luque, A. Martì, *Increasing the Efficiency of Ideal Solar Cells by Photon Induced Transitions at Intermediate Levels*, Phys. Rev. Lett. 78 (1997) 5014

[22] A. Martì, E. Antolin, C. R. Stanley, C. D. Farmer, N. Lopez, P. Diaz, E. Canovas, P. G. Linares, A. Luque, *Production of photocurrent due to intermediate to conduction band transitions: a demonstration of a key operating principle of the intermediate band solar cell*, Physical Review Letters 97 (2006) 247701

[23] A. Luque, A. Martì, *The intermediate band solar cell: progress toward the realization of an attractive concept*, Advanced Materials 22 (2010) 160-174

[24] A. Luque, A. Martì, C. Stanley, *Understanding intermediate band solar cells*, Nature Photonics 6 (2012) 146

[25] Y. Okada, T. Morioka, K. Yoshida, R. Oshima, Y. Shoji, T. Inoue, T. Kita, *Increase in photocurrent by optical transitions via intermediate quantum states in direct doped InAs/GaNAs strain compensated quantum dot solar cell*, Journal of Applied Physics 109 (2011) 024301

[26] K. A. Sablon, J. W. Little, V. Mitin, A. Sergeev, N. Vagidov, K. Reinhardt, *Strong enhancement of solar cell efficiency due to quantum dots with built-in charge*, Nano Letters 11 (2011) 2311-2317

[27] S. P. Bremner, S. N. Dahal, C. B. Honsberg, *Limiting efficiency of an intermediate band solar cell under concentrated AM1.5 spectrum*, Proc. 23rd EU-PVSEC (2008) 37-40

[28] L. Cuadra, A. Martì, A. Luque, *Influence of the overlap between the absorption coefficients on the efficiency of intermediate band solar cell*, IEEE Transactions on Electron Devices 51 (2004) 1002

[29] M. Y. Levy, C. B. Honsberg, *Solar cell with an intermediate band of finite width*, Physical Review B 78 (2008) 165122

[30] M. Y. Levy, C. B. Honsberg, *Intraband absorption in solar cells with an intermediate band*, Journal of Applied Physics 104 (2008) 113103

[31] A. Luque, A. Martì, L. Cuadra, *Thermodynamic consistency of sub-bandgap absorbing solar cell proposals*, IEEE Transactions on Electron Devices 48 (2001) 2118

[32] A. Luque, A. Martì, L. Cuadra, *Impact ionization assisted intermediate band solar cell*, IEEE Transactions on Electron Devices 50 (2003) 447

[33] A. Luque, A. Martì, *A metallic intermediate band high efficiency solar cell*, Progress in photovoltaics: Research and applications 9 (2001) 73-86

[34] A. Martì, L. Cuadra, N. Lopez, A. Luque, *Intermediate band solar cells: comparison with SRH recombination*, Semiconductors 38 (2004) 946

[35] K. M. Yu, W. Walukievicz, J. Wu, W. Shan, J. W. Beeman, M. A. Scarpulla, O. D. Dubon, P. Becla, *Diluted II-VI oxide semiconductors with multiple band gaps* Physical Review Letters 91 (2003) 246403

[36] K. M. Yu, W. Walukievicz, J. Wu Ager III, D. Bour, R. Farshchi, O. D. Dubon, S. X. Li, D. Sharp, E. E. Haller, *Multiband GaNAsP quaternary alloys*

[37] E. Antolin, A. Martì, J. Olea, D. Pastor, G. Gonzalez-Diaz, I. Martil, A. Luque, *Lifetime recovery in ultrahighly Ti-doped silicon for the implementation of and intermediate band material*, Applied Physics Letters 94 (2009) 042115

[38] A. Martì, D. Fuertes Marron, A. Luque, *Evaluation of the efficiency potential of intermediate band solar cells based on thin film chalcopyrite materials*, Journal of Applied Physics 103 (2008) 073706

[39] D. Fuertes Marron, A. Martì, A. Luque, *Thin-film intermediate band chalcopyrite solar cells*, Thin Solid Films 517 (2009) 2452

[40] Y. Okada, S. Yagi, R. Oshima, *High-efficiency solar cells based on quantum dot superlattice*, Oyo Buturi 79 (2010) 206

[41] A. Luque, P. G. Linares, E. Antolin, E. Canovas, C. D. Farmer, C. R. Stanley, A. Martì, *Multiple levels in intermediate band solar cells*, Applied Physics Letters 96 (2010) 013501

[42] A. Luque, P. G. Linares, E. Antolin, I. Ramiro, C. D. Farmer, E. Hernandez, I. Tobias, C. R. Stanley, A. Martì, *Understanding the operation of quantum dot intermediate band solar cells*, Journal of Applied Physics 111 (2012) 044502

[43] A. Luque, A. Martì, N. Lopez, E. Antolin, E. Canovas, C. Stanley, C. Farmer, P. Diaz, *Operation of the intermediate band solar cell under nonideal space charge region conditions and half filling of the intermediate band*, Journal of Applied Physics 99 (2006) 094503

[44] A. Martì, L. Cuadra, A. Luque, *Quasi-drift diffusion model for the quantum dot intermediate band solar cell*, IEEE Transactions on Electron Devices 49 (2002) 1632

[45] M. A. Green, *Multiple band and impurity photovoltaic solar cells: general theory and comparison to tandem cells*, Progress in Photovoltaics: Research and Applications 9 (2001) 137-144

[46] A. S. Brown, M. A. Green, *Intermediate band solar cell with many bands: ideal performance*, Journal of Applied Physics 94 (2003) 6150

[47] A. S. Brown, M. A. Green, R. P. Corkish, *Limiting efficiency for a multi-band solar cells containing three and four bands*, Physica E 14 (2002) 121

[48] C.Y. Shih, M.H. Tan, L.H. Hsu, C.P. Tsai, C.C. Lin, H.C. Kuo, K.Y. Chuang, T.S. Lay, *Numerical study of GaAs-based dual junction intermediate band solar cells*, 38th IEEE PVSC (2012) 1917

[49] E. Antolin, A. Martì, P. G. Linares, I. Ramiro, E. Hernandez, A. Luque, *Raising the efficiency limit of the GaAs-based intermediate band solar cell through the implementation of a monolithic tandem with an AlGaAs top cell*, 25th EU-PVSEC (2010) 65-68

[50] J. Lee, C. B. Honsberg, *The thermodynamic limits of tandem photovoltaic devices with intermediate band*, Proc. of SPIE vol. 8256 (2012) 82560Q-1

[51] A. Martì, N. Lopez, E. Antolin, E. Canovas, C. Stanley, C. Farmer, L. Cuadra, A. Luque, *Novel semiconductor solar cell structures: the quantum dot intermediate band solar cell*, Thin Solid Films 511-512 (2006) 638-644

[52] A. Luque, A. Martì, N. Lopez, E. Antolin, E. Canovas, C. Stanley, C. Farmer, L. J. Caballero, L. Cuadra, J. L. Balenzategui, *Experimental analysis of the quasi-Fermi level split in quantum dot intermediate band solar cells*, Applied Physics Letters 87 (2005) 083505

[53] K. Tanabe, D. Guimard, D. Bordel, R. Morihara, M. Nishioka, Y. Arakawa, *High efficiency InAs/GaAs quantum dot solar cells by MOCVD*, 38th IEEE PVSC (2012) 1929

[54] K. Tanabe, K. Watanabe, Y. Arakawa, *Thin film InAs/GaAs quantum dot solar cells layer transferred onto Si substrates and flexible plastic films*, 38th IEEE PVSC (2012) 105

[55] T. Sugaya, Y. Kamikawa, S. Furue, T. Amano, M. Mori, S. Niki, *Multi-stacked quantum dot solar cells fabricated by intermittent deposition of InGaAs*, Solar energy materials and Solar cells 95 (2011) 163

[56] S. J. Polly, C. G. Bailey, Z. S. Bittner, Y. Dai, E. G. Fernandez, S. M. Hubbard, *Spectroscopic analysis of InAs quantum dot solar cells*, Proc. of SPIE vol. 8256 (2012) 825615

[57] A. Martì, N. Lopez, E. Antolin, E. Canovas, A. Luque, C. R. Stanley, C. D. Farmer, P. Diaz, *Emitter degradation in quantum dot intermediate band solar cells*, Applied Physics Letters 90 (2007) 233510

[58] D. Zhou, G. Sharma, S. F. Thomassen, T. W. Reenaas, B. O. Fimland, *Optimization towards high density quantum dots for intermediate band solar cells grown by molecular beam epitaxy*, Applied Physics Letters 96 (2010) 061913

[59] J. Wu, Y. F. M. Makableh, R. Vasan, M. O. Manasreh, B. Liang, C. J. Reyner, D. L. Huffaker, *Strong interband transitions in InAs quantum dots solar cells*, Applied Physics Letters 100 (2012) 051907

[60] V. Popescu, G. Bester, M. C. Hanna, A. G. Norman, A. Zunger, *Theoretical and experimental examination of the intermediate band concept for strain balanced InGaAs/GaAsP quantum dot solar cells*, Physical Review B 78 (2001) 205321

[61] Y. Okada, N. Shiotsuka, H. Komiyama, K. Akahane, N. Ohtani, *Multistacking of highly uniform self-organized quantum dots for solar cell applications*, 20th EU-PVSEC (2005) 51

[62] Y. Okada, R. Oshima, *Current transport analysis in InAs/GaNAs strain compensated quantum dot superlattice solar cells*, 22nd EU-PVSEC (2007) 418

[63] R. Oshima, A. Takata, Y. Okada, *Strain compensated InAs/GaNAs quantum dots for use in high efficiency solar cells*, Applied Physics Letters 93 (2008) 083111

[64] R. B. Laghumavarapu, M. El-Emawy, N. Nuntawong, A. Moscho, F. L. Lester, D. L. Huffaker, *Improved device performance of InAs/GaAs quantum dot solar cells with GaP strain compensation layers*, Applied Physics Letters 91 (2007) 243115

[65] S. M. Hubbard, C. G. Bailey, C. D. Cress, S. Polly, J. Clark, D. V. Forbes, R. P. Raffaelle, S. G. Bailey, C. M. Wilt, *Short circuit current enhancement of GaAs solar cells using strain compensated InAs quantum dots*, 33rd IEEE PVSC (2008) 1-6

[66] S. M. Hubbard, C. D. Cress, C. G. Bailey, R. P. Raffaelle, S. G. Bailey, D. M. Wilt, *Effect of strain compensation on quantum dot enhanced GaAs solar cells*, Applied Physics Letters 92 (2008) 123512

[67] K. Akahane, N. Yamamoto, T. Kawanishi, *Fabrication of ultra high density InAs quantum dots using the strain compensation technique*, Physica Status Solidi A 208 (2011) 425

[68] E. Antolin, A. Martì, C. R. Stanley, C. D. Farmer, E. Canovas, N. Lopez, P. G. Linares, A. Luque, *Low temperature characterization of the photocurrent produced by two-photon transitions in a quantum dot intermediate band solar cell*, Thin Solid Films 516 (2008) 6919

[69] A. Mellor, A. Luque, I. Tobias, A. Martì, *The influence of quantum dot size on the sub-bandgap intraband photocurrent in intermediate band solar cells*, Applied Physics Letters 101 (2012) 133909

[70] J. S. Blakemore, *Semiconducting and other major properties of Gallium Arsenide*, J. Appl. Phys. 53 (1982) R123

[71] H. A. Atwater, A. Polman, *Plasmonics for improved photovoltaic devices*, Nature Materials 9 (2010) 205

[72] J. G. Fossum, *Physical operation of back-surface-field silicon solar cells*, IEEE Transactions on Electron devices 24 (1977) 322

[73] S. Michael, A. Bates, *The design and optimization of advanced multijunction solar cells using the Silvaco ATLAS software package*, Solar energy materials and Solar cells 87 (2005) 785

[74] M. Burgelman, P. Nollet, S. Degrave, *Modelling polycrystalline semiconductor solar cells*, Thin Solid Films 361-362 (2000) 527-532

[75] A. Froitzheim, R. Stangl, M. Kriegel, L. Elstner, W. Fuhs, *AFORS-HET, a Computer Program for the Simulation of Heterojunction Solar Cells to be Distributed for Public Use*, Proc. WCPEC-3, 3rd World Conference on Photovoltaic Energy Conversion, Osaka, Japan, May 2003, 1P-D3-34

[76] G. Letay, M. Hermle, A. W. Bett, *Simulating single junction GaAs solar cells including photon recycling*, Progress in photovoltaics: Research and applications 14 (2006) 683

[77] M. Burgelman, J. Verschraegen, S. Degrave, P. Nollet, *Modeling thin film PV devices*, Progress in photovoltaics: research and applications 12 (2004) 143

[78] D. L. Rode, S. Knight, *Electron transport in GaAs*, Physical Review B 3 (1971) 2534

[79] H. J. Lee, D. C. Look, *Hole transport in pure and doped GaAs*, Journal of Applied Physics 54 (1983) 4446

[80] S. Adachi, *GaAs, AlAs and AlGaAs: material parameters for use in research and device applications*, Journal of Applied Physics 58 (1985) R1

[81] G. Kaiblinger-Grujin, S. Selberherr, *A universal low-field electron mobility model for semiconductor device simulation*, http://www.nsti.org/procs/MSM98 Chapter 3, 70-75

[82] D. B. M. Klaassen, *A unified mobility model for device simulation. 1 Model equations and concentration dependence*, Solid state electronics 35 (1992) 953

[83] M. E. Law, E. Solley, M. Liang, D. E. Burk, *Self-consistent model of minority carrier lifetime, diffusion length and mobility*, IEEE Electron device letters 12 (1991) 401

[84] N. Shigyo, H. Tanimoto, M. Norishima, S. Yasuda, *Minority carrier mobility model for device simulation*, Solid state electronics 33 (1990) 727

[85] M. Sotoodeh, A. H. Khalid, A. A. Rezazadeh, *Empirical low-field mobility model for III-V compounds applicable in device simulation codes*, Journal of Applied Physics 87 (2000) 2890

[86] A. Chandra, C. E. C. Wood, D. W. Woodard, L. F. Eastman, *Surface and interface depletion corrections to free carrier density determinations by Hall measurements*, Solid-state electronics 22 (1979) 645

[87] N. Koguchi, S. Takahashi, T. Chikyow, *New MBE growth method for InSb quantum well boxes*, Journal of Crystal Growth 111 (1991) 688-692

[88] K. Watanabe, N. Koguchi, Y. Gotoh, *Fabrication of GaAs quantum dots by modified droplet epitaxy*, Japanese Journal of Applied Physics 39 (2000) 79-81

[89] M. Jo, T. Mano, Y. Sakuma, K. Sakoda, *Extremely high density GaAs quantum dots grown by droplet epitaxy*, Applied Physics Letters 100 (2012) 212113

[90] C. Somaschini, S. Bietti, N. Koguchi, S. Sanguinetti, *Fabrication of multiple concentric nanoring structures*, Nano Letters 9 (2009) 3419

[91] C. Somaschini, S. Bietti, A. Scaccabarozzi, E. Grilli, S. Sanguinetti, *Self-assembly of quantum dot-disk nanostructures via growth kinetics control*, Crystal Growth and Design 12 (2012) 1180

[92] S. Sanguinetti, K. Watanabe, T. Tateno, M. Wakaki, N. Koguchi, T. Kuroda, F. Minami, and M. Gurioli, Applied Physics Letters 81 (2002) 613

[93] L. J. Brillson, *Contacts to semiconductors - Fundamentals and technology*, Noyes Publications (1993)

[94] J.W. Orton, P. Blood, *The electrical characterization of semiconductors: measurement of Majority carrier properties*, Academic Press (1990)

[95] P. D. DeMoulin, S. Tobin, M. Lundstrom, M. S. Carpenter, M. R. Melloch, *Influence of perimeter recombination on high efficiency GaAs p/n heteroface solar cells*, IEEE Elec. Dev. Lett. 9 (1988) 368

[96] A. R. Clawson, *Guide to references on III-V semiconductor chemical etching*, Mat. Sci. and Eng. 31 (2001) 1-438

[97] K. A. Emery, C. R. Osterwald, *Solar cell calibration methods*, Solar Cells 27 (1989) 445

[98] R. J. Matson, K. A. Emery, R. E. Bird, *Terrestrial solar spectra, solar simulation and solar cell short-circuit current calibration: a review*, Solar Cells 11 (1984) 105

[99] K. A. Emery, C. R. Osterwald, *Solar cell efficiency measurements*, Solar Cells 17 (1986) 253

[100] S. P. Tobin, S. M. Vernon, C. Bajgar, L. M. Geoffroy, C. J. Keavney, M. M. Sanfacon, V. E. Haven, *Device processing and analysis of high efficiency GaAs solar cells*, Solar Cells 24 (1988) 103-115

[101] S. P. Tobin, S. M. Vernon, C. Bajgar, S. J. Wojtczuk, M. R. Melloch, A. Keshavarzi, T. B. Stellwag, S. Venkatensan, M. S. Lundstrom, K. Emery, *Assessment of MOCVD and MBE grown GaAs for high efficiency solar cell applications*, IEEE Trans. Electron Dev. 37 (1990) 469

[102] P. D. DeMoulin, S. P. Tobin, M. S. Lundstrom, M. S. Carpenter, M. R. Melloch, *Influence of perimeter recombination on high efficiency GaAs p/n heteroface solar cells*, IEEE Electron Dev. Lett. 9 (1988) 368

[103] B. M. Kayes, H. Nie, R. Twist, S. G. Spruytte, F. Reinhardt, I. C. Kizilyalli, G. S. Higashi, *27.6% conversion efficiency, a new record for single junction solar cells under 1 sun illumination*, Proceedings of the 37th IEEE PVSC (2011) 4-8

[104] M. R. Melloch, S. P. Tobin, C. Bajgar, A. Keshavarzi, T. B. Stellwag, G. B. Lush, M. S. Lundstrom, K. Emery, *High efficiency $Al_{0.22}Ga_{0.78}As$ solar cells grown by molecular beam epitaxy*, Applied Physics Letters 57 (1990) 52

[105] K. Takahashi, Y. Minagawa, S. Yamada, T. Unno, *Improved efficiency of $Al_{0.36}Ga_{0.64}As$ solar cells with a pp^-n^-n structure*, Solar energy materials and solar cells 66 (2001) 525-532

[106] C. Amano, H. Sugiura, K. Ando, M. Yamaguchi, *High efficiency $Al_{0.3}Ga_{0.7}As$ solar cells grown by molecular beam epitaxy*, Applied Physics Letters 51 (1987) 1075

[107] SPIRE Corp. Contractor Report *Development of a thin AlGaAs solar cell* SAND87-7098(1987)

[108] M. R. Melloch, S. P. Tobin, C. Bajgar, T. B. Stellwag, A. Keshavarzi, M. S. Lundstrom, K. Emery, *High efficiency GaAs and AlGaAs solar cells grown by molecular beam epitaxy*, Proc. 21st IEEE PVSC (1990) 163-167

[109] E. Munoz, E. Calleja, I. Izpura, F. Garcia, A. L. Romero, J. L. Sanchez-Rojas, A. L. Powell, J. Castagné, *Techniques to minimize DX center deleterious effects in III-V device performance*, Journal of Applied Physics 73 (1993) 4988

[110] E. Antolin, A. Martì, C. D. Farmer, P. G. Linares, E. Hernandez, A. M. Sanchez, T. Ben, S. I. Molina, C. R. Stanley, A. Luque, *Reducing carrier escape in the InAs/GaAs quantum dot intermediate band solar cell*, Journal of applied physics 108 (2010) 064513

[111] I. Ramiro, E. Antolín, P. G. Linares, E. Hernández, A. Martí, A. Luque, C. D. Farmer, C. R. Stanley, *Application of photoluminescence and electroluminescence techniques to the characterization of intermediate band solar cells*, Energy Procedia 10 (2011) 117-121

[112] P. Wuerfel, *The chemical potential of radiation*, Journal of Physics C: Solid state physics 15 (1982) 3967

LIST OF PUBLICATIONS

G. Gori, R. Campesato, M. C. Casale, G. Gabetta, M. Zenobi, A. Principe, S. Rossi, A. Scaccabarozzi, S. Binetti, M. Acciarri, *Multi junction cells for standard and spectrum splitting concentrated photovoltaics- Indoor and outdoor performances.* Proc. 26th EUPVSEC (2011) 676-680

C. Somaschini, S. Bietti, A. Scaccabarozzi, E. Grilli, S. Sanguinetti, *Self-assembly of quantum dot-disk nanostructures via growth kinetics control.* Crystal Growth and Design 12 (2012) 1180-1184

A. Scaccabarozzi, M. Acciarri, S. Bietti, S. Sanguinetti, *Quantum dot intermediate band solar cells made of AlGaAs alloy systems.* 27th EUPVSEC (2012)

A. Le Donne, A. Scaccabarozzi, S. Tombolato, S. Binetti, M. Acciarri, A. Abbotto, *Solar photovoltaics: a review*, ACCEPTED by Reviews in Advanced Science and Engineering 2 (2), June 2013 - IN PRESS

A. Scaccabarozzi, S. Adorno, S. Bietti, M. Acciarri, S. Sanguinetti, *GaAs/AlGaAs quantum dot intermediate-band solar cell grown by*

droplet epitaxy. TO BE PRESENTED at EuroMBE 2013

L. Miglio, S. Bietti, A. Scaccabarozzi, R. Bergamaschini, C. Frigeri, G. Isella, F. Isa, C. V. Falub, E. Bonera, M. Bollani, P. Niedermann, H. von Kaenel, S. Sanguinetti, *Monolithic integration of GaAs on deeply patterned Si substrates by self-assembled arrays of 3-dimensional crystals.* TO BE PRESENTED at EuroMBE 2013

A. Scaccabarozzi, S. Adorno, S. Bietti, M. Acciarri, S. Sanguinetti, *Evidence of two-photon absorption in strain-free quantum dot GaAs / AlGaAs solar cells.* ACCEPTED for publication in Physica Status Solidi - Rapid Research Letters

S. Bietti, A. Scaccabarozzi, R. Bergamaschini, C. Frigeri, C. V. Falub, M. Bollani, E. Bonera, P. Niedermann, H. von Kaenel, S. Sanguinetti, L. Miglio, *Monolithic integration of GaAs on deeply patterned Si substrates by self-assembled arrays of three-dimensional crystals.* SUBMITTED to Nature Materials

A. Scaccabarozzi, S. Adorno, S. Bietti, M. Acciarri, S. Sanguinetti, *Characterization of GaAs/AlGaAs quantum dot intermediate band solar cells made by droplet epitaxy.* IN PREPARATION

A. Scaccabarozzi, S. Bietti, A. Marzegalli, S. C. Cecchi, H. von Kaenel, S. Sanguinetti, L. Miglio, *Analysis of the thermal strain relaxation of GaAs three-dimensional crystals grown on deeply patterned Si substrates.* IN PREPARATION

ACKNOWLEDGEMENTS

This work would never have been possible without the great help and support of many people. To all of them go my great thanks, and sorry if in the rush of the final days I can't remember all of them.
First of all I want to thank my supervisors, Dr. Maurizio Acciarri and Prof. Stefano Sanguinetti. Thanks for welcoming me and letting me work in a pleasant and somehow family-like environment. As in all families, sometimes there are arguments and misunderstandings: sorry about that. Thanks for sharing your knowledge and your point of view about many different things. Thanks for sharing the enthusiasm (and the effort) of doing this work.
I wish to thank Dr. Sergio Bietti for useful discussions about MBE, nanostructures and much more. And of course also for being good friend and my personal sample grower. Thanks to Jacopo Frigerio, nice friend and good cleanroom teacher, for all the discussions, complaints and suggestions in these years. Great thanks to my friend Dr. Stefano Marchionna, with whom I enjoyed a lot of time spent in the lab assembling or repairing stuff. Working with you is such a fun, despite you make a terrible mess!
Though not directly involved in my Ph.D. project (and especially for that) I must thank Dr. Enos Gombia, for his extremely useful guidelines at the beginning of my work. I really appreciated that

help and kindness. And I must thanks also Prof. Emanuele Grilli for being so patient and kind with all the stuff related to optics: I always learned something while talking to him, and I still learn.
Thanks to all the people in the Bicocca groups, Simona, Alessia, Sara, Paolo, Andrea, Bruno, Eleonora, Fabio, Anna, and former members like Manuel, Elisabetta, Lorenzo and Matteo. Discussions, lunches, meetings, lab work and whatever we could share in these years have been very nice moments, thank you!
Thanks to all the people in the Como lab, Fabio, Silvia, Andrea, Alexey, Erica, Marco and Stefano. You made my trips to Como very pleasant every time.
Thanks to the undergraduate students I had in these years, Paolo, Luka, Simone and Matteo. Working with you also allowed me to grow a lot and increase my experience. And thanks for the Porto wine too!
Thanks to all the people I met during my stay at NICT, Tokyo. I wish to thank Dr. Kouichi Akahane for welcoming me in spite of being extremely busy, and for the very long discussions we had, from which I took extremely useful tips for my work. Thanks to André, Lu and Pham and all the other guys I met there: I had a very great time with you!
Thanks to all the people who supported me during these years out of the work: Angelo, Alessandra, Claudia, Laura, Filippo, Germano, Daniela, Caio, Francesca, the Cafarellis, Preso, Barbaz, David, Fabio and all the guys of Delirium, Simone, Giovanni, Paolo, Andrea, Raffaele, Riccardo, Francesco, Antonio and all the guys of the Accademia Corale. Without you I wouldn't be the person I am today. Thanks for your patience, love and suggestions. You probably don't know how important your support has been and still is today for me. Please don't give up!
Thanks to my family and my parents for their infinite patience. I promise you that one day you will eventually understand what my job is. Apart from this, thanks for being proud of your son.

Andrea